Non-Smooth Controller Optimization for Active Vibration Isolation Suspension of an Einstein Telescope Mirror

Author

S.K. Sijtsma

Master Mechanical Engineering

Faculty of Engineering Technology

Department of Mechanics, Solids, Surfaces and Systems
Precision Engineering

Examination Committee

Dr.Ir W.B.J. Hakvoort[1]
Dr.Ir. J.P. Schilder[1]
Ir. S.T. Spanjer[1]
Dr. C.M. Mow-Lowry[2]

[1] Faculty of Engineering Technology, University of Twente
[2] Department of Physics and Astronomy, Vrije Universiteit Amsterdam

October, 2024

Preface

This thesis concludes my Master's degree Mechanical Engineering in Robotics. The research on which this report is based has learned me about applying gained knowledge from the past years of studying at the University of Twente. Moreover, this research allowed me to dive deeper in interesting control system design topics. Besides this thesis, both mentors from Nikhef and the University of Twente enabled me to write a publication for a scientific journal, which all in all was an interesting and enjoyable experience.

I would like to thank a number of people. First of all, I would like to express my gratitude to Wouter Hakvoort and Sil Spanjer from the University of Twente. Both have significantly supported my research and answered many control related issues throughout the full length of my time here in Amsterdam. I would also like to thank Wouter for reaching out to Nikhef to arrange this graduation assignment. Furthermore, I would like to thank Conor Mow-Lowry, Pooya Saffarieh and Nathan Holland for their daily support at Nikhef. All these people have greatly contributed to my understanding of gravitational wave science, but moreover made my time at Nikhef really enjoyable throughout the proceedings of this concluding part of my study.

Sander Kieran Sijtsma, 9th of October 2024, Amsterdam

Abstract

Gravitational waves are ripples in space-time that carry valuable information about interactions between large interstellar objects, such as neutron stars, black holes or supernovae. The information that gravitational waves carry can reveal new insights about physics and our understanding of the universe. These signals are measured by gravitational wave observatories. These observatories employ laser interferometry to detect gravitational waves, which relies on measuring a phase difference between two perpendicularly reflected laser beams that originate from a single laser source. This phase difference is induced by a disruption of space-time between the lasers, that can be the cause of a gravitational wave passing through the earth. These observatories are extremely sensitive to seismic activities from the earth's surface. Therefore, an elaborate vibration isolation suspension guards the mirrors, that alter the path of the lasers, from the seismic noise. Without these suspensions, a gravitational wave measurement would vanish in noise. Usually, the control systems for gravitational wave applications are designed via classical frequency domain design methods, such as loop-shaping. This design approach can be time consuming, labour intensive and often requires much expertise and knowledge about the suspension design in order to successfully design suitable controllers. A more modern approach for the design of controllers is via optimal controller synthesis methods. The great benefit of these optimal controller design techniques is that they largely automate the controller design. This allows to quickly evaluate the achievable performance for many suspension configurations within the available design space. This makes optimal controller synthesis especially usefull for future gravitational wave observatories that are still in the design phase. This research investigates the usefulness of a non-smooth optimal controller design strategy, specifically for the controller design for the mirror suspensions that are present in gravitational wave observatories. Additionally, optimization of the actuation distribution and suspension mechanics is integrated with the controller design for a more holistic design approach. Moreover, the suitability of the optimal controller design method is investigated in terms of its ability to encapsulate typical requirements that are found for gravitational wave applications into a suitable optimization problem. Part of the research is therefore dedicated to shaping the requirements into a relevant optimization problem. Besides the optimization of the controller and actuation distribution, some relevant extensions are investigated to showcase the versatility and flexibility of the non-smooth optimization algorithm. These extensions involve simultaneous optimization of both the controller and the dynamics of the plant. The results show how the proposed methodology is able to successfully shape controllers and the distribution of the actuation over the stages of the suspension according to requirements. The controllers generally achieve good suppression of seismic disturbances, while conforming to frequency dependent bounds and stability margins.

Contents

Chapter 1

Introduction

Gravitational Waves (GW) are distortions in space-time that carry valuable information about interactions between large interstellar objects. They are induced by for example interactions between black holes, binary neutron stars or supernovae that occur far away from earth. The information that such a gravitational wave carries is valuable for scientists, because it may reveal new insights about our understanding of physics and the universe [35, 37]. Although predicted by Einstein in 1916, the first detections of gravitational waves were made almost a century later by the LIGO-Virgo-KAGRA collaboration [2–7]

The detection of these signals is not trivial. Decades of research regarding the development of gravitational wave detectors will lead to a new generation, highly advanced gravitational wave observatory; the Einstein Telescope (ET) [41]. Its predecessors, such as the LIGO [1] and Virgo [8] observatories and ET itself all rely on a similar working principle to measure the presence of a gravitational wave that passes by the earth. All these telescopes make use of laser interferometry, of which the operating principle is based on measuring phase differences between perpendicular lasers, that are induced by gravitational waves.

An interferometer thus makes use of lasers to detect a gravitational wave. A laser splits into two beams, which are sent through two perpendicular arms. These arms typically have a length in the order of a few kilometres. The laser beams are both reflected by a mirror, or test mass, at the end of each arm. The reflected beams interfere at the base of the arms. A gravitational wave that passes by the earth manifests as a distortion in space-time and this effectively stretches the earth in one direction and compresses the earth in a direction perpendicularly. Since a gravitational wave disturbs the space-time between the lasers, it can lead to non-destructive interference between the reflected beams, because one laser beam travels further that the other. Such an interference pattern can be an indication of a gravitational wave passing through the earth.

The Einstein Telescope is made up of two separate interferometers, where one interferometer is responsible for measuring gravitational waves with a low frequency content from $3 - 30$Hz (ET-LF) and the other is responsible for measuring gravitational waves with a high frequency content between $30 - 10^4$Hz (ET-HF) [28]. The largest deformations that must be detected are in the order of 10^{-18}m and one can imagine that various noise sources can impact the measurements significantly. Therefore, the mirrors must be isolated from vibrations of the earth's surface. Each mirror is isolated from seismic activity by means of a vibration isolation system that minimizes the effect of seismic disturbances on the measurement of the interferometer. If not attenuated, a gravitational wave signal will simply vanish in the noise from the earth.

The test masses for all observatories are suspended by a combination of active and passive vibration isolation filters, to guard the mirrors from any vibrations that are induced by numerous sources. Examples of sources of vibrations are earthquakes, traffic or natural seismic activities induced by weather conditions [10]. For ET, a part of the seismic noise is compensated for by a seismic isolation table, which is a 6DoF actively controlled isolation table. This platform is followed by a large inverted pendulum. A multi-pendulum suspension is suspended from this inverted pendulum. The first couple of pendulums act as a passive filter, after which another actively controlled multi-pendulum suspension compensates for any residual seismic activity that is left after the other isolation stages. This last part of the suspension is referred to as the payload suspension. This sub-system is the part of the suspension chain that is considered for this study. A schematic overview of a similar suspension chain of Advanced Virgo is shown

in Figure 1.1. The Virgo superattenuator does not include an ISI.

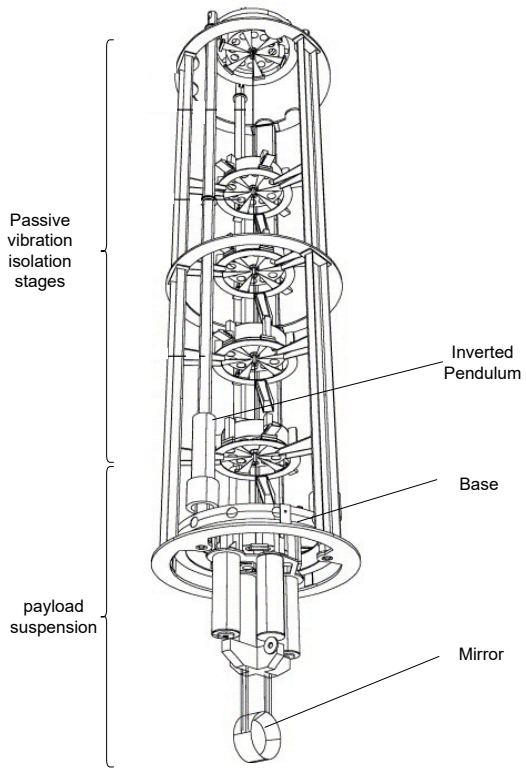

Figure 1.1: Schematic overview of the Advanced Virgo suspension chain [14], consisting of an inverted pendulum and multi-pendulum filter

For many years, the control systems that make up the gravitational wave detectors are designed via classical frequency domain controller design methods [9, 30]. These methods require much expertise about the suspension, are generally labour intensive and moreover can be rather time consuming. From the 1980s, more modern approaches were introduced to design controllers for a broad spectrum of applications. Not by hand, but via algorithms implemented in software. Among the controller optimization strategies, $\mathcal{H}_2$- and $\mathcal{H}_\infty$-optimal control are arguably the most popular methods for optimization based controller design [38]. Optimal design methodologies automate the controller design process significantly and therefore ease the design of control systems, while reducing design time for the control algorithms. The responsibility of the designer is shifted to defining a suitable definition of the optimization problem. Once the optimization problem is formulated, the performance of different configurations of the suspension design can be assessed quickly without much expertise required by the designer.

These optimal methods have already been applied to GW applications [19, 42]. Often, either $\mathcal{H}_2$- or $\mathcal{H}_\infty$-optimal control is employed for applications within the GW research field. However, it can be shown that typical requirements for the payload suspensions that are present in a gravitational wave observatory require both optimal control design paradigms to synthesize controllers that satisfy all requirements. Combining both $\mathcal{H}_2$- and $\mathcal{H}_\infty$-control into a single optimization is a novel approach to design controllers for gravitational wave applications. For the control system design for a typical payload suspension, these methods allow for quick exploration of the design space for the suspension mechanics and control to an extent that is simply not feasible to achieve with classical controller design techniques. For this reason, such optimal control techniques lend themselves well to investigate the performance of many suspension topologies early in the design phase. This makes such methods specifically interesting for third generation or other future gravitational wave observatories such as ET and Cosmic Explorer (CE) [18]. The next section discusses the research questions that this study aims to answer.

1.1 Scope and Research Questions

This study is part of a collaboration between the University of Twente and the VU and has two research goals as the outcome. The main goal is to investigate whether recently studied control system optimization methods are suitable for applications within gravitational wave disciplines. More specifically, this is investigated on the occasion of the development of the Einstein Telescope. One of the main interests for this study is to investigate whether advanced optimization methods are suitable to aid control system design, specifically for mirror suspensions that are part of the gravitational wave telescopes. This also leads to the other goal of this research.

A considerable part of this work is dedicated to the identification of the control challenge that is associated with such gravitational wave telescopes. The use of modern multi-objective control design tools have not yet been incorporated in the design of current gravitational wave detectors. Applications of such methods is relatively novel, specifically to the payload suspensions that isolate the mirrors from seismic disturbances. Therefore, part of the research is dedicated to establish an understanding of the problem that is interpretable for control system design. This is eventually condensed in a fitting control problem that best meets the identified requirements and description of the suspension. The next chapters elaborate more on the details of the operating principles of gravitational wave observatories and the formulation of the challenge in terms of a relevant control problem. To support the research, a set of research questions were identified to guide the study and support the outcome of this work.

> ***RQ. 1:*** *How can typical requirements for the Einstein Telescope seismic isolation suspensions be translated in a suitable control problem formulation, fitting an optimal control framework?*

Some relevant detailing of this question is supported by the accompanying sub-questions. One main interface between the system description and the solution process is formulated in terms of suitable requirements that best meet the purpose of the active suspension.

> ***RQ. 1.1:*** *What are the requirements for the control system?*

To put the need of the active controlled suspension in perspective, the following questions are relevant:

> ***RQ. 1.2:*** *How exactly does the mirror suspension integrate with the rest of the gravitational wave telescope?*

> ***RQ. 1.3:*** *What is the purpose of the mirror suspension from an engineering perspective?*

The other goal is to investigate the suitability of optimal control strategies as a method that aids the controller design process. The research questions that reflects the investigation of a suitable controller optimization strategy is formulated as:

> ***RQ. 2:*** *Can optimal controller synthesis methodologies aid controller design for active mirror suspensions for gravitational wave telescopes?*

A supporting question that also reflects the needs of the first set of research questions would be:

> ***RQ. 2.1:*** *Which type of optimization best fits the needs of the mirror suspension controller design?*

Since the type of optimization strategy is closely related to the requirements for the control system.

1.2 Research and Outline

This research proposes a non-smooth controller optimization method, combined with Dynamic Error Budgeting techniques [26, 33], to design control systems for the active payload suspension of a gravitational wave telescope. Similar techniques were already shown to be successful within the precision engineering field [39]. Although some detailing is given for ET specifically, the proposed methodology could also apply to the development of mirror suspensions for other future telescopes. A simplified suspension model is considered for this research, to find out whether controller optimization design tools are usefull

for these type of systems. The suitability is expressed in terms of achievable performance, inclusion of non-conventional open-loop requirements and improvement of the design process compared to a design process that relies on classical controller design techniques. The proposed optimization methodology also allows to tune dynamic systems, other than the feedback controllers. Therefore, a joint controller and mechatronic system design is investigated to explore the full capabilities of non-smooth mixed controller synthesis.

The structure of this report is organised as follows; Chapter 2 provides a more detailed description of the interferometer. This chapter also addresses the requirements for the payload suspension control system. Chapter 3 derives models for the suspension as well as relevant filters that are used in the optimization studies that were carried out during this research. The design of these models flow from the requirements that were derived in Chapter 2. The third chapter also addresses the architecture of the control loop. Chapter 4 shows the results of several optimization studies that were carried out to answer the research questions that were posed in the previous paragraph. Then, the results are interpreted in Chapter 5 to assess whether the proposed optimization method conforms to the needs for the control system design for gravitational wave payload suspensions. This chapter also discusses some relevant topics for further research. Finally, Chapter 6 summarizes the main findings of this research.

Chapter 2

Problem Definition

As mentioned in the previous section, all ground based telescopes employ laser interferometry to measure gravitational waves. A view of LIGO and a schematic representation of a basic Michelson interferometer are shown in Figure 2.1. The operating principle of such an interferometer works as follows. A laser is split into two beams by a beam splitter. The individual beams travel through two, perpendicularly placed arms. These arms typically have a length in the order of a few kilometers. Each laser is reflected at the end of each arm by a mirror and both beams interfere at the base. This interference is measured by a photo detector at the base of the arms of the interferometer. If there is no presence of a gravitational wave, each beam will travel exactly the same amount of distance. The lasers will then interfere destructively, or in other words, they cancel each other out. This changes due to the presence of a gravitational wave that passes through the earth. A gravitational wave strains the space-time between the mirrors. This causes a laser beam in one arm to travel more than the other, due to a relative differential motion between the mirrors that is induced by a gravitational wave [36]. On its turn, this causes non-destructive interference between the lasers which is measured by the photo detector. The measured interference pattern is then a measure for a gravitational wave.

(a) View of LIGO Livingston [16]

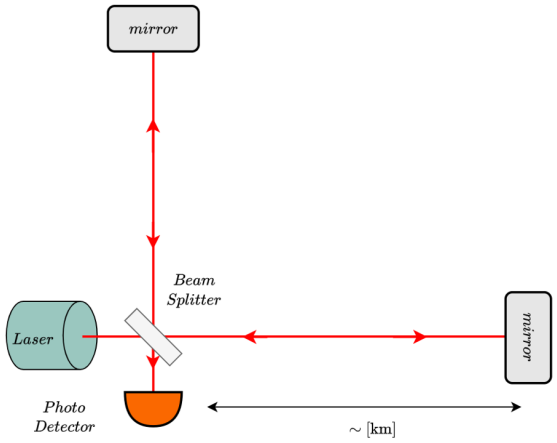

(b) schematic overview of a basic Michelson interferometer

Figure 2.1: View of LIGO Livingston and a schematic representation of a basic Michelson interferometer

Each arm of the interferometer is equipped with a Fabry-Pérot (FP) cavity, that acts as an optical resonator [17]. Figure 2.2 includes such FP cavities. Each cavity is an enclosed resonating space that is created between two mirrors. These resonators effectively extend the optical traveling path of each laser, and thus increase the sensitivity of the observatory. The length of this cavity should fit an integer number of wavelengths to ensure that the FP cavities are able to resonate the laser beams. This is called the resonating condition of the optical resonators.

The interferometer is an extremely sensitive device. Seismic activity from the earth's surface would leave gravitational waves immeasurable, if the mirrors were not isolated from ground motion. Each mirror in the interferometer is therefore isolated from seismic disturbances by means of an elaborate suspension.

The suspension involves both active and passive seismic isolation strategies. This means that the active suspension should compensate for residual seismic disturbances felt at the mirror to suppress the longitudinal differential motion of the optical resonators that are present in each interferometer arm.

The main aim of the control system for these active suspensions is to attenuate effective seismic motion from the earth's surface that is felt at the mirror stage. Not directly on the measurement, but to keep the telescope within its small linear operating range. This is elaborated on in Section 2.2. The control system inevitably requires actuation of some kind to the suspension stages. Since the controllers will be implemented digitally, the injection of Digital to Analog Converter (DAC) voltage noise from the actuators to the control loop is something that cannot be avoided. The next sections elaborate on this and illustrate some useful performance indicators that will be used for the formulation of a suitable controller optimization statement.

The attenuation of seismic noise and on the other hand the injection of electrical DAC noise into the system form the basic requirements for the control system. Often, in control system design, such requirements manifest mostly as limits on closed-loop transfer functions, which dictate the ability of a control system to follow references or reject disturbances to name a few. In science involving gravitational wave detection however, requirements are often formulated in some open-loop equivalence of (a combination of) noise sources, instead of their closed-loop counterpart. The next section will elaborate on this open-loop representation of a noise source. Especially for the DAC noise, since this is the main open-loop contribution that is considered for this study.

2.1 Open-Loop Equivalence for Gravitational Wave Detectors

The measurement of a gravitational wave is not trivial in the sense that one cannot design a sensor that directly measures the gravitational wave and converts it into a proportional electrical signal. Instead, the gravitational wave couples in the loop very similar to the seismic noise, since it effectively acts upon the longitudinal degree of freedom of the the FP cavities. A schematic overview of an interferometer, including a part of the mirror suspension is illustrated in Figure 2.2[1].

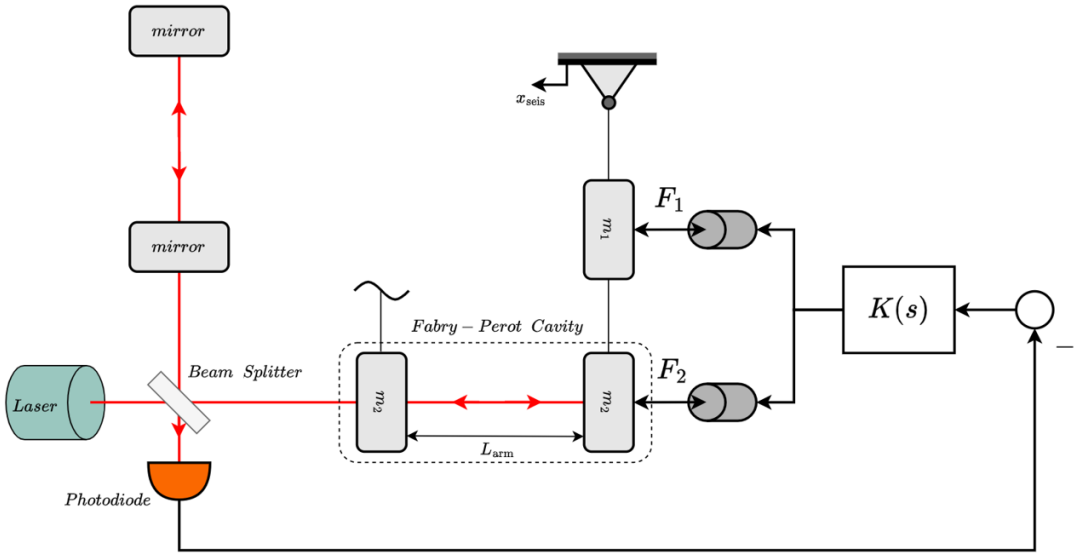

Figure 2.2: Schematic of a Michelson interferometer, including a part of the mirror suspension and control loop

The standard feedback configuration of Figure 2.3 shows where the DAC noise u_{dac}, seismic noise x_{seis} and a gravitational wave signal f_{GW} enter the control loop. Seismic motion, although attenuated, will

[1]The Einstein Telescope will likely employ an interferometer with three arms, arranged in a triangular configuration. However, the Michelson interferometer, which is used in the LIGO and Virgo observatory, works in a very similar fashion and hence the concepts mentioned in this text can be interpreted analogously to the interferometer for ET

result in motion of the FP cavities and thus changes the length of the optical path of the laser. A gravitational wave strains the spacetime between the two respective lasers by a small amount, and this also changes the spacetime between the mirrors in a similar way. Notice that seismic noise and gravitational waves have a similar effect on the interference measurement at the base of the telescope and hence enter the control loop at the same location, at the output of the plant[2].

From the above we can make up that the measurement of a gravitational wave is not a direct measurement in the sense that the gravitational have is 'hidden' in the output of the telescope. To obtain the gravitational wave signal, one must reconstruct it from the closed-loop system signals. This reconstruction heavily relies on knowledge of the systems that make up the interferometer as well as accurate models of the dynamics of the suspension. As an illustrative example, consider the output $\hat{y}$ of the telescope, as measured at the base of the arms of the interferometer. Let $P(s)$ denote the suspension dynamics and $K(s)$ a feedback controller that regulates the suspension. Then, we can write this output as a linear combination of the exogenous inputs as follows.

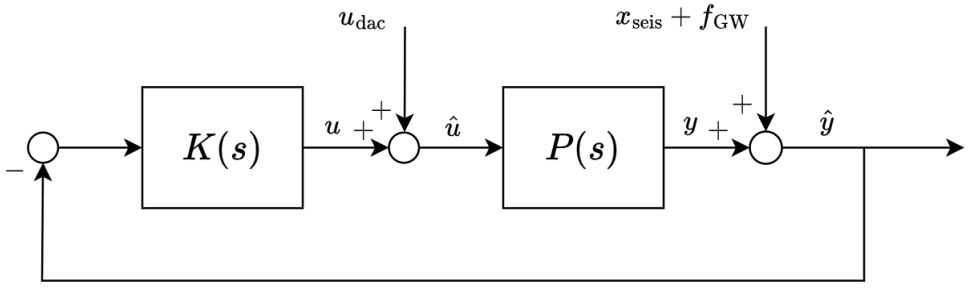

Figure 2.3: Standard feedback loop illustrating how a gravitational wave enters the control loop

$$\hat{y}(s) = (I + P(s)K(s))^{-1}P(s) \cdot u_{\text{dac}}(s) + (I + P(s)K(s))^{-1} \cdot x_{\text{seis}}(s) + (I + P(s)K(s))^{-1} \cdot f_{\text{GW}}(s) \quad (2.1)$$

Reconstructing the gravitational wave from the signal $\hat{y}$ yields the following equation.

$$(I + P(s)K(s))\hat{y}(s) = P(s) \cdot u_{dac}(s) + x_{\text{seis}}(s) + f_{\text{GW}}(s) \quad (2.2)$$

$$f_{\text{GW}}(s) = (I + P(s)K(s))\hat{y}(s) - P(s) \cdot u_{\text{dac}}(s) - x_{\text{seis}}(s) \quad (2.3)$$

The contribution of the noise sources is not dependent on the controller anymore, and can be interpreted as the *open-loop equivalence*. It should be noted that the individual noise sources and gravitational wave signal should be compared in phase. This is because they all have a direct effect on the measured optical phase between the laser beams. The open-loop equivalence of the DAC noise is thus given by the following equation.

$$u_{\text{dac,ol}} = P(s) \cdot u_{\text{dac}}(s) \quad (2.4)$$

From Equation 2.3 it can also be concluded that it is sufficient to know the effective seismic disturbance at the output of the plant. In order to understand the limits on the allowable DAC noise, it is of importance to understand the sensitivity curve of a gravitational wave detector.

Gravitational Wave Observatory Sensitivity Curves

The sensitive frequency range in which a GW observatory operates is given by it's design sensitivity curve. Such a curve is expressed as an open-loop equivalent Amplitude Spectral Density (ASD). The curve is limited by the various noise sources that inevitably limit the sensitivity of the observatory over the frequency spectrum [15]. Figure 2.4 shows the design sensitivity curves for advanced LIGO, ET and CE.

[2]This follows from a modelling choice. The suspension model is part of the seismic noise model, hence it enters the loop at the output of the suspension transfer function. The seismic disturbance is measured at the top stage of the pendulum chain, and not at stages further down the chain

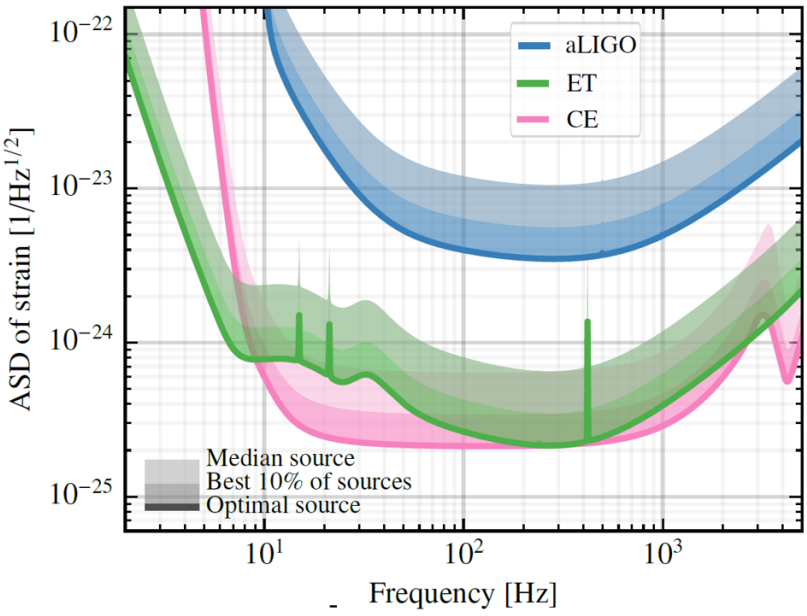

Figure 2.4: Design sensitivity curves of Advanced LIGO, ET and CE [41]

Cosmic sources that emit gravitational waves with a magnitude above the sensitivity curve, and a frequency content that lies within the sensitive frequency range, can be detected. The effect of noise sources may therefore not exceed the sensitivity design curve of the observatory, since exceeding the curve leads to deterioration of the overall sensitivity of the telescope. For this reason, the open-loop equivalence of the DAC noise may not exceed the sensitivity curve of ET. This curve thus forms a frequency dependent bound on the DAC noise.

2.2 Closed-Loop Seismic Noise Suppression

One would suspect that, similarly, the open-loop projection of the seismic noise to the mirror output should be considered as a disturbance, instead of the closed-loop seismic noise. This however, is not the case for this problem. The reason for the suppression of the closed-loop seismic noise is to maintain the output of the telescope within its linear operating range such that the FP cavities remain in their resonating condition [43]. Moreover, the open-loop projection of the seismic noise cannot be rejected by the controlled system, since it is independent of the controller, as can be seen in Equation 2.3. To maintain the linear operating range of the telescope, the Root-Mean-Square (RMS) of the residual seismic disturbance that is felt at the mirror should be minimized.

To illustrate the linear operating range of the telescope, consider the following. An interferometric measuring setup measures the power of the sum of the electrical fields, induced by the two interfering laser beams at the base of the arms. If there exists a phase difference between incoming laser beams, the lasers will interfere non-destructively. Therefore, the telescope will measure a power that is equivalent to the relative elongation of the telescope arms of the interferometer that is the result of a gravitational wave. Figure 2.5 shows a plot of how the power output of the photo detector is related to the relative displacement Δx between the mirrors that induces a phase difference between the two reflected laser beams (phase difference $\varphi = 2 \cdot (\frac{2\pi}{\lambda} \Delta x)$, where λ denotes the wavelength of the laser). This relative displacement can for example be induced by a gravitational wave.

From this curve it can be seen that, around a Δx where the slope of the power is the steepest, the telescope is the most sensitive. At this point, a small Δx has the highest effect on the change of the measured power. The drawback of measuring around a high-power operating point is that several noise sources, amongst which quantum noise, are amplified. This results in a low Signal to Noise Ratio (SNR) for the measurement. Vice versa, the SNR is the highest around the lowest power point in the graph (close to $\Delta x = 0$, but not at $\Delta x = 0$). Measuring close to this zero power point is not trivial, since the power output of the telescope is also close to zero. Therefore, the operating point of the telescope is

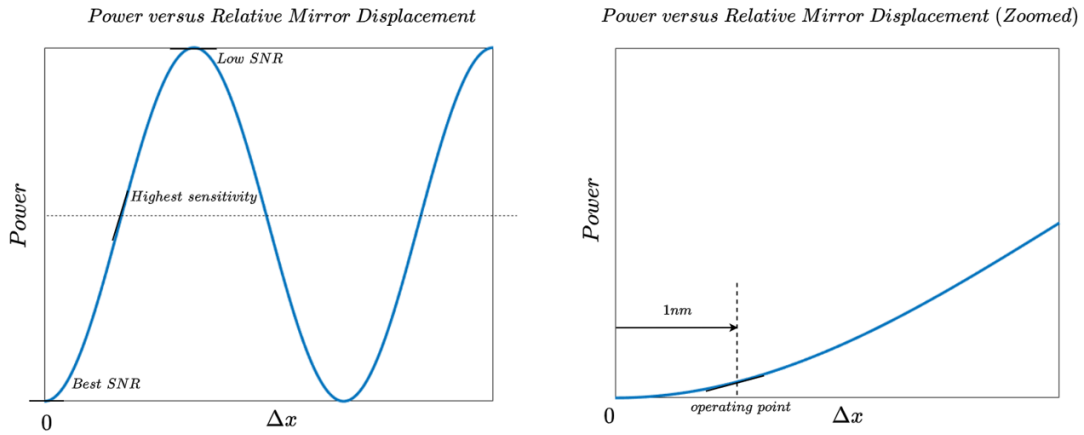

Figure 2.5: ET output power versus the relative mirror displacement

shifted a little bit to the right from the origin, such that the SNR is still very good. The telescope must stay in the linear region around the operating point and this limits the allowable relative displacement between the mirrors, denoted as ε. The linear region is about $\varepsilon = \frac{\Delta x_{@\text{operating point}}}{10} = 10^{-10}$m around the operating point.

The quality factor for the optical resonators is expressed as the finesse $\mathcal{F}$, which is analogous to the $\mathcal{Q}$ factor of a mechanical resonator. The higher the finesse, the better the light can resonate in the FP cavity and hence the better the sensitivity of the interferometer gets. The resonator effectively amplifies the difference in displacement between the mirrors by a factor of the finesse $(\Delta x \cdot \mathcal{F})$. The allowable mirror displacement to ensure that the interferometer stays within the linear regime of the telescope measurement is therefore scaled down by the finesse. With a value of $\mathcal{F} = 100$ for ET, the allowable deflection that stays within the linear region of the operating point is then about:

$$\varepsilon \approx \frac{\Delta x_{@\text{operating point}}}{10} \cdot \frac{1}{\mathcal{F}} \approx 10^{-12}\text{m} \tag{2.5}$$

For the LIGO and Virgo gravitational wave detectors, it appeared that practically, the admissible value of ε is about one order of magnitude lower than computed here. Throughout this research, a value of $\varepsilon = 1 \cdot 10^{-13}$m is assumed. For this reasoning, the RMS of the residual closed-loop seismic noise felt by the mirrors must be minimized. If not attenuated, the FP cavities are kept from their resonating condition the telescope does not operate in the linear region of the operating point. Gravitational waves remain immeasurable in that case. The suppression of the seismic noise by the global control system is commonly referred as *locking* the interferometer to its operating point.

2.3 Requirements for the Control System

We can define a set of requirements that fit the aforementioned problem, which can be translated into a quantitative description of the goals and limitations for the optimization study. Since the primary goal of the control system is the attenuation of the effects of seismic noise to the locking of the mirror, the first requirement may be expressed as follows.

> *The control system should minimize the RMS of the closed-loop seismic noise to a value smaller than $\gamma < \varepsilon$.*

The open-loop equivalence of the DAC noise may not exceed the ET design sensitivity curve, since this is the baseline performance of the Einstein Telescope. Since this research is focused on ET-LF specifically, the sensitivity curve of ET-LF forms a hard bound for the DAC voltage noise. Therefore, an additional requirement to extend the problem is formulated as such.

> *The open-loop equivalence of the DAC noise may not exceed the Einstein Telescope sensitivity curve, and should possibly stay well below this curve by a certain safety factor.*

One could argue that the stability of the system is also an important issue for the control system design. Since there are no specific design goals for stability margins yet, we can at least complement the latter requirements with the following.

The closed-loop control system, with the designed controller, should be asymptotically stable.

2.4 Motivating a Mixed $\mathcal{H}_2/\mathcal{H}_\infty$ Optimization Strategy

Often, in practice, the controllers for the mirror suspension of gravitational wave telescopes are tuned by hand. Any changes of the plant, updated noise budgets or changes in models of noise sources would then require a lot of effort to re-tune the controller. If the problem can be formulated into an optimization problem, in principle, an optimization algorithm can compute a suitable controller that meets the desired requirements if possible. Any change in the model of the plant or noise budget is known a priori, and computing a new controller then only requires an update of the optimization problem. An optimization algorithm should be able to compute a new optimal controller for the updated problem. This could in the end save a lot of design time when the control problem is formulated well, since the controller design will then be mostly automated. Moreover, this allows to explore the optimal performance of many different configurations of the suspension design space quickly. This is usually too labour intensive to do utilizing manual controller design techniques.

The minimization of the RMS of a closed-loop disturbance spectrum is indirectly a variance minimization based optimization. That is exactly what an $\mathcal{H}_2$-optimal controller should do: minimize the variance of the impulse response of the closed-loop transfer function that maps some disturbance input (seismic disturbances) to a specified output (motion of the mirror). The constraint on the open-loop equivalence of the DAC noise is a hard limit for the frequency spectrum of this noise source. Since the open-loop DAC noise should not exceed the noise budget for ET, we can view this requirement as an $\mathcal{H}_\infty$-norm on the open-loop equivalent DAC noise. Hence an $\mathcal{H}_\infty$-optimization is the most suitable strategy for this requirement. Moreover, it might be favourable to guarantee a certain robustness against unmodelled dynamics. We can often describe such a robustness requirement as an $\mathcal{H}_\infty$-bound on one or more closed-loop transfer functions.

The above illustrates that for a part of the problem, an $\mathcal{H}_2$-optimization is suitable for the problem. On the other hand an $\mathcal{H}_\infty$-optimization is fitting for the other part of the problem. The next sections will focus on how to cast this mixed control problem into a suitable optimization statement. This section also addresses the control loop architectures and important modelling choices.

Chapter 3

Modelling and Methodology

This chapter starts with the modelling of the suspension. The equations of motion of the suspension are used to define transfer functions that are used for the controller design. Besides the controller, the actuator distribution for the suspension is also optimized. In order to fulfill the DAC noise constraint that was posed in the previous chapter, the actuators should be sized accordingly. Proper sizing should maintain allowable amplification of the DAC noise. Choosing an appropriate sizing for the actuator at each stage is also done by the optimizer in question. Therefore, some detailing is given in this chapter about the actuation and estimation of the actuator dynamics.

Next, the architecture of the control loop is discussed. The optimization algorithms that were investigated are discussed to showcase why these methods can be suitable for the controller optimization of the ET mirror suspension control system. Also, models for the disturbances that enter the control loop are derived, as well as weighting functions, which are later used for the optimizations.

3.1 System Description and Modelling

The suspension of the mirror can be globally divided into three main parts: the Internal Seismic Isolation system (ISI), a passive filtering stage and finally the payload suspension. A schematic overview of the complete suspension for the test mass is shown in Figure 3.1.

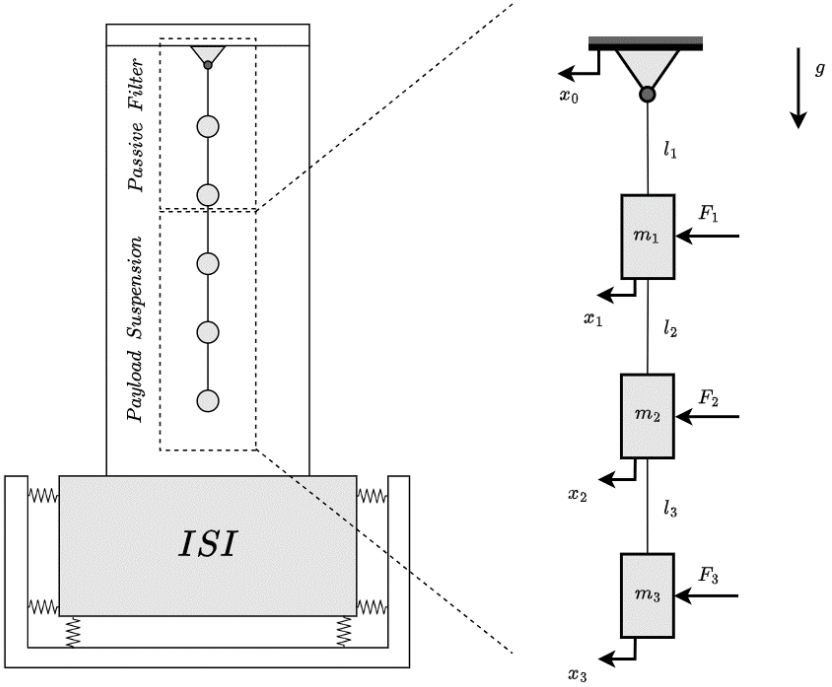

Figure 3.1: Schematic overview of the complete test mass suspension (left) and IPM of the payload suspension (right)

The ISI is an actively controlled platform that compensates for a part of the seismic disturbances. A large inverted pendulum follows the ISI, from which a multi-pendulum suspension is suspended. This set of pendulums consists of a passive filtering stage and finally the actively controlled payload suspension. The payload suspension compensates for any residual seismic disturbances that are left after the preceding vibration isolation stages. The bottom mass of the payload suspension is the mirror stage. The aim of this whole suspension chain is to isolate the mirror as much as possible from the fixed world. The payload suspension is the system that is considered for this study and the following paragraph addresses the derivation of the nominal dynamics of this subsystem.

Dynamics of the Payload Suspension

The payload suspension can be modelled with reasonable accuracy by a triple pendulum[1]. For now, it is assumed that the mirror is actuated at all three stages. The generalized coordinates for the system are the absolute angles of the pendulums. This is the angle between each pendulum stage and the vertical axis, counter-clockwise positive by convention. The full derivation of the equations of motion for the triple pendulum is given in Appendix A. The linearized dynamics of the triple pendulum are given by the following set of coupled equations of motion, assuming small angles:

$$(m_1+m_2+m_3)l_1^2\ddot{\theta}_1 + (m_2+m_3)l_1l_2\ddot{\theta}_2 + m_3l_1l_3\ddot{\theta}_3 + (m_1+m_2+m_3)gl_2\theta_1 = \xi_1 \tag{3.1}$$

$$(m_2+m_3)l_1l_2\ddot{\theta}_1 + (m_2+m_3)l_2^2\ddot{\theta}_2 + m_3l_2l_3\ddot{\theta}_3 + (m_2+m_3)gl_2\theta_2 = \xi_2 \tag{3.2}$$

$$m_3l_1l_3\ddot{\theta}_1 + m_3l_2l_3\ddot{\theta}_2 + m_3l_3^2\ddot{\theta}_3 + m_3gl_3\theta_3 = \xi_3 \tag{3.3}$$

$$\boxed{sin(\theta_\mathrm{i}) \approx \theta_\mathrm{i}, \quad cos(\theta_\mathrm{i}) \approx 1, \quad \dot{\theta}_\mathrm{i}\dot{\theta}_\mathrm{j} \approx 0} \tag{3.4}$$

[1]Initially, the dynamics of a double pendulum (2DoF) were investigated. It appeared that the direct actuation of the mirror does not provide sufficient roll-off to get both good seismic noise suppression and satisfying the open-loop requirement for the DAC noise.

The equations are linearized about the operating point $\theta_1 = 0$, $\theta_2 = 0$, $\theta_3 = 0$. Rewriting the dynamics in the general form of:

$$M(\boldsymbol{q})\ddot{\boldsymbol{q}} + C(\boldsymbol{q}, \dot{\boldsymbol{q}}) + g(\boldsymbol{q}) = \boldsymbol{\xi} \tag{3.5}$$

Yields the following set of equations.

$$\underbrace{\begin{bmatrix} (m_1+m_2+m_3)l_1^2 & (m_2+m_3)l_1l_2 & m_3l_1l_3 \\ (m_2+m_2)l_1l_2 & (m_2+m_3)l_2^2 & m_3l_2l_3 \\ m_3l_1l_3 & m_3l_2l_3 & m_3l_3^2 \end{bmatrix}}_{M(\boldsymbol{q})} \begin{bmatrix} \ddot{\theta}_1 \\ \ddot{\theta}_2 \\ \ddot{\theta}_3 \end{bmatrix} + \underbrace{\begin{bmatrix} (m_1+m_2+m_3)gl_1 & 0 & 0 \\ 0 & (m_2+m_3)gl_2 & 0 \\ 0 & 0 & m_3gl_3 \end{bmatrix}}_{g(\boldsymbol{q})} \begin{bmatrix} \theta_1 \\ \theta_2 \\ \theta_3 \end{bmatrix} = \boldsymbol{\xi} \tag{3.6}$$

The Coriolis matrix $C(\boldsymbol{q}, \dot{\boldsymbol{q}})$ disappears due to small velocities. The generalized coordinates of the system are the angles of the pendulum stages:

$$\boldsymbol{q} = \begin{bmatrix} \theta_1 \\ \theta_2 \\ \theta_3 \end{bmatrix} \tag{3.7}$$

The state-space form of the system with state vector $\boldsymbol{x} = [\boldsymbol{q}, \dot{\boldsymbol{q}}]^T$ is found as:

$$\dot{\boldsymbol{x}} = \begin{bmatrix} \dot{\boldsymbol{q}} \\ \ddot{\boldsymbol{q}} \end{bmatrix} = \begin{bmatrix} \dot{\boldsymbol{q}} \\ M^{-1}(\boldsymbol{q}) \cdot ((-g(\boldsymbol{q}) + \boldsymbol{\xi}) \end{bmatrix} \tag{3.8}$$

The state-space equation is rewritten in the standard form as:

$$\dot{\boldsymbol{x}} = A\boldsymbol{x} + B\boldsymbol{u} \tag{3.9}$$

$$\boldsymbol{y} = C\boldsymbol{x} + D\boldsymbol{u} \tag{3.10}$$

$$A = \begin{bmatrix} 0_{3\times3} & I_{3\times3} \\ -M^{-1}(\boldsymbol{q})g(\boldsymbol{q}) & 0_{3\times3} \end{bmatrix}, \quad B = \begin{bmatrix} 0_{3\times3} \\ M^{-1}(\boldsymbol{q})\boldsymbol{\xi} \end{bmatrix}, \quad C = \begin{bmatrix} l_1 & l_2 & l_3 & 0 & 0 & 0 \end{bmatrix}, \quad D = \begin{bmatrix} 0_{1\times3} \end{bmatrix} \tag{3.11}$$

The transfer function of the plant is then found from the state-space matrices as:

$$G(s) = C(sI - A)^{-1}B + D \tag{3.12}$$

The actuator dynamics $K_\mathrm{a}[N/V]$ are described by gains that represent the sizing of the actuators. The total transfer from controller voltage command to motion of the mirror is then described by $\tilde{G}(s) = G(s)K_\mathrm{a}$. Note that modelling the actuators with a gain is a simplification of the dynamics of the real actuator. Especially, high frequency actuator dynamics are neglected during this study. Since we are mainly concerned about the distribution of the actuation over the suspension stages, this simplification is justified. Also, the power spectrum of the seismic disturbance is situated in the low frequency regime of the frequency spectrum. Therefore, seismic noise attenuation will likely not be influenced by possible high frequency parasitic actuator dynamics.

3.2 Control and Optimization Strategies

The previous chapter argued that the control problem at hand can be described both in terms of an $\mathcal{H}_2$- and an $\mathcal{H}_\infty$-optimal framework. Although we aim to investigate the usability of a mixed $\mathcal{H}_2/\mathcal{H}_\infty$ optimization approach for the ET mirror suspension controller design, an introduction and understanding of the optimization approaches separately is important as the principles that define them are still present in the mixed approach to some extent. All of the approaches have in common that they aim to minimize either the $\mathcal{H}_2$- or $\mathcal{H}_\infty$-system norm of selected closed-loop transfer functions. For the next sections, the transfer function $T_{\mathrm{w}\to\mathrm{z}}(s)$ is the closed-loop mapping from an arbitrary set of exogenous inputs $\boldsymbol{w}$ to an arbitrary set of weighted performance outputs $\boldsymbol{z}$. Consider the standard generalized plant configuration of Figure 3.2, which is often used for optimal control problems.

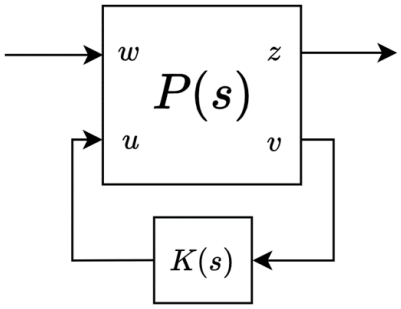

Figure 3.2: Standard generalized plant block diagram

Where $P(s)$ is the generalized plant. Since the controller $K(s)$ should be optimized, it is pulled out of the loop to form a path that maps controller inputs $\boldsymbol{v}$ to controller outputs $\boldsymbol{u}$. The closed-loop transfer function $T_{\mathrm{w}\to\mathrm{z}}(s)$ is the linear fractional transformation of $P(s)$ and $K(s)$ that maps $\boldsymbol{w} \to \boldsymbol{z}$. $P(s)$ is then a linear mapping as follows:

$$\begin{bmatrix} \boldsymbol{z} \\ \boldsymbol{v} \end{bmatrix} = P(s) \begin{bmatrix} \boldsymbol{w} \\ \boldsymbol{u} \end{bmatrix} \tag{3.13}$$

3.2.1 $\mathcal{H}_2$-Optimal Control

Controllers that are synthesized via $\mathcal{H}_2$-optimization are generally designed such that they minimize the variance of some defined closed loop signal. Consider again the generalized plant configuration of Figure 3.2, where the generalized plant is denoted as $P(s)$. The minimization the $\mathcal{H}_2$-norm of a selected transfer function leads to the minimization of the mapping transfer function $T_{\mathrm{w}\to\mathrm{z}}(s)$ from a disturbance $\boldsymbol{w}$ to performance output $\boldsymbol{z}$ or in other words:

> *The $\mathcal{H}_2$-optimal controller $K(s)$ is a stabilizing controller that minimizes the $\mathcal{H}_2$-norm of the closed loop $T_{\mathrm{w}\to\mathrm{z}}(s)$ such that the power of the performance outputs $\boldsymbol{z}$ is minimized for inputs $\boldsymbol{w}$ that have a unitary white noise spectrum.*

The performance channels can be weighted by frequency dependent weighting filters $W_2(s)$ to emphasize a minimization over specified frequency range. An $\mathcal{H}_2$-optimization thus aims to minimize the variance of closed-loop control signals that are selected by a designer. $\mathcal{H}_2$-control generally holds for exogenous inputs $\boldsymbol{w}$ that have a unitary white power spectrum.

3.2.2 $\mathcal{H}_\infty$-Optimal Control

The other type of well known optimization is the $\mathcal{H}_\infty$-optimal controller design. In general, the objective for this optimization is to minimize the $\mathcal{H}_\infty$-system norm of selected weighted closed loop transfer functions. The designer must design, possibly frequency dependent, weighting filters $W_\infty(s)$, such that the weighted closed-loop transfer function or transfer function matrix has an $\mathcal{H}_\infty$-norm less than one. Here, the $\mathcal{H}_\infty$-norm is the maximum singular value of a transfer function [21][38]:

$$|W_\infty(s)T_{\mathrm{w}\to\mathrm{z}}(s)| = |W_\infty(s)||T_{\mathrm{w}\to\mathrm{z}}(s)| \leq 1 \quad \to \quad |T_{\mathrm{w}\to\mathrm{z}}(s)| \leq |W_\infty^{-1}(s)| \tag{3.14}$$

Thus, if feasible, the optimal controller $K(s)$ should ensure that the gain of the closed-loop transfer function $T_{\mathrm{w}\to\mathrm{z}}(s)$ is lower than the inverse of the weighting filter $W_\infty(s)$ over the complete frequency range. So in words:

> *The $\mathcal{H}_\infty$-optimal controller $K(s)$ is a stabilizing controller that minimizes the $\mathcal{H}_\infty$-norm of a selected weighted closed-loop transfer function $W_\infty(s)T_{w\to z}(s)$, such that the closed-loop transfer function $T_{w\to z}(s)$ is limited in gain by designer specified frequency dependent weighting filters $W_\infty(s)$.*

Often, the stability margins or the robustness of a system can be specified as an $\mathcal{H}_\infty$-norm. Therefore, this type of optimization lends itself very well to ensure some desired robustness margin for the closed-loop system. Also, $\mathcal{H}_\infty$-optimal control generally holds for exogenous inputs $\boldsymbol{w}$ that have a unitary white power spectrum.

3.2.3 Mixed $\mathcal{H}_2/\mathcal{H}_\infty$-Optimal Control

The problem definition of the previous chapter posed the basic requirements for the control system. On the one hand, the objective is to minimize the RMS of the closed-loop seismic noise. This is necessary in order to keep the telescope within its linear operating range such that the resonating condition of the FP cavities is maintained. Minimizing the $\mathcal{H}_2$-norm of closed-loop systems minimizes the power of selected output error signals. This effectively minimizes the RMS of these error signals [38]. From this, it can be concluded that an $\mathcal{H}_2$-optimization is the most suitable paradigm for designing controllers concerning this goal. Generally, the $\mathcal{H}_2$ framework does not provide any way to ensure a certain stability or robustness margin, resulting in closed-loop systems that often have small stability margins [20].

On the other hand, the requirement for the open-loop equivalent spectrum of the DAC noise poses a hard limit on the DAC noise that enters the control loop via the actuators. This hard limit typically manifests as an $\mathcal{H}_\infty$-norm. Since the problem specifically describes a frequency dependent limit on the open-loop equivalent DAC noise, an appropriate $\mathcal{H}_\infty$-weight should be applied to the open-loop equivalent spectrum of the DAC noise. Additional robustness requirements are also reflected well by an $\mathcal{H}_\infty$-constraint. This allows to obtain a closed-loop system that is more robust against process variations than what a typical $\mathcal{H}_2$-optimal controller is able to achieve.

The aim of the control system can thus be expressed in terms of both the $\mathcal{H}_2$ and the $\mathcal{H}_\infty$ framework. Hence, the separate strategies that were described in paragraphs 3.2.1 and 3.2.2 are not sufficient by themselves to find a solution that satisfies all requirements directly. In this work, a mixed $\mathcal{H}_2/\mathcal{H}_\infty$ approach is investigated, since this seems to fit the control challenge the most. Typically, this mixed framework results in an optimization problem for which the associated cost function is not convex anymore. The solution cannot be found by solving a set of Ricatti equations, as for $\mathcal{H}_2$ and $\mathcal{H}_\infty$-control problems. There exist methods to convexify this mixed optimization. However, methods that do this are often numerically poorly conditioned and often lead to conservative controller design [24]. To avoid this, in this research, the controllers are computed by an algorithm that utilizes a non-smooth optimization approach. This method finds minima of the associated cost function via an iterative gradient descent method, where the direction of the steepest descent of the cost is computed via the gradient of the cost function [12][11]. This might lead to the localization of a local minimum instead of a global minimum. Exploring the parameter space at multiple starting points can lead to the localization of multiple local minima. Local minima could nevertheless still provide a solution that meets the requirements. Consider the block diagram of of Figure 3.3, which will act as the starting point of the control problem formulation. A standard feedback loop with open-loop plant $\tilde{G}(s)$ and feedback controller $K(s)$ is considered. The DAC noise u_d and seismic disturbance x_d are considered to be the most significant noise sources.

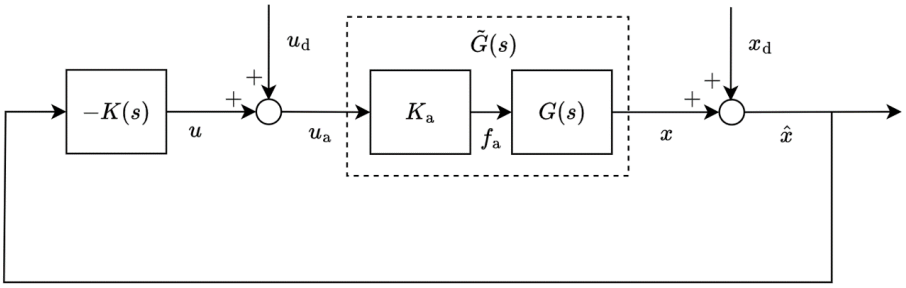

Figure 3.3: Block diagram of the global feedback control system

Block Diagram and Mathematical Formulation of the Optimization

Consider the block diagram of the generalized plant configuration for a general mixed synthesis problem of Figure 3.4. Besides the controller $K(s)$, we also take the actuator dynamics K_a out of the loop to include them in the optimization. The generalized plant $P(s)$ is defined as the open-loop mapping from the concatenated vector of exogenous inputs $\boldsymbol{w}$, actuator forces $\boldsymbol{f_\mathrm{a}}$ and controller output $\boldsymbol{u_\mathrm{c}}$ to the performance outputs $\boldsymbol{z}$, actuator voltage $\boldsymbol{u_\mathrm{a}}$ and controller input $\boldsymbol{y_\mathrm{c}}$.

$$\begin{bmatrix} \boldsymbol{u_a} \\ \tilde{\boldsymbol{z}} \\ y_c \end{bmatrix} = \boldsymbol{P(s)} \cdot \begin{bmatrix} \boldsymbol{f_a} \\ \tilde{\boldsymbol{w}} \\ \boldsymbol{u_c} \end{bmatrix}, \qquad \tilde{\boldsymbol{w}} = \begin{bmatrix} x_d \\ \boldsymbol{u_d} \end{bmatrix}, \qquad \tilde{\boldsymbol{z}} = \begin{bmatrix} x \\ \hat{x} \\ \boldsymbol{u_c} \end{bmatrix} \tag{3.15}$$

Where the exogenous disturbances consist of the seismic noise $x_d(s)$ and DAC noise $u_d(s)$. The performance channel $\boldsymbol{z}$ consists of selected $\mathcal{H}_2$-weighted control signals $\boldsymbol{z_2(s)}$ and $\mathcal{H}_\infty$-weighted control signals $\boldsymbol{z_\infty(s)}$. The frequency dependent weighting filters that make up $W(s)$ are discussed separately later in this chapter. The optimization methodologies that were discussed in Section 3.2.1 and 3.2.2 only hold for exogenous inputs that have a unitary white power spectrum. Since the realistic disturbances typically do not have a white power spectrum, a matrix $V(s)$ with noise models on the diagonal is included. The entries of this matrix colour white noise such that the disturbances correspond with the real disturbances [26]. The design of each entry of $V(s)$ is discussed in the subsequent chapter.

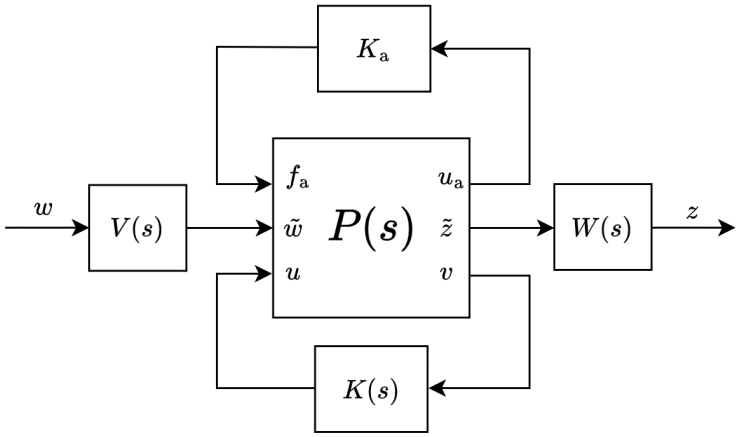

Figure 3.4: Generalized plant configuration

The optimization algorithm thus aims to compute a controller $K(s)$, such that the $\mathcal{L}_2$-norm of the effective closed-loop seismic noise at the mirror is minimized. The DAC noise is limited by the appropriate weighting filter, such that it does not exceed some defined frequency dependent limit. This combination of $\mathcal{H}_2$ and $\mathcal{H}_\infty$ is the baseline optimization that is considered throughout this study.

> *The control system should attenuate the seismic disturbances in terms of a closed-loop root mean square minimization as long as the open-loop DAC noise injection to the system does not exceeds its admissible limits. Both the controller and the actuator dynamics can be optimized to achieve this goal.*

Additionally, it might be necessary to constrain the voltages as computed by the controller with an $\mathcal{H}_2$-constraint, to ensure that they are within the capabilities of the DAC. Typically, any robustness constraints manifest as an $\mathcal{H}_\infty$-channel and might be assigned to guarantee a certain pre-specified robustness margin to account for process variations. Let $V_u(s)$ and $V_x(s)$ be the noise colouring filters for the DAC noise and seismic disturbance respectively. $W_u(s)$, $W_{dac}(s)$ and $W_p(s)$ are (possibly frequency dependent) weighting filters concerning the control signal, open-loop equivalent DAC noise and seismic disturbance rejection respectively. The block diagram of Figure 3.3 is then extended with the noise models and weighted $\mathcal{H}_2$ and $\mathcal{H}_\infty$-channels as shown in Figure 3.5. Notice that this block diagram includes the inverse of the sensitivity function $S(s)$ for the DAC noise optimization path. The sensitivity function is defined as follows

$$S(s) = (I + G(s)K_aK(s))^{-1} \tag{3.16}$$

The $\mathcal{H}_\infty$-constraint is a bound on the open-loop equivalent spectrum of the DAC noise. According to Equation 2.3, the open-loop equivalence of the DAC noise is then effectively found by multiplying the closed-loop DAC noise with the inverse of the sensitivity function. Notice that the loop gain here is equal to $L(s) = G(s)K_aK(s)$.

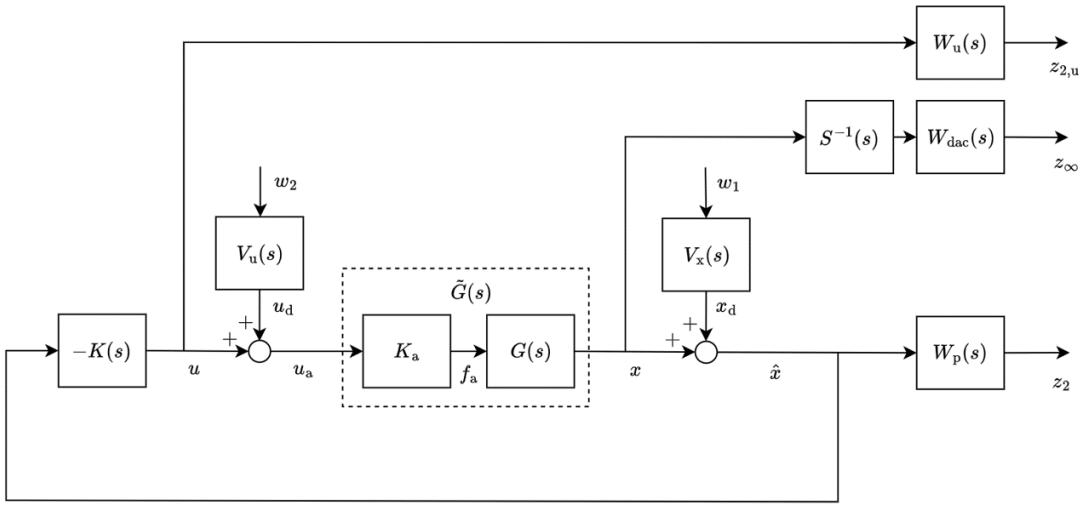

Figure 3.5: Block diagram for the payload suspension, including the weighting filters

3.3 Modelling of the Noise Sources

The noise sources that are considered for this study do typically not have a unitary white power spectrum. Therefore it was argued that the block-diagram of Figure 3.4 should include a matrix with LTI noise models $V(s)$. The entries of $V(s)$ colour white noise to a spectrum that resembles the actual noise source that will be present for the control system. A block diagram for this colouring of white noise $w_{\mathrm{w}}(s)$ to the actual disturbance $w(s)$ is shown in Figure 3.6. The filter $V_{\mathrm{w}}(s)$ is designed such that the Power Spectral Density (PSD) of the coloured noise $w(s)$ is related to the magnitude of the filter as:

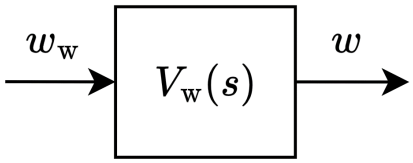

Figure 3.6: Block diagram of colouring white noise to a desired spectrum

$$S_{\mathrm{w}}(j2\pi f) = |V_{\mathrm{w}}(j2\pi f)|^2 \cdot S_{\mathrm{w_w}}(j2\pi f) \tag{3.17}$$

The next paragraphs will develop noise models for the seismic disturbance and the DAC noise. These noise models are shown in Figure 3.5 as $V_{\mathrm{x}}(s)$ and $V_{\mathrm{u}}(s)$ respectively. Moreover, an approximate model for the ET-LF noise budget is made, which is the base-line noise budget design of ET. All these models are part of the optimization problem statement.

3.3.1 Seismic Disturbance

The seismic activity of the earth's surface induces vibrations at the base of the suspension. The seismic motion of the earth propagates via the seismic isolation table, through the passive suspension finally to the payload. There are no measurements of the intermittent stages, only of the position of the mirror, such that disturbances to the mirror from sensing device artefacts are minimized. The effect of the seismic noise to the mirror is a known model, derived from [32]. The actual motion of the mirror is then modelled as a convolution of the seismic noise with the dynamics. The noise model for the seismic noise thus includes the dynamics of the suspension, such that the noise can be added at the output of the plant.

The effect of the seismic noise at the mirror is a combination of a rotational and translational vibratory component. This is due to that the floor both translates and rotates locally due to seismic vibrations. For both components, the transfer from disturbance of the base of the pendulum to the mirror motion is known. The PSD of the total disturbance can be computed as the superposition of the rotational and translational component as:

$$S_{\mathrm{x}}(j2\pi f) = |H_{\rightarrow}(j2\pi f)|^2 \cdot S_{\rightarrow}(j2\pi f) + |H_{\curvearrowleft}(j2\pi f)|^2 \cdot S_{\curvearrowleft}(j2\pi f) \tag{3.18}$$

Where the transfer function $H_{\rightarrow}(j2\pi f)$ is the transfer from translational seismic disturbance to the mirror's longitudinal degree of freedom, with $S_{\rightarrow}(j2\pi f)$ as the corresponding disturbance spectrum. Similarly, $H_{\curvearrowleft}(j2\pi f)$ is the transfer from rotational seismic disturbance to the motion of the mirror, with corresponding disturbance spectrum $S_{\curvearrowleft}(j2\pi f)$. The total spectrum of the seismic disturbance $S_{\mathrm{x}}(j2\pi f)$ and the corresponding approximate filter $V_{\mathrm{x}}(j2\pi f)$ is shown in Figure 3.7. The seismic noise spectrum is manually fitted with a low order LTI model $V_{\mathrm{x}}(s)$ as:

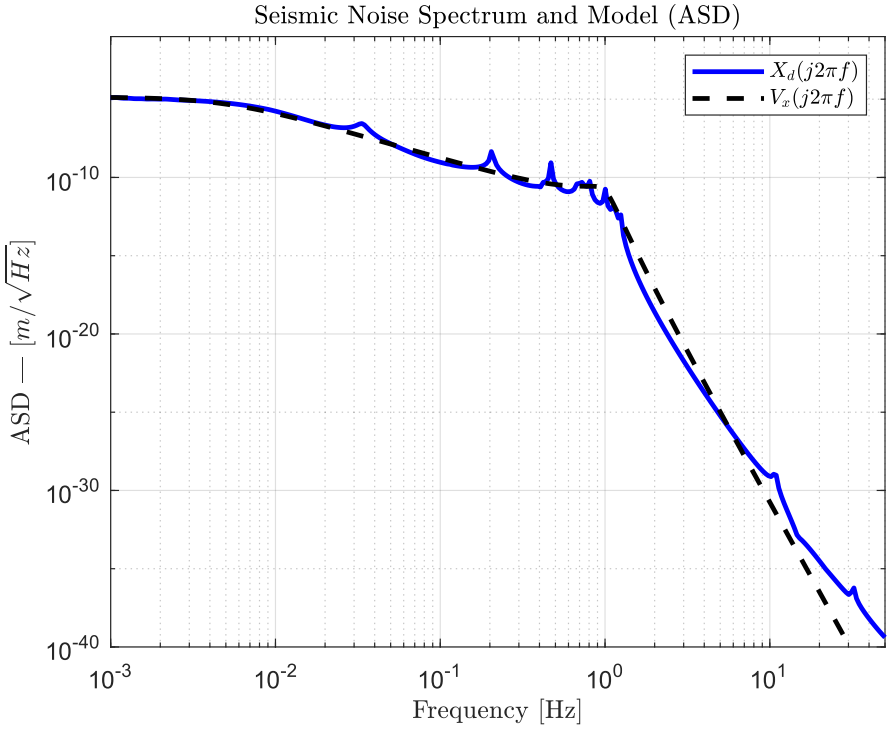

Figure 3.7: Total seismic disturbance at the mirror and corresponding filter model

$$V_{\mathrm{x}}(s) = \frac{2497.2}{(s+0.03)^3(s^2+8.63s+39.48)^2(s^2+7.31s+39.48)^2(s^2+4.89s+39.48)^2(s^2+1.72s+39.48)^2} \tag{3.19}$$

To make sure that the optimizer tries to minimize the actual disturbance $X_{\mathrm{d}}(j2\pi f)$ as best as possible, the RMS of the actual disturbance and the disturbance model $V_{\mathrm{x}}(j2\pi f)$ are matched.

3.3.2 Actuator Electronic Noise

The actively controlled suspension requires actuators and this inevitably introduces additional noise to the system. The main reason for this noise is due to the nature of the electrical components that drive the actuator. Typically, this electrical noise is a combination of flicker noise, thermal noise and shot noise:

- **Flicker Noise:** is mostly induced by semiconductors that are present in electronic circuits. The PSD of flicker noise is proportional to the inverse of the frequency, hence it is mostly significant at lower frequencies.
- **Thermal Noise:** is mostly due to the vibration of electrons. This noise source is proportional to the temperature of the electrical component. This noise source typically has a white spectrum and hence has a flat PSD.

- **Shot Noise:** is due to the discrete nature of currents in an electrical device. A current consists of individually moving charges that flow through a conductor discretely. The flow of these individual charges results in shot noise, which can be modelled as white noise with a flat PSD.

The frequency spectrum of electrical noise from the Digital to Analog Converter (DAC) is often a combination of these noise sources, as shown in Figure 3.8.

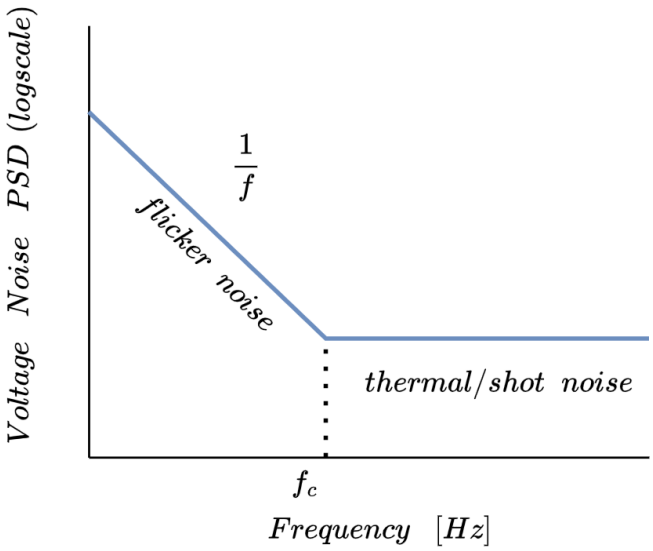

Figure 3.8: Typical spectrum for electrical noise

Figure 3.9 shows a known noise model that closely resembles the electrical noise spectrum of the noise that is present for the actuator drives [25]. The noise spectrum is approximated by the filter $V_{\mathrm{u}}(s)$. The electrical noise can be closely resembled by a filter with a pole at the origin and a zero placed at the cut-off frequency at which the spectrum goes to flat.

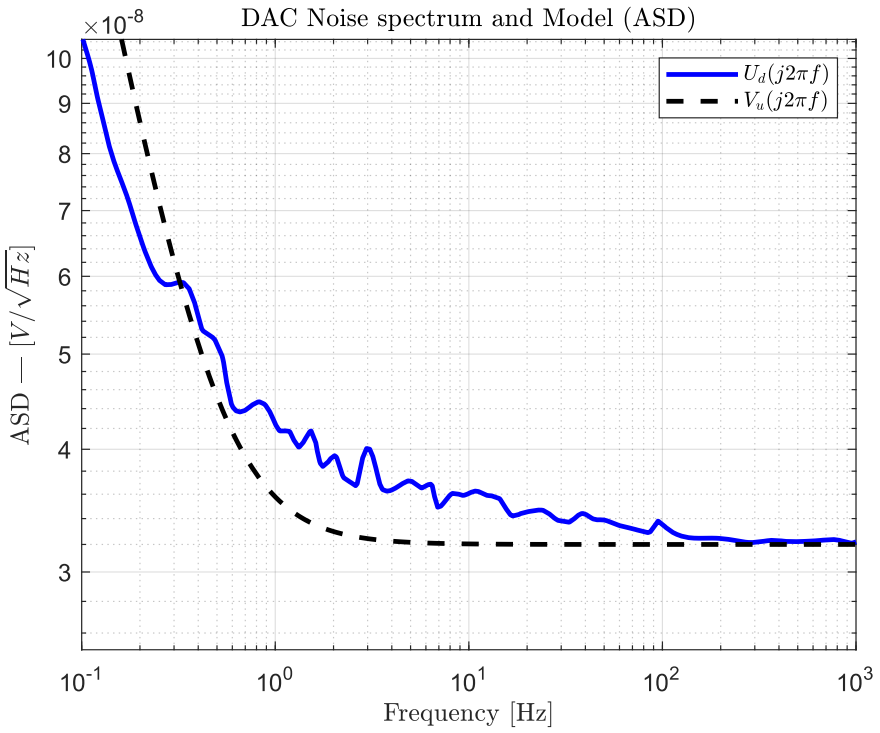

Figure 3.9: DAC noise spectrum and corresponding filter model

$$V_{\mathrm{u}}(s) = K \cdot \frac{(s + 2\pi f_{\mathrm{c}})}{s} \tag{3.20}$$

From Figure 3.9 it can be inferred that the actual spectrum can not be approximated by an integer order filter, hence a first order model is used to approximate the DAC noise as close as possible. The transfer function of the filter $V_{\mathrm{u}}(s)$ from Figure 3.9 was found as:

$$V_{\mathrm{u}}(s) = \frac{3.20 \cdot 10^{-8}(s + 3.14)}{s} \tag{3.21}$$

The RMS value of the model $V_{\mathrm{u}}(j2\pi f)$ and the measured spectrum $U_{\mathrm{d}}(j2\pi f)$ are also matched in value.

3.3.3 ET-LF Noise Budget

In Chapter 2.1 it was shown how the overall performance of ET as a measuring device is given by its sensitivity curve. This curve can be considered as a hard limit, which other noise sources may not exceed. The noise budget is reflected as an open-loop equivalence, much like the occurrence of the open-loop equivalence of the DAC noise that was encountered in Chapter 2. This curve will appear as an $\mathcal{H}_\infty$-constraint for the DAC noise. Therefore, a model is created that resembles the ET-LF noise budget with sufficient accuracy.

Figure 3.10 shows the ET-LF design sensitivity curve. The filter $W_{\mathrm{ET-LF}}(s)$ is designed by combining two inverse Butterworth filters and four poles at the origin to obtain the low frequency slope of -80dB per decade below a frequency of 10Hz. The approximate filter is shown in Figure 3.10.

$$W_{\mathrm{ET-LF}}(s) = \left[\frac{2.7 \cdot 10^{-19}\left(s^2 + 41.5s + 1421\right)^2\left(s^2 + 131.9s + 3.6 \cdot 10^4\right)}{s^4}\right]^{-1} \tag{3.22}$$

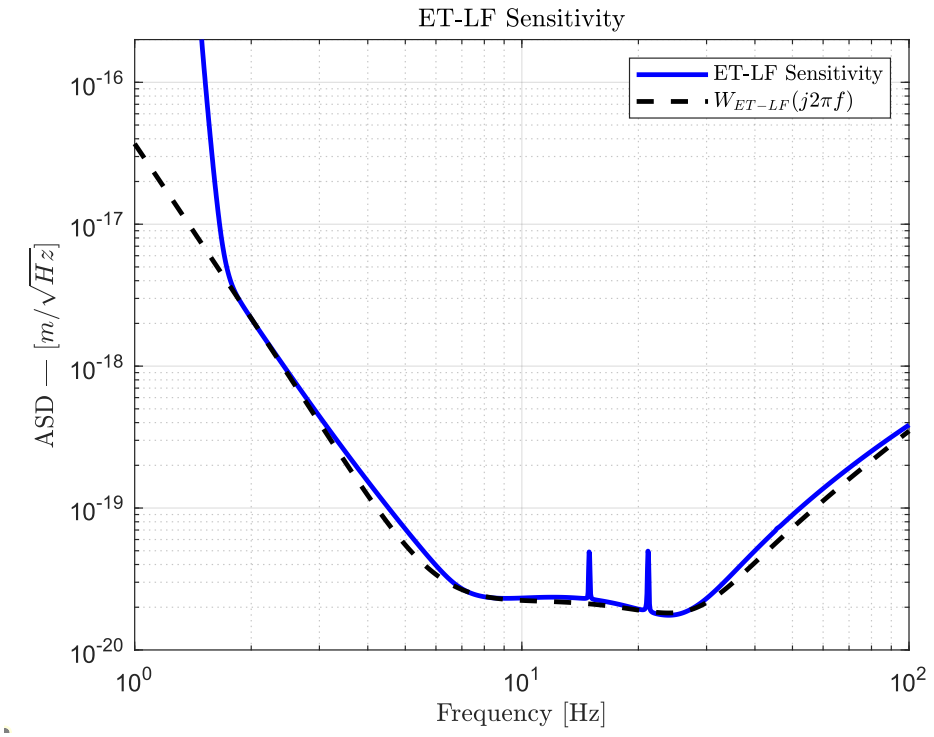

Figure 3.10: ET-LF sensitivity curve and corresponding approximate filter

3.3.4 Other Noise Sources

There exist other noise sources that are usually considered for the design of high precision control systems. Among these are sensor noise and quantization noise, of which both are not considered during this study.

This paragraph aims to illustrate the reason for omitting these noise sources, that are present for any control system after all.

3.3.5 Quantization Noise

Almost every controller is implemented digitally these days. The measurement signals from sensors are periodically sampled and usually a control signal is computed and kept constant for one sample time. The digital controller output is then converted by a DAC and an analog voltage is applied to the actuators. Because the controller is digital, there are only a finite number of discrete values which the control action can take, dictated by the number of bits that are available for the DAC. This requires rounding of the ideal value to the nearest quantized value. The difference between the rounded value and the ideal value results in a quantization error. It turns out that this noise source can be modelled as a white noise spectrum, with a spectrum computed as [34]:

$$S_{\mathrm{qe}}(j2\pi f) = \frac{2^{-2B} X_{\mathrm{m}}^2}{12} \tag{3.23}$$

With X_{m} the voltage range of the DAC and B the number of bits available for the DAC. One can easily see that the noise spectrum decreases significantly with the number of bits. Generally, the DAC's that are used for gravitational wave observatories have sufficient bits available such that the quantization noise may be assumed to be negligible compared to other noise sources.

3.3.6 Sensor Noise

A gravitational wave enters the control loop similarly to the seismic disturbances and therefore, the gravitational wave must be reconstructed from control signals from the loop. The interferometric sensing setup, that indirectly measures the relative displacement of the mirror, is designed such that ET as a sensor is the base-line performance of what it can measure. Basically, the ET-LF noise budget from Figure 3.10 can be seen as the effective sensor noise. Since this is the best we can measure nonetheless, the effects of the sensor noise are usually ignored for controller design for these types of equipment.

3.4 Weighting Filter Design

Although the design of the weighting filters for controller synthesis are tuned a bit during the design process, the overall shape of the filters is already mostly dictated by the type of problem that was described above. The optimization incorporates both $\mathcal{H}_2$- and $\mathcal{H}_\infty$-synthesis and the matrix $W(s)$ therefore consists of $\mathcal{H}_2$ related filters $W_2(s)$ and $\mathcal{H}_\infty$ related filters $W_\infty(s)$.

$\mathcal{H}_2$-channel Weighting Filters

The first entry of the z_2-performance channel is applied to the closed-loop seismic noise, since it is the main objective to minimize the RMS of this signal. It can be expected that an optimization that minimizes the variance of a closed loop signal will compute a controller with high gains at frequencies where the seismic noise should be attenuated. Therefore, a simple gain should suffice as an $\mathcal{H}_2$-bound regarding the closed-loop seismic noise:

$$W_{\mathrm{p}}(s) = k_{\mathrm{p}} \tag{3.24}$$

Since it might be necessary to ensure that the control signal $\boldsymbol{u(s)}$ stays within the capacity of the DAC and the actuators, an additional weight on this signal is proposed in the form of a matrix with a gain related to each entry as follows:

$$W_{\mathrm{u}}(s) = \mathrm{diag}(\{k_{\mathrm{u}_1}, k_{\mathrm{u}_2}, k_{\mathrm{u}_3}\}) \tag{3.25}$$

$\mathcal{H}_\infty$-channel Weighting Filters

The main trade-off in the optimization exists between the attenuation of the residual seismic noise at one hand, while keeping the open-loop equivalence of the DAC noise low enough such that it does not exceed the sensitivity curve of the telescope. A logical constraint $W_{\mathrm{dac}}(s)$ that should be applied to the

open-loop equivalence of the DAC noise is then exactly the inverse of the sensitivity curve. Since the $\mathcal{H}_\infty$-optimal solution mathematically tries to achieve the following:

$$|W_{\text{dac}}(s)G(s)K_{\text{a}}V(s)|_\infty < 1 \tag{3.26}$$

The open-loop equivalence should stay below the inverse of $W_{\text{dac}}(s)$, which then is exactly the noise budget design again. A logical choice of the filter is thus:

$$W_{\text{dac}}(s) = W^{-1}_{\text{ET-LF}}(s) \tag{3.27}$$

Finally, an additional robustness constraint is proposed, which manifests as a second $\mathcal{H}_\infty$-weight. It is suggested to maintain a desired distance between the loop gain $L(s)$ and the critical point in the Nyquist plot, to account for process variations. This distance, otherwise known as the modulus margin, is directly related to the peak gain of the sensitivity function $S(s) = (1 + L(s))^{-1}$ as follows:

$$\text{MM} = \frac{1}{|S(s)|_\infty} \tag{3.28}$$

Therefore, the $\mathcal{H}_\infty$-bound on the sensitivity function is applied to guarantee a desired modulus margin $\text{MM}_{\text{req}} = \alpha$, which is described as:

$$W_{\text{rob}}(s) = \alpha \tag{3.29}$$

Such that the nominal sensitivity peak does not exceed a value of $1/\alpha$ which in turn ensures that the desired modulus margin is guaranteed.

Noise Colouring and Weighting Filter

The generalized plant of Figure 3.4 included a noise colouring filter matrix $V(s)$ and a weighting filter matrix $W(s)$. The diagonal entries of these filters are occupied with the filters that were derived above. The weighting filter matrix $W(s)$ is then:

$$W(s) = \text{diag}(\{W_{\text{p}}, W_{\text{u}}, W_{\text{dac}}, W_{\text{rob}}\}) \tag{3.30}$$

The noise colouring filter matrix is then given by the diagonal matrix:

$$V(s) = \text{diag}(\{V_{\text{x}}, V_{\text{u}}\}) \tag{3.31}$$

Now that we have a full description of the control problem at hand, a corresponding optimization statement can be identified accordingly. The next chapter shows the results of mixed synthesis studies for the control problem, that use the models that are derived in this chapter.

Chapter 4

Results

This chapter discusses the main findings of this research. First, the results for a pendulum with actuation at only two stages is shown in Chapter 4.1. This is followed by a similar study for a three degree of freedom pendulum that is actuated at all stages. The main findings of the research are summarized in paper form, shown in Chapter 4.2. This paper reflects the baseline optimization that aims to answer the main research questions that support this study. Namely, it opts to answer the question the whether mixed controller optimization via non-smooth optimization methods is suitable for gravitational wave applications.

Besides these baseline optimizations, some relevant extensions of this optimization were carried out. These extensions explore the capabilities of the optimizer to join both controller and mechatronic design of the plant in an integrated way. The extensions that are considered involve the optimization of the pendulum length topology and an optimization of the complete dynamics.

4.1 Optimization with Actuation at Two Stages

Figure 3.5 shows the block diagram that is associated with the control problem formulation. The weighting filter design was already discussed in Section 3.4. These weights are used in the optimization statements that are showed in the subsequent chapters.

Let $F_{\mathrm{l}}(P, K, K_{\mathrm{a}})$ denote the linear fractional transformation of the plant, controller and actuator dynamics. This transfer function is a closed-loop mapping that maps the exogenous disturbances $\tilde{w}$ to performance outputs $\tilde{z}$. where $\tilde{w} = [x_{\mathrm{d}}\ u_{\mathrm{d}}]^T$ and $\tilde{z} = [u\ x\ \hat{x}]^T$ The transfer function $S(s)$ is the the sensitivity function. The optimizer is required to maintain a modulus margin of 0.1, hence $W_{\mathrm{rob}} = 0.1$ Then, mathematically, the optimization problem is summarized in Equation 4.1.

$$\boldsymbol{\Theta} = \underset{\text{K stabilizing}}{argmin}\ \|W_{\mathrm{p}}(s)F_{\mathrm{l}}(s)V(s)\|_2, \qquad s.t. \tag{4.1}$$

$$\|W_{\mathrm{u}}(s)F_{\mathrm{l}}(s)V(s)\|_2 \leq \gamma_{\mathrm{u}} \qquad \|W_{\mathrm{rob}}(s)S(s)I\|_\infty \leq \gamma_{\mathrm{r}}, \qquad \|W_{\mathrm{dac}}(s)\tilde{G}(s)V_{\mathrm{u}}(s)\|_\infty \leq \gamma_{\mathrm{d}}$$

$$K_{\mathrm{a,l}} \leq K_{\mathrm{a}} \leq K_{\mathrm{a,u}}$$

Where the sizing of the actuators is bounded by a lower limit $K_{\mathrm{a,l}}$ and upper limit $K_{\mathrm{a,u}}$. The problem is thus stated as:

> *Find a stabilizing controller $K(s)$ and actuator distribution K_{a} that minimizes the $\mathcal{H}_2$-norm of $T_{\mathrm{w_2 \to z_2}}(s)$, for all $K(s)$ satisfying the $\mathcal{H}_\infty$-constraints.*

Where w_2 and z_2 are the disturbances and performance outputs that are related to the $\mathcal{H}_2$-channels respectively. The controller is a fixed order state-space. If the controller state-space is defined as:

$$K(s) \overset{s}{=} \left[\begin{array}{c|c} A_{\mathrm{k}} & B_{\mathrm{k}} \\ \hline C_{\mathrm{k}} & D_{\mathrm{k}} \end{array}\right] \tag{4.2}$$

The $B_{\mathrm{k}}, C_{\mathrm{k}}, D_{\mathrm{k}}$ matrix are fully tunable and the sub, super and main diagonal of the A_{k} matrix are tunable. Presumably, the optimization is then unique. A fully tunable state-space for a certain transfer is never unique. The controller computed via $\mathcal{H}_2$-synthesis, without $\mathcal{H}_\infty$-constraints, is used as an initial controller, shown in Appendix D. The controller from this study is computed for a generalized plant with 28 states, hence this is also the size of the controller that is used for the mixed synthesis.

Starting the Optimization at Multiple Points in the Optimization Space

The controller, resulting from the optimization stated in Equation 4.1, is expected to be sub-optimal, since the optimization problem is not convex. It is therefore likely that the solution that the optimizer converges to is not globally optimal, such that the γ values for the $\mathcal{H}_\infty$-channels are not close to one. Appendix B illustrates why this could be the case. The optimizer allows to initiate the optimization at multiple points in the optimization space. Therefore, the optimization is started at a sufficient amount of points in the optimization space to make sure that the resulting controller and actuator distribution is (almost) globally optimal. There is not a clear way to quantify whether the result is (almost) globally optimal, however the result with the lowest γ values was chosen.

4.1.1 Results from the Optimization Study

The main aim of the control system is to minimize the effects of the closed-loop seismic disturbance. Figure 4.1 shows the Cumulative Amplitude Spectrum (CAS) of the actual closed-loop seismic disturbance X_{d}. The ASD is integrated from high to low frequency to obtain this plot, which is considered standard within gravitational wave science. Typically, an RMS of $|x_{\mathrm{d,cl}}|_{\mathrm{rms}} < 1 \cdot 10^{-13}$m is required as a performance measure for the active suspension. From the figure, we can see that this criterion is not met, since $|x_{\mathrm{d,cl}}|_{\mathrm{rms}} = 4.56 \cdot 10^{-13}$m.

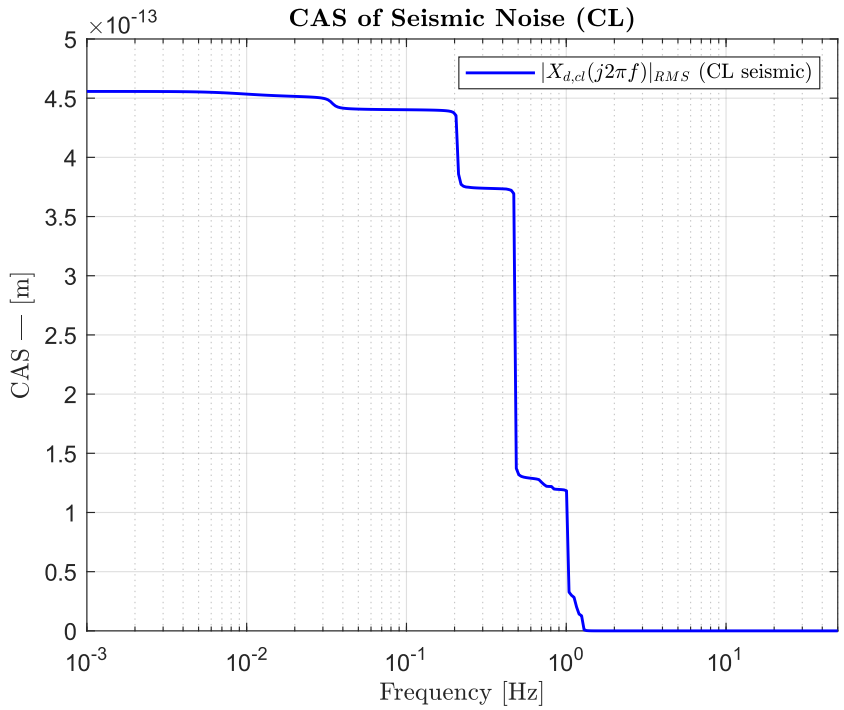

Figure 4.1: CAS of the of the closed-loop seismic disturbance

Figure 4.2 shows the singular values of the weighted open-loop DAC optimization channel. From this figure, we can see that the value of $\gamma_{\mathrm{d}} = 1.02$ at a frequency of 2Hz is close to one, which is something that can be expected for an $\mathcal{H}_\infty$-optimal solution.

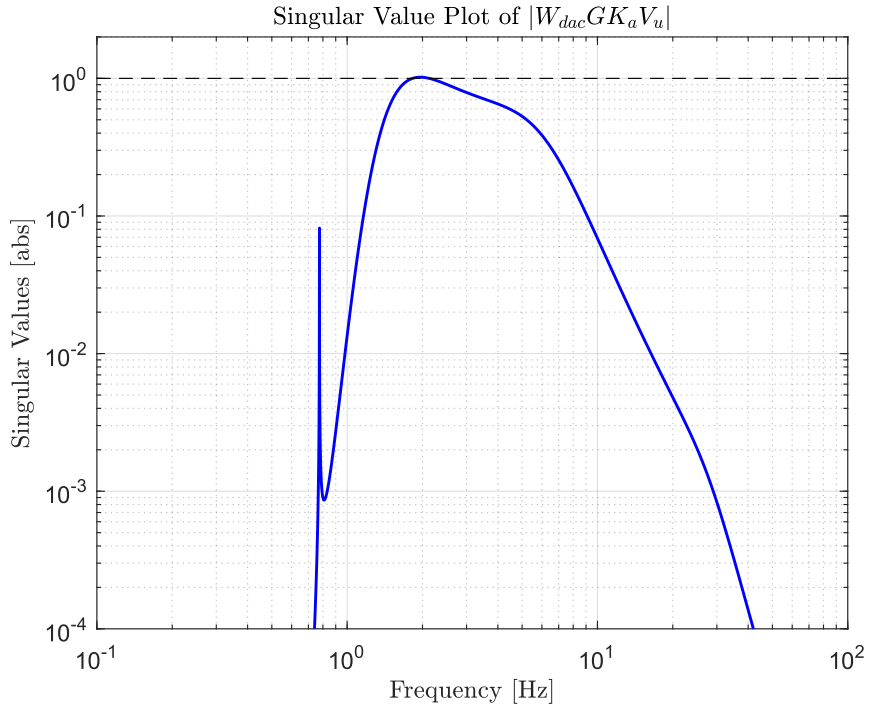

Figure 4.2: Singular values of $|W_{\mathrm{dac}}(s)G(s)K_{\mathrm{a}}V_{\mathrm{u}}|$ optimization path, confirming that $|GK_{\mathrm{a}}u_{\mathrm{d}}| < |W_{\mathrm{dac}}^{-1}|$

Next, Figure 4.3 shows the open-loop equivalent DAC noise, compared to the filter $W_{\mathrm{dac}}^{-1}(s) = W_{\mathrm{ET-LF}}(s)$. From this figure, we can see that due to the $\mathcal{H}_\infty$-bound, the open-loop DAC noise is kept below the noise

budget for almost all frequencies, except around 2Hz. This is exactly what is stated by the open-loop DAC related optimization statement. Notice that the open-loop equivalent DAC touches the inverse of the weighting filter at the peaking of the singular value plot that is shown in Figure 4.2, at a frequency of 2Hz. It should be noted that the DAC noise slightly exceeds the inverse of the weighting filter, since $\gamma_{\mathrm{d}} = 1.02$.

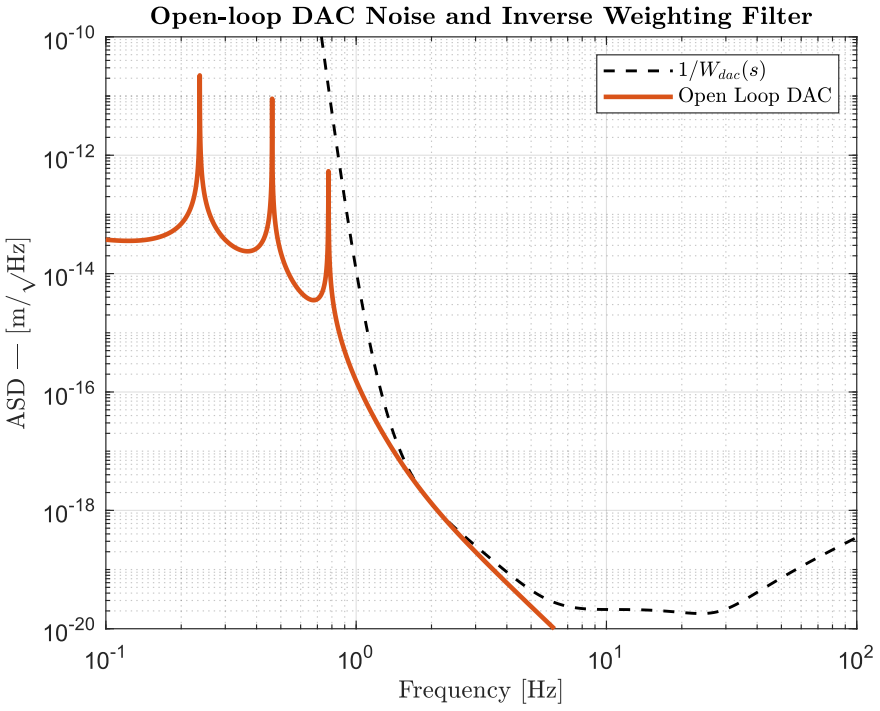

Figure 4.3: Open-loop DAC noise equivalence, compared to the ET-LF noise budget

Finally, the closed-loop stability of the control system is assessed via the Nyquist stability criterion. The number of counter clock-wise encirclements of the point $s = -1 + 0j$ equals zero, as does the number of open-loop poles in the RHP. The system is thus closed-loop stable. The robustness constraint results in that the requested modulus margin of $\mathrm{MM}_{\mathrm{req}} = 0.1$, as indicated by the green dashed circle with a radius of $\mathrm{MM} = 0.1071$, is guaranteed.

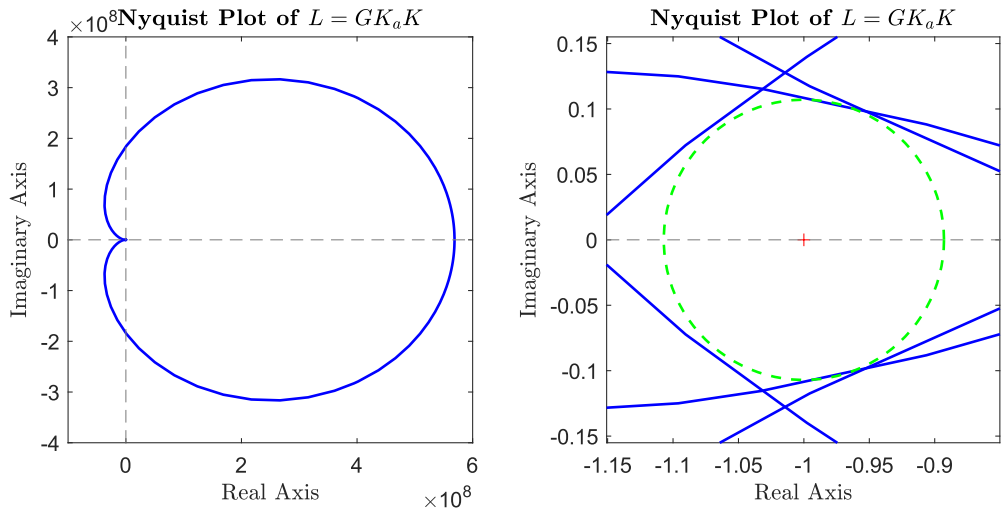

Figure 4.4: Nyquist plot of the loop gain $L(s) = G(s)K_{\mathrm{a}}K(s)$

Figure 4.5 shows the loop gain resulting from the synthesis. It is noticeable that the controller has significantly high gain for frequencies lower than $\omega_{\mathrm{c}} \approx 1$Hz. This is because high control gains are needed

at low frequencies in order to attenuate the seismic disturbance. In the frequency range of $1 - 10$Hz, the loop gain goes flat. This is due to the robustness constraint. At this frequency range, it can be noted how the controller puts in effort to keep the peaking of the sensitivity below the inverse of $W_{\text{rob}}(s)$. This is discussed in Chapter 5.

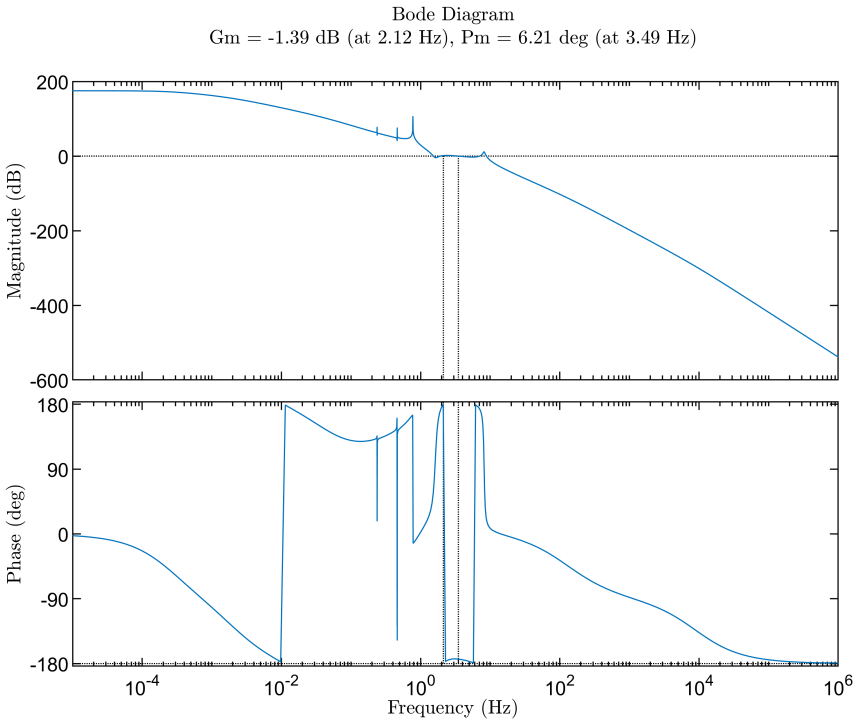

Figure 4.5: Loop gain $L(s) = G(s)K_{\text{a}}K(s)$, resulting from the synthesis

The achieved gain and phase margin are directly a result of the robustness constraint. Achieving a certain modulus margin guarantees a gain margin and phase margin as follows.

$$\text{GM} = \frac{||S(s)||_\infty}{||S(s)||_\infty - 1}[\text{abs}], \qquad \text{PM} = \frac{1}{||S(s)||_\infty}[\text{rad}] \tag{4.3}$$

With $||S(s)||_\infty = \frac{1}{\text{MM}}$. For the achieved modulus margin, this means that the minimum gain margin would be GM $= 1.12$dB and PM $= 6.14°$. Figure 4.5 confirms that this is the case. The optimized values of the actuator sizing matrix K_{a} are given in Table 4.1 below, as well as the RMS value of the control signal.

	Top Actuator	**Bottom Actuator**
$K_{\text{a,i}}G_{\text{i}}(0)$	$1.74 \cdot 10^{-7}$m/V	$3.12 \cdot 10^{-8}$m/V
u_{rms}	3.61V	0.96V

Table 4.1: Optimal actuator sizing and average control voltage for each actuator

The sizing of the actuators are expressed as the maximum achievable displacement at DC. That is then the DC gain of the plant $G(s)$ convoluted with the actuator gain matrix as K_{a}. The RMS control voltages are in the range of typical low voltage DAC's [13, 23].

The optimization algorithm appears to minimize the effects of the seismic disturbances, while satisfying the open-loop DAC noise constraint. Also, the controller keeps the sensitivity peak $|S(s)|_\infty$ below the admissible limits, such that a sufficiently large robustness margin is guaranteed. The closed-loop RMS of the seismic disturbance is however not within specifications, hence some additional effort is needed to increase the performance of the system.

For the optimization that is described above, only actuation at the two top stages is considered. Possibly, additional actuation at the mirror stage could increase the attenuation of the seismic noise. Since the last

stage does not provide much roll-off of the gain to high frequencies, it can be expected that the size of the actuator at the mirror is made rather small, to satisfy the open-loop DAC noise constraint. However, the additional actuator could increase performance by introducing more flexibility in the design of the controller and additional actuation power to the system.

4.2 Paper Non-Smooth Mixed Synthesis for Gravitational Wave Telescopes

This chapter shows a paper, that was written to show how non-smooth mixed optimization strategies can be implemented to design controllers for gravitational wave detection applications. The paper was written with the main purpose to convey the methodology as a usefull tool that can aid controller design for these applications. Especially, this is shown for control problems that involve both $\mathcal{H}_2$-optimal design that satisfy relevant $\mathcal{H}_\infty$-constraints according to requirements that are typically found for gravitational wave telescope applications. The paper is yet under review of LIGO/Virgo and will then be submitted to the Galaxies journal of MPDI.

Besides the capabilities of the optimizer, the intention is also to showcase how controller optimizations can significantly speed up the design of control systems. Moreover, the methodology is really flexible concerning changes of the control problem. Once a suitable definition of the control challenge exists, a change in noise budget, or models of the system disturbances is reflected quickly by interchanging these models within the optimization statement. A new controller is computed accordingly without much additional effort. This is especially beneficial over manually re-tuning controllers via classical methods. This also allows to quickly assess the performance of a suspension configuration, without much effort spent on manually tuning controllers. In the previous paragraph, it was seen that actuation at the two top stages is not sufficient to meet the required performance for the active suspension. Therefore, the paper shows an optimization study which investigates a suspension that is actuated at all three stages.

MDPI

Article

Non-Smooth Multi-objective Controller Synthesis for Test-Mass Actuation in Gravitational-Wave Detectors

Sander K. Sijtsma [1], Pooya Saffarieh [2,3], Nathan A. Holland [2,3], Sil T. Spanjer [1], Wouter B. J. Hakvoort [1], and Conor M. Mow-Lowry [2,3]

[1] University of Twente, Precision Engineering,7522 NB, Enschede, Netherlands
[2] Nikhef, 1098 XG Amsterdam, Netherlands
[3] Department of Physics and Astronomy, Vrije Universiteit Amsterdam, 1081 HV Amsterdam, Netherlands

Abstract: This paper proposes a non-smooth controller optimization method and shows the results of ongoing research on the implementation of this method for gravitational wave applications. Typical performance requirements concerning these type of suspensions are defined in terms of both $\mathcal{H}_2$- and $\mathcal{H}_\infty$-type constraints. A non-smooth optimization approach is investigated, which allows the use of non-convex cost functions that are often a result of mixed $\mathcal{H}_2/\mathcal{H}_\infty$ optimization problems. Besides the controller, the distribution of the actuation is integrated with the optimization to investigate the feasibility of simultaneous controller and actuator optimization. The results demonstrate that the proposed non-smooth optimization method is able to find suitable solutions for the control and actuator distribution that satisfy all required performance and design constraints.

Keywords: Non-smooth Controller Optimization, Optimal Control, Vibration Isolation, Gravitational Waves, Einstein Telescope, Payload Suspension

1. Introduction

Observations of gravitational waves made by the LIGO-Virgo-KAGRA collaboration [2–8] are the result of decades of innovation of the ground-based detectors LIGO [1], Virgo [9], and KAGRA [10]. All of these detectors employ laser-interferometry to detect gravitational waves that pass through the earth. The mirrors, or test masses, that reflect the laser at the ends of the interferometer arms are isolated from vibration by means of extensive suspension systems that include both active and passive vibration isolation strategies [13,14]. Although current and future detectors have adapted different vibration isolation techniques, each observatory's vibration isolation involves a 'payload' suspension that refers to the final stages of the vibration isolation. Actuation on the payload is the primary method for compensating residual disturbances and 'locking' the interferometer. The global feedback controllers, required to lock the optical resonators, are usually designed via classical loop-shaping methods. While these methods are effective, they tend to be challenging for less experienced control designers, and it is time-consuming to develop many such controllers during the design phase of the suspension system and payload.

More modern approaches for the design of control systems are automated controller optimization strategies, amongst which $\mathcal{H}_2$- and $\mathcal{H}_\infty$-synthesis are among the most commonly employed methods [24], and they have already been applied for gravitational-wave applications [16,25]. Typically, the computation of a suitable control algorithm that meets the control system requirements is performed by a computer program, and the responsibility of the control system designer is shifted to translating the design requirements into a relevant optimization problem. The benefit of this approach lies in the fact that once a suitable mathematical definition of the control problem exists, a change in the noise models or the observatory's requirements is reflected simply by the relevant parameters within the problem definition. The computational program produces an updated controller design without much additional effort. Compared with classical controller design methods, this

Citation: Sijtsma, S.K.; Saffarieh, P.; Holland, N.; Spanjer, S.T.; Hakvoort, W.B.J; Mow-Lowry, C.M. Title. *Journal Not Specified* **2024**, *1*, 0. https://doi.org/

Received:
Revised:
Accepted:
Published:

optimal approach can simplify and accelerate the design or redesign of suitable control algorithms. Moreover, optimization methods allow for quick performance evaluation for a wide range of suspension configurations during the conceptual design phase enabling a more holistic controls and mechanics design process. As such, optimal control methods are especially interesting for third generation gravitational-wave detectors the Einstein Telescope (ET) and Cosmic Explorer that are still in the development phase [15,17]. Specifically, the sensitivity design curve and requirements for the low-frequency optimised interferometer of the Einstein Telescope, ET-LF, are considered in this study.

This paper investigates the suitability of a non-smooth mixed synthesis optimization algorithm [11,12], which allows us to automatically tune controllers for a problem that is constrained by both $\mathcal{H}_2$ and $\mathcal{H}_\infty$ system norms. This approach was successfully applied to similar applications within the precision engineering field [23]. A simplified model of the suspension is considered to illustrate how this optimization approach fits the requirements typical for a payload suspension gravitational-wave detectors. Moreover, the optimization of the distribution of the actuator forces is considered, opening the possibility to jointly design both the controller and a parametric mechatronic design.

2. Modelling

In order to demonstrate non-smooth optimisation methods, the dynamics of the payload suspension can be represented with sufficient accuracy by a multi-pendulum system. In this study, we consider a 3-stage 3-DoF pendulum that is actuated at the mirror and both upper stages. A schematic model of the plant is shown in Figure 1. The mass of each stage is denoted as m_i, $i = 1,2,3$ and the length of each pendulum by l_i, $i = 1,2,3$. The values for masses and lengths are taken from [19].

The residual seismic disturbance at the base of the payload suspension is denoted by the signal $x_0(t)$. The state vector of the suspension is given by the angles of the pendulums as $\boldsymbol{q} = [\theta_1\ \theta_2\ \theta_3]^T$. Although the pendulum angles are used to express the equations of motion that describe the dynamics of the suspension, the measured coordinate that we are actually interested in is the displacement of the mirror. When the equations of motion are converted into state-space representation, the C-matrix converts angles into displacement such that the output of the model is $y \approx l_1\theta_1 + l_2\theta_2 + l_3\theta_3$. The aim of the suspension system is to minimize the coupling of $x_0(t)$ to the motion $x(t)$ of the mirror. The general form of the linearized dynamics of the payload suspension is given by the following equation, assuming the small angle approximation

$$M\ddot{\boldsymbol{q}} + g\boldsymbol{q} = \boldsymbol{\xi}, \tag{1}$$

where

$$M = \begin{bmatrix} (m_1+m_2+m_3)l_1^2 & (m_2+m_3)l_1l_2 & m_3l_1l_3 \\ (m_2+m_3)l_1l_2 & (m_2+m_3)l_2^2 & m_3l_2l_3 \\ m_3l_1l_3 & m_3l_2l_3 & m_3l_3^2 \end{bmatrix}, \tag{2}$$

$$g = \begin{bmatrix} (m_1+m_2+m_3)gl_1 & 0 & 0 \\ 0 & (m_2+m_3)gl_2 & 0 \\ 0 & 0 & m_3gl_3 \end{bmatrix}. \tag{3}$$

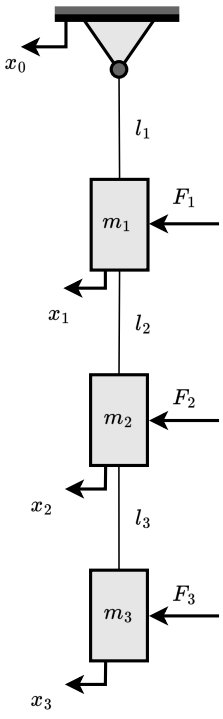

Figure 1. Schematic model of the payload suspension

Since this plant has multiple inputs and a single measured output, the system is of MISO type.

3. Problem Formulation

The motion of the mirror is interferometrically sensed by the observatory's primary laser through the 'global' interferometer sensing and control system. The main objective for the global interferometer control system is to 'lock' the interferometer by keeping it within its small linear operating range. This is necessary to achieve the extreme sensitivities that enable the detection of gravitational waves. A driving requirement of this control system is to limit the differential motion of the optical resonators within the detector arms. This motion must be reduced to less than a picometer [13]. We assume a value of $1 \cdot 10^{-13}$ m in this work. The dominant contribution to this differential motion is the residual seismic motion leaking through the active and passive isolation stages at low frequencies, typically between 0.02 Hz and 0.2 Hz.

Control of this motion is distributed over the final stages of the mirrors' suspension. This necessarily requires actuators that introduce (Digital to Analog Converter) DAC noise to the system, since the control system is implemented digitally. Since the sensitivity of a gravitational wave detector is often expressed as a combination of the open-loop equivalent contributions from several sources, the contribution of the open-loop equivalent DAC noise may not exceed the observatory's design sensitivity curve at any point over the entire sensitive frequency range. Tables of all the signals and dynamic systems that will appear in the following paragraphs are given in Appendix A.1 and A.2.

The main performance objective of the control system is to find a controller and actuator distribution that limits the closed-loop root mean square (RMS) of the mirror's residual motion. This is a typical $\mathcal{H}_2$-control problem, since an $\mathcal{H}_2$-optimal controller effectively minimizes the variance of selected closed-loop control signals. The requirement on the DAC noise is a hard limit. The open-loop equivalent spectra must not exceed the detector's sensitivity curve. This can be captured by an $\mathcal{H}_\infty$-norm on the open-loop equivalent DAC noise spectrum. Moreover, desired robustness margins typically manifest as additional $\mathcal{H}_\infty$-constraints. Figure 2 shows a block diagram of the payload suspension control system.

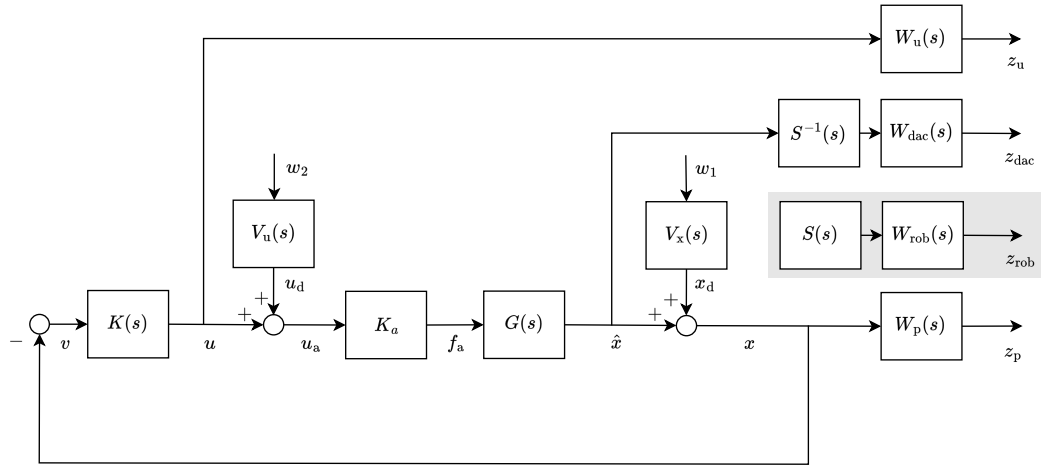

Figure 2. Block diagram of the payload suspension control system, including $\mathcal{H}_2/\mathcal{H}_\infty$-weights

The transfer function $G(s)$ is a model of the suspension that maps actuator forces to the mirror motion. The dynamics of the actuators are represented by a frequency-independent matrix K_{a} N/V such that the actuators can be simultaneously optimized together with the controller to reduce the coupling of DAC noise into the system. Choosing a flat gain to represent the actuator dynamics simplifies the optimization problem, since we are neglecting high-frequency dynamics that are not interesting for this problem. The gain represents the size of the actuator, such that the optimizer can return an optimal distribution of the actuation over the three stages of the suspension. The total transfer from input voltage u_{a} to displacement of the mirror $\hat{x}$ is then given by $G(s)K_{\mathrm{a}}$. The signal x

denotes the total mirror motion, including the residual seismic disturbance, that is present at the mirror. Channels for both relevant $\mathcal{H}_2$ and $\mathcal{H}_\infty$ constraints are also included in the block diagram.

An additional $\mathcal{H}_2$-constraint $W_{\mathrm{u}}(s)$ on the control signal u is introduced to prevent the RMS of this signal from exceeding the DAC range. The RMS requirement is captured by the weight W_{p}, which is a constant gain. The hard limit on the open-loop-equivalent DAC noise is dictated by the filter $W_{\mathrm{dac}}(s)$, which modelled as the approximate inverse of the sensitivity curve of the detector [20].

Notice that the inverse of the sensitivity function $S(s)$ is introduced to emphasize that the DAC noise optimization channel is related to an open-loop requirement. An $\mathcal{H}_2$-optimal controller often results in a closed-loop system with very small stability margins, which is often undesirable for any control system. A robustness margin can be defined as the distance between the critical point and the loop gain in the Nyquist plot. This robustness margin is guaranteed by introducing an additional $\mathcal{H}_\infty$-constraint W_{rob} that is applied to the sensitivity function to maintain a desired distance between the loop gain and the critical point on the Nyquist plot. The sensitivity is the closed-loop transfer function that maps the seismic disturbance x_{d} to the mirror motion x and is defined as

$$S(s) = (I + G(s)K_{\mathrm{a}}K(s))^{-1}. \tag{4}$$

Peaking of this sensitivity function is constrained with an $\mathcal{H}_\infty$-bound, since the robustness margin of the system is inversely proportional to the $\|S(s)\|_\infty$-norm.

4. Optimization

Consider the generalized plant formulation of Figure 3. The generalized plant $\tilde{P}(s)$ is the open-loop mapping from disturbances $\tilde{w}$, controller command u, and actuator output f_{a} to the performance outputs $\tilde{z}$, controller input v, and actuator input u_{a}. The plant $P(s)$ includes the noise models and weighting filters. The controller $K(s)$ and actuator dynamics K_{a} are taken out of the loop because both are to be optimized by the algorithm. Since the disturbances do not have a unitary white power spectrum, we need to include noise models that colour white noise to the realistic disturbance spectra [18]. The matrix $V(s)$ is a matrix with linear time-invariant noise colouring models on the diagonal. The individual entries colour white noise w such that the coloured noise $\tilde{w}$ represents the actual disturbance and $\tilde{w} = V(s)w$. The entries of $V(s)$ thus consist of the DAC noise model, $V_{\mathrm{u}}(s)$, and the seismic disturbance model, $V_{\mathrm{x}}(s)$. The model $V_{\mathrm{x}}(s)$ is derived from known seismic disturbance spectra [21], and includes the suspension dynamics, such that the seismic disturbance can be modelled as an additive noise source at the output of the plant. The matrix $W(s)$ is a diagonal matrix with designer-specified and potentially frequency-dependent weighting filters on the diagonal and combines the performance and robustness constraints.

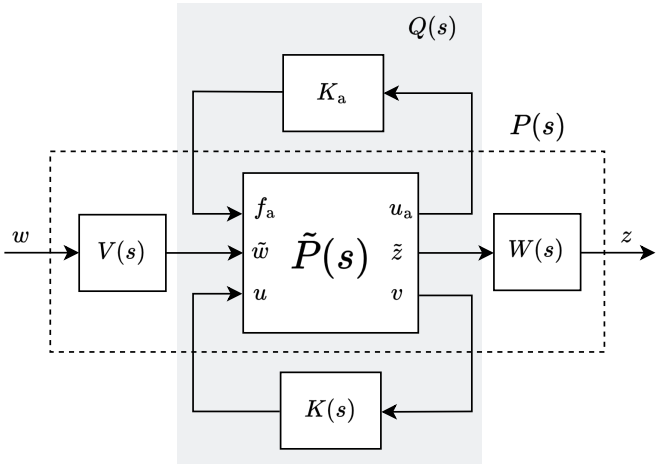

Figure 3. Generalized plant formulation of the control problem.

$$\begin{bmatrix} \boldsymbol{u}_\mathrm{a} \\ \tilde{\boldsymbol{z}} \\ \boldsymbol{v} \end{bmatrix} = \tilde{P}(s) \cdot \begin{bmatrix} \boldsymbol{f}_\mathbf{a} \\ \tilde{\boldsymbol{w}} \\ \boldsymbol{u} \end{bmatrix}, \quad \tilde{\boldsymbol{w}} = \begin{bmatrix} x_\mathrm{d} \\ u_\mathrm{d} \end{bmatrix}, \quad \tilde{\boldsymbol{z}} = \begin{bmatrix} \hat{x} \\ x \\ u \end{bmatrix}, \tag{5}$$

$$V(s) = \mathrm{diag}([\mathrm{V_x}, \mathrm{V_u}]), \qquad \mathrm{W(s)} = \mathrm{diag}([\mathrm{W_p}, \mathrm{W_{dac}}, \mathrm{W_{rob}}, \mathrm{W_u}]). \tag{6}$$

The linear fractional transformation of the plant, actuators and controller is denoted by the transfer function $Q(s)$, equivalent to the closed-loop system that maps $\tilde{\boldsymbol{w}} \rightarrow \tilde{\boldsymbol{z}}$. The optimization problem is then defined by the following statement

$$\begin{aligned} \boldsymbol{K}(\boldsymbol{s}, \boldsymbol{K_\mathbf{a}}) = \underset{K,\, K_\mathrm{a}}{\arg\min} & \left\| \begin{bmatrix} \boldsymbol{W}_\mathrm{p} & & & \\ & \mathbf{0} & & \\ & & \mathbf{0} & \\ & & & \mathbf{0} \end{bmatrix} \boldsymbol{Q}(s) \begin{bmatrix} \boldsymbol{V}_\mathrm{x} & \\ & \mathbf{0} \end{bmatrix} \right\|_2, \\ \text{s.t.} & \left\| \begin{bmatrix} \mathbf{0} & & & \\ & \boldsymbol{W}_\mathrm{dac} & & \\ & & \mathbf{0} & \\ & & & \mathbf{0} \end{bmatrix} \boldsymbol{Q}(s) \begin{bmatrix} \mathbf{0} & \\ & \boldsymbol{V}_\mathrm{u} \end{bmatrix} \right\|_\infty < \gamma_\mathrm{d}, \\ & \left\| \begin{bmatrix} \mathbf{0} & & & \\ & \mathbf{0} & & \\ & & \boldsymbol{W}_\mathrm{rob} & \\ & & & \mathbf{0} \end{bmatrix} \boldsymbol{Q}(s) \begin{bmatrix} \mathbf{1} & \\ & \mathbf{0} \end{bmatrix} \right\|_\infty < \gamma_\mathrm{r}, \\ & \left\| \begin{bmatrix} \mathbf{0} & & & \\ & \mathbf{0} & & \\ & & \mathbf{0} & \\ & & & \boldsymbol{W}_\mathrm{u,i} \end{bmatrix} \boldsymbol{Q}(s) \begin{bmatrix} \boldsymbol{V}_\mathbf{x} & \\ & \boldsymbol{V}_\mathrm{u} \end{bmatrix} \right\|_2 \leq \gamma_\mathrm{i} \quad \forall\, i, \\ & K_\mathrm{lower,j} \leq K_\mathrm{a,j} \leq K_\mathrm{upper,j} \quad \forall\, j. \end{aligned} \tag{7}$$

where the actuator gains can be tuned by the optimizer, bounded by lower limit K_lower and upper limit K_upper. The first $\mathcal{H}_\infty$-constraint is a limit on the open-loop equivalent spectrum of the DAC noise. The second $\mathcal{H}_\infty$-constraint determines the robustness, and the last $\mathcal{H}_2$-constraint ensures that each of the the actuator outputs remain with the DAC range. Typically, the cost function that is associated with such a mixed $\mathcal{H}_2/\mathcal{H}_\infty$ optimization problem is no longer convex. Although there exist methods to convexify this optimization problem [22], these can lead to conservative controller design, hence a non-smooth optimization algorithm [11,12] is utilized to solve for a controller $K(s)$ as well as the optimal actuator distribution K_a. This optimization algorithm is implemented in `Matlab's systune()` function of the `Control System Toolbox`.

5. Results

The results of a controller optimization for the suspension model that was described in Section 2 are expressed in the open-loop DAC noise equivalence requirement and the suppression of the seismic disturbance. Figure 4 shows the cumulative x_rms of the open-loop motion, of which the lowest-frequency value corresponds to x_rms. The cumulative RMS value is computed by integrating the spectra from high to low frequencies. The approximate model x_d is included. This simplified model is matched in RMS with the actual disturbance seen by the main observatory laser, x_m. The value of x_rms is reduced to a value of $4.78 \cdot 10^{-14}$ m, such that the seismic disturbance suppression requirement is satisfied.

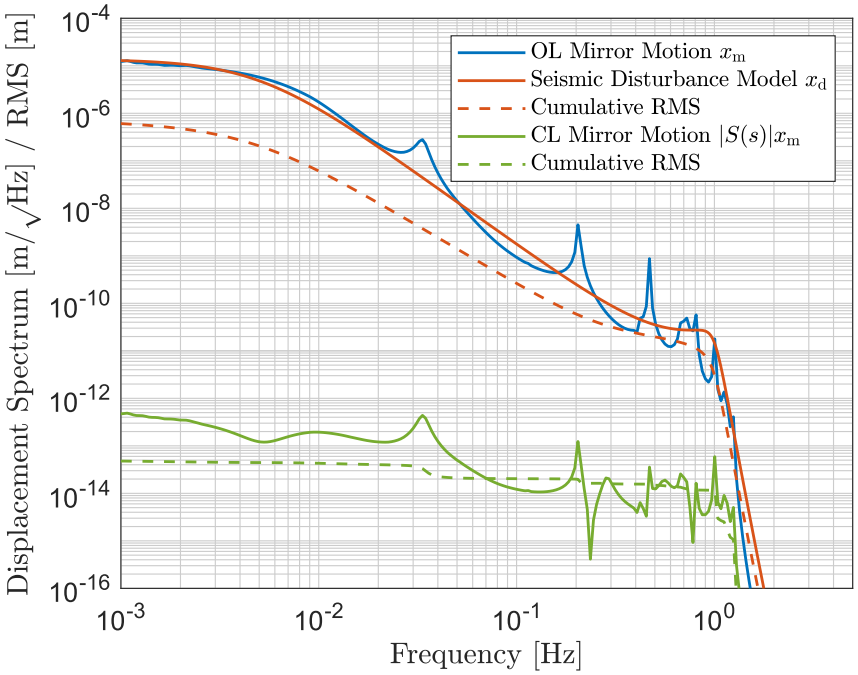

Figure 4. Closed-loop seismic disturbance compared with the open-loop. The simplified model V_x is used in the optimiser but performance is computed using the detailed disturbance.

Figure 5 shows the open-loop equivalent DAC noise and the inverse of the weighting filter, $W_{\text{dac}}^{-1}(s)$. The requirement includes a safety factor of 6 to keep the open-loop DAC noise well below the ET-LF sensitivity design curve. It can be seen that the open-loop DAC noise is tuned such that it touches the inverse of the weighting filter at around 2-5 Hz, with $\gamma_d = 1.00$, which is something that one can typically expect from an $\mathcal{H}_\infty$-optimal controller since the objective according to Equation 7 is to minimize the $\mathcal{H}_2$-channel, as long as the $\mathcal{H}_\infty$-limits allow this.

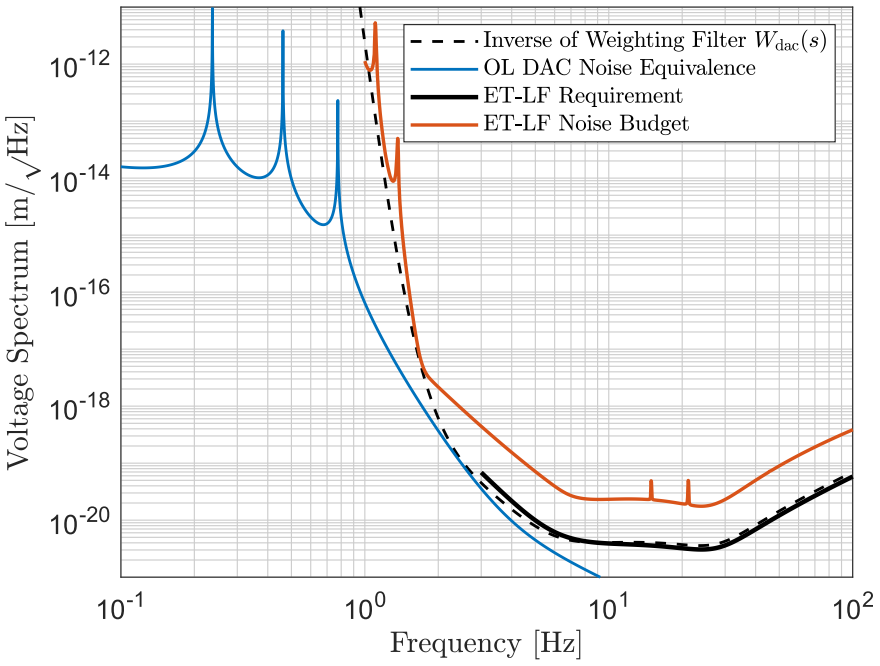

Figure 5. Closed-loop seismic disturbance suppression, compared to open-loop seismic disturbance

Additionally, the robustness constraint allows to obtain a desired modulus margin to guarantee sufficient margin against process variations. Usually, the dynamics of the suspension are well known for gravitational wave applications and the operating conditions are assumed to be rather constant. Therefore, it is not required to achieve large stability margins. The stability of the system is assessed via Nyquist stability requirement and the corresponding Nyquist diagram for the loop gain $L(s) = G(s)K_{\mathrm{a}}K(s)$ is shown in Figure 6.

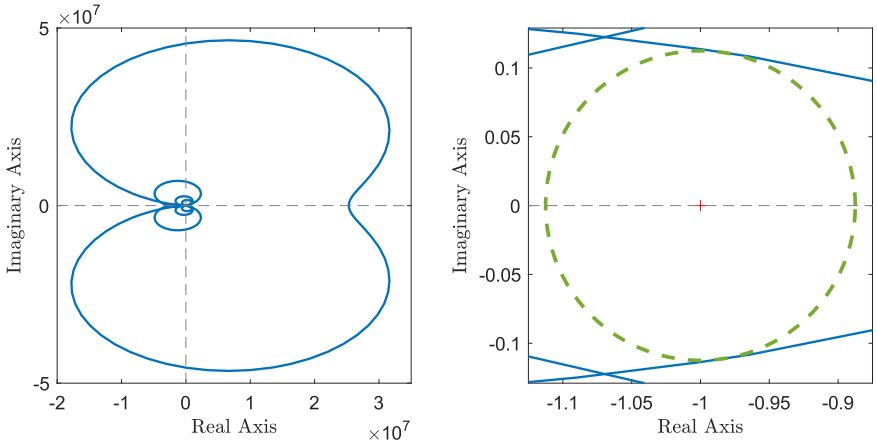

Figure 6. Nyquist plot of the loop gain $L(s)$ (left) and zoomed view around the critical point (right)

From the Nyquist plot, it can be concluded that the closed-loop system $Q(s)$ is stable and a requested modulus margin of 0.1 is guaranteed, which can be deduced from the green circle that indicates the area for which the distance to the critical point is less than 0.10. From this plot, it can be seen that the sensitivity $S(s)$ is tuned such that this closed-loop transfer function coincides exactly with $W_{\mathrm{rob}}(s)$ at multiple instances, reflected by a value of $\gamma_{\mathrm{r}} = 0.89$. Since the sensitivity touches the inverse robustness weighting filter at about $2 - 8$ Hz, the suppression of the low frequency seismic disturbance should be minimally affected by increased robustness margins.

6. Discussion

This study demonstrates a method for situating the control requirements, typical for a gravitational-wave observatory's test-mass suspension, within a non-convex, mixed optimization problem. The result of this study demonstrates that this methodology produces a quantitative global control distribution that satisfies the basic control requirements of the test-mass suspensions. Additionally, the optimizer allows to define open-loop weighting channels. For nominal $\mathcal{H}_2$ or $\mathcal{H}_\infty$ synthesis, it is often not possible to directly define such an open-loop requirement.

The controller is able to suppress the seismic noise sufficiently, such that the detectors' sensitivity is not degraded by the expense of excessive effects of the seismic noise at the mirror stage. From the open-loop DAC plot from Figure 5, it can be seen that the graph closely meets the inverse of the weighting filter, which means that the controller is optimized such that the seismic motion is suppressed until the open-loop DAC noise injection limit is reached. Additionally, the weighting on the controller commands allows to ensure that the signal u stays below the capacity of the actuators and drives. Finally, the Nyquist plot shows how an additional $\mathcal{H}_\infty$ robustness constraint allows to enforce a desired robustness margin such that the system is sufficiently far away from instability to account for process variations, such as process delays, which are inherently present to some extent in any control system.

A great benefit of optimization based control system design is that it alleviates the need for manual tuning of filters, allowing the global interferometric control distribution to be verified early in the design phase. Moreover, automated optimal control techniques allow to effectively assess many possible suspension configurations within the design

space. It is often not possible to achieve this utilizing manual control design techniques and thus poses a great benefit in terms of allowable exploration of a more effective suspension design.

This specific case study involves for a simultaneously optimized actuator distribution for the suspension stages, however there are many more possibilities to study. The optimizer allows to explicitly tune parameterized models of dynamic systems, which allows for a simultaneous controller and suspension mechanics optimization. Since most of the time, extensive suspension models are present, this method lends itself well to integrate a suspension parameter optimization to fully benefit from the optimization strategy. This way, even better performance of the system may be achieved by having the optimizer aiding as a design tool for both controller algorithms and plant dynamics.

Finally, the controller that is tuned for this case study is a single transfer function matrix with three entries. Additionally, possible benefits of a multi degree-of-freedom controller may be studied, or the implementation of a feed-forward compensator might be of interest to include to further increase the performance of the system. All of these suggestions could be seamlessly integrated with the optimization study that was shown previously.

7. Conclusions

We showed that the combination of seismic disturbance variance minimization and frequency-dependent bounded requirements regarding the DAC noise can be condensed in a mixed $\mathcal{H}_2/\mathcal{H}_\infty$-optimization problem. Additional constraints, such as robustness and control signal variance constraints, can be integrated seamlessly with the optimization. Non-smooth synthesis was utilized to avoid conservative controller design. This method also explicitly allows for optimizing the actuation distribution and, moreover, lends itself well to include optimization of the mechanics or an additional feed-forward controller.

Acknowledgments: The authors thank M. Valentini for useful discussions and input. This project has received funding from the European Research Council (ERC) under the European Union's Horizon 2020 research and innovation programme (grant agreement No. 865816).

Abbreviations

The following abbreviations are used in this manuscript:

ET	Einstein Telescope
ET-LF	Einstein Telescope's Low-Frequency interferometer
DoF	Degree of Freedom
MISO	Multiple Input Single Output system
DAC	Digital to Analog Converter
RMS	Root Mean Square

Appendix A

Appendix A.1

Table A1 shows all control signals that appear in the figures and equations throughout this text. The following control signals can be identified. The argument (s) is omitted for readability.

Table A1. Summary of the control signals, identified in the optimization problem.

Signal	Meaning	Unit
f_{a}	Actuator effort	[N]
u	Controller command voltage	[V]
u_{a}	Actuator voltage, sum of u and DAC noise	[V]
u_{d}	DAC noise	[V]
v	Controller input	[m]
w_1	White noise, coloured by V_{u}	[-]
w_2	White noise, coloured by V_{x}	[-]
w_{rob}	Robustness constraint input, $w_{\mathrm{rob}} = x_{\mathrm{d}}$	[m]
x	Total mirror motion	[m]
x_{d}	Seismic disturbance felt at the mirror stage	[m]
x_{m}	Real disturbance felt at the mirror stage	[m]
$\hat{x}$	Output of the suspension model	[m]
z_{dac}	Open-loop DAC noise channel, $\mathcal{H}_\infty$-bounded	[-]
z_{p}	Seismic disturbance suppression channel, $\mathcal{H}_2$-bounded	[-]
z_{rob}	Robustness channel, $\mathcal{H}_\infty$-bounded	[-]
z_{u}	Controller energy channel, $\mathcal{H}_2$-bounded	[-]

Appendix A.2

Table A5 shows all control signals that appear in the figures and equations throughout this text. The following control signals can be identified. The argument (s) is omitted for readability.

Table A3. Summary of the systems and models, identified in the optimization problem

Model	Meaning	Unit
G	Actuator effort	[m/N]
K	Controller	[N/m]
K_{a}	Actuator dynamics	[N/V]
P	Generalized plant	[-]
$\tilde{P}$	Generalized plant without weights and noise models	[-]
Q	Linear fractional transformation of P, K and K_a	[-]
S	Sensitivity transfer function	[-]
V	Matrix with noise models on the diagonal	[-]
V_{x}	Seismic disturbance model	[m]
V_{u}	DAC noise model	[V]
W	Matrix with weighting filters on the diagonal	[-]
W_{dac}	$\mathcal{H}_\infty$-weight open-loop DAC noise	[-]
W_{p}	$\mathcal{H}_2$-weight seismic disturbance	[-]
W_{rob}	$\mathcal{H}_\infty$-weight, robustness filter	[-]
W_{u}	$\mathcal{H}_2$-weight controller command	[-]

Appendix A.3

The open-loop gain $L(s)$ resulting from the optimization is shown in Figure A1. The gain and phase margin can be computed as:

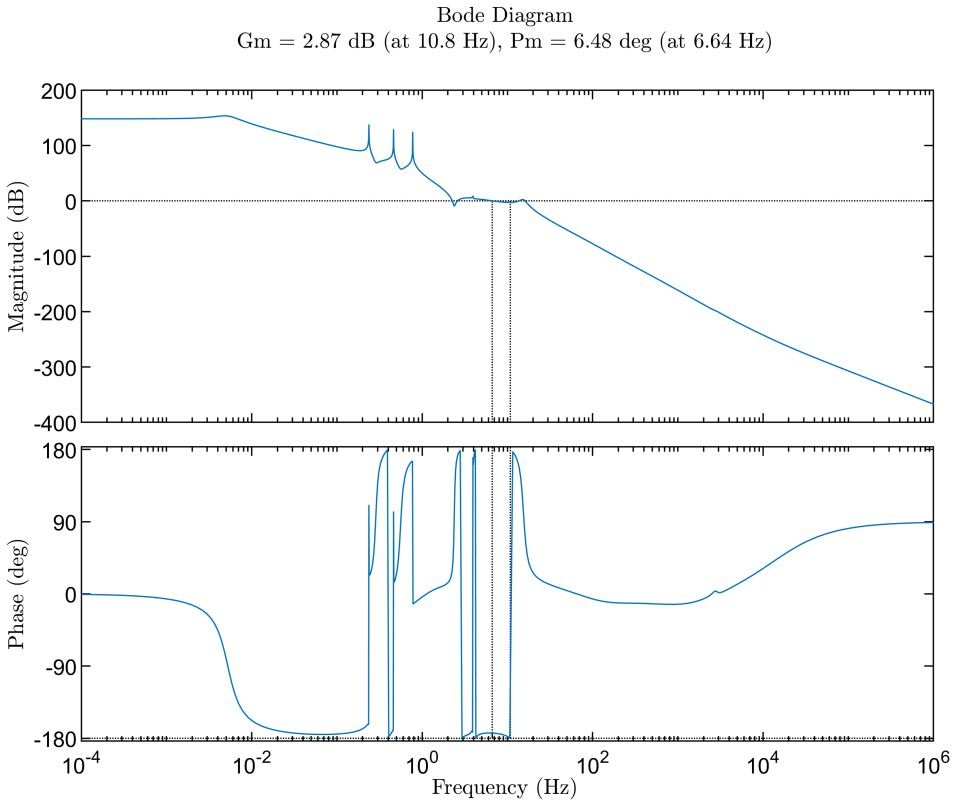

Figure A1. Bode plot of the loop gain $L(s) = G(s)K_{\mathrm{a}}K(s)$

The sizing of the actuators is expressed in terms of achievable displacement in meters per volt for each actuator. The sizing is then computed as $K_{\mathrm{a}}G(0)$. The values that resulting from the optimization study are summarized in Table A5 below, as well as the RMS of the control commands for each channel.

Table A5. Sizing of the actuators, resulting from the optimization study

	Top actuator	**Middle Actuator**	**Bottom Actuator**
K_{a}	$7.5 \cdot 10^{-8}$[m/V]	$3.7 \cdot 10^{-9}$[m/V]	$3.2 \cdot 10^{-11}$[m/V]
u_{rms}	7.9V	0.4V	2.6V

References

1. Aasi, J. et al.,Advanced Ligo. Class. Quantum Grav.**2015**;32;
2. Abbot,B.P. et al., Observation of Gravitational Waves from a Binary Black Hole Merger. Phys. Rev. Lett. .**2016**;116;
3. Abbot,B.P. et al., Multi-messenger Observations of a Binary Neutron Star Merger. The Astrophysical Journal Letters.**2017**;848;
4. Abbot,B.P. et al., Observation of Gravitational Waves from a Binary Neutron Star Inspiral. Phys. Rev. Lett. .**2017**;119;
5. Abbot,R. et al., Compact Binary Coalescences Observed by LIGO and Virgo during the Second Part of the Third Observing Run. Phys. Rev. X.**2023**;13;041039
6. Abbot,R. et al., Compact Binary Coalescences Observed by LIGO and Virgo during the First Half of the Third Observing Run. Phys. Rev. X.**2021**;11;
7. Abbot,R. et al., A Gravitational-Wave Transient Catalog of Compact Binary Mergers Observed by LIGO and Virgo during the First and Second Observing Runs. Phys. Rev. X.**2019**;9;
8. Abbot,R. et al., Deep extended catalog of compact binary coalescences observed by LIGO and Virgo during the first half of the third observing run. Phys. Rev. D.**2024**;109;

9. Agathos, M. et al.,Advanced Virgo: a second-generation interferometric gravitational wave detector. Class. Quantum Grav.**2015**;32;24001-24052;
10. Akutsu, T. et al., Construction of KAGRA: an Underground Gravitational Wave Observatory. Progress of Theoretical and Experimental Physics. **2018**
11. Apkarian P., Noll D. and Rondepierre A., Mixed $\mathcal{H}_2/\mathcal{H}_\infty$ Control Via Nonsmooth Optimization. **2009**
12. Apkarian P., Noll D. and Pellanda, P., Non-smooth $\mathcal{H}_\infty$ Synthesis. IEEE Transactions on Automatic Control. **2006**;51;71-86;
13. Aston, M. et al., Update on quadruple suspension design for Advanced LIGO. Class. Quantum Grav. **2012**;29;235004;
14. Bertocco, A. et al., New Generation of Superattenuator for Einstein Telescope: preliminary studies. Class. Quantum Grav. **2024**; 51;
15. Chamberlain, K and Junes, N., Theoretical physics implications of gravitational wave observation with future detectors. Phys. Rev. D. **2017**;96;
16. Dael, M. van et al., Control of the laser frequency in the Virgo interferometer: Dynamic noise budgeting for controller optimization. Astroparticle Physics. **2025**;164;
17. Einstein Telescope Steering Committee, Design Report Update 2020: for the Einstein Telescope. Einstein Telescope Collaboration. **2020**;ET-0007C-20.
18. Jabben, L., Mechatronic Design of a Magnetically Suspended Rotating Platform. PhD Thesis. Delft University of Technology.**2007**
19. Koroveshi, X et. al.,Cryogenic payloads for the Einstein Telescope: Baseline design with heat extraction, suspension thermal noise modeling, and sensitivity analyses.Phys. Rev. D**2023**;108;
20. Moore, C. and Cole, R., Gravitational Wave Sensitivity Curves. Class. Quantum Grav. **2015**.
21. Mow-Lowry, C. and Martynov D., A 6D interferometric inertial isolation system. Class. Quantum Grav. **2019**;36;
22. Scherer, C., Mixed $\mathcal{H}_2/\mathcal{H}_\infty$ Control. Springer London. **1995**
23. Spanjer, S. and Köroğlu, H. and Hakvoort, W., The Potential of Active Vibration Isolation Systems. ASPE. **2023**;81; 11-16
24. Skogestad, S. and Postlethwaite, I., *Multivariable Feedback Control*, 2nd ed.; John Wiley & Sons, Ltd.: England. **2006**; 352-362.
25. Tsang, T. et al., Optimal sensor fusion method for active vibration isolation systems in ground-based gravitational-wave detectors.Class. Quantum Grav. **2022**;39;

4.3 Extensions of the Optimization

Previously, we have seen how the non-smooth mixed synthesis optimization approach nicely complies with the mixed $\mathcal{H}_2/\mathcal{H}_\infty$-control problem for the test-mass suspension and is able to suffice all the baseline requirements for the control system. So far, only the dynamics of the actuators are considered to be optimized, simultaneously with the controller. However, the optimization algorithm also lends very well to optimize more complex dynamic systems.

Since the suspension design for ET is still in the design phase, the design is not yet set in stone. It might therefore be interesting to investigate the optimality of the suspension design as well, by exploring the design space of the mechanical system too. The next paragraphs showcase two case studies that perform a simultaneous controller and parameterized plant optimization, to investigate the possibilities to join mechatronics and controller design. Specifically, we focus on the case where there is no actuation at the mirror stage, to find out whether tuning the suspension dynamics allows to get the system performance withing specifications.

4.3.1 Optimization of Controller and Plant

The first extension of the baseline type of optimization that was shown in Section 4.1 and 4.2 investigates an optimization of a fully tunable suspension. The optimizer is free to tune the lengths and masses of the pendulum, within reasonable bounds. To facilitate this, the plant is parameterized in terms of the masses of the stages and the lengths of the pendulums. The tunable mass of each stage is denoted by m_i and the tunable length is denoted as l_i. More compactly, the set of tunable parameters is written as $\psi_\mathrm{i} = [m_\mathrm{i}, l\mathrm{i}],\ \ i = 1, 2, ..., n_\mathrm{dof}$, where n_dof is the number of generalized coordinates of the suspension. Since the triple pendulum has three degrees of freedom, we have $n_\mathrm{dof} = 3$. The transfer function of the tunable suspension is then given by:

$$G(s, \boldsymbol{\psi}), \qquad \boldsymbol{\psi} = [\psi_1 \ \ \psi_2 \ \ \psi_3]^T \tag{4.4}$$

Each tunable element of the plant is bounded by the lower bound $\psi_\mathrm{i,l}$ and upper bound $\psi_\mathrm{i,u}$:

$$\psi_\mathrm{i,l} \leq \psi_\mathrm{i} \leq \psi_\mathrm{i,u} \tag{4.5}$$

This tunable suspension can be optimized together with the actuator distribution and controller design. The lower and upper bound for the masses are $[0.25, 1.1]$, expressed as a fraction of the nominal value. The upper bound is quite low, since much higher masses are not compatible with the fused silica wires that suspend the stages. The length is bounded similarly with lower and upper bound $[0.5, 1.25]$. Again, the maximum length is constrained more, due to possibly limited allowable height of the suspension chain. The extended optimization problem, including the optimization of the plant is then stated as:

$$\boldsymbol{\Theta} = \underset{\text{K stabilizing}}{\arg\min} \ \|W_\mathrm{p}(s) F_\mathrm{l}(s, \boldsymbol{\psi}) V(s)\|_2 \qquad s.t. \tag{4.6}$$

$$\|W_\mathrm{u}(s) F_\mathrm{l}(s, \boldsymbol{\psi}) V(s)\|_2 \ \leq \gamma_\mathrm{u} \qquad \|W_\mathrm{rob}(s) S(s, \boldsymbol{\psi}) I\|_\infty \leq \gamma_\mathrm{r} \qquad \|W_\mathrm{dac}(s) G(s, \boldsymbol{\psi}) K_\mathrm{a} V_\mathrm{u}(s)\|_\infty \leq \gamma_\mathrm{d}$$

$$\psi_\mathrm{i,l} \leq \psi_\mathrm{i} \leq \psi_\mathrm{i,u}, \quad \forall\, i$$

$$K_{a_\mathrm{j,l}} \leq K_\mathrm{a} \leq K_{a_\mathrm{j,u}}, \quad \forall\, j$$

Where j now denotes the actuators, with $j = 1, 2$ since there are two actuators. Strictly speaking, the seismic noise model should have been parameterized, since it depends on the dynamics of the payload suspension as well. The actual seismic disturbance was derived from numerical transfer functions, from which it is not exactly clear which poles and zeros are attributed to the payload suspension. For the sake of completeness, the model $V_\mathrm{x}(s)$ should however be parameterized according to Equation 4.4.

Results from the Optimization

The main motivation for the optimization of the suspension is to improve the performance in terms of vibration isolation compared to the results obtained with a fixed suspension from Section 4.1. The optimization was done for a 3 DoF pendulum actuated at the two upper stages[1]. This is motivated by the

[1] The unforced dynamics of the pendulum are the same. However $F_3 = 0$, hence the generalized force ξ_3 disappears.

extra roll-off present due to the extra un-actuated stage, such that the open-loop DAC equivalent noise rolls off faster. The RMS of the closed-loop seismic noise could be reduced to about $4.56 \cdot 10^{-13}$m, without a mechanical optimization. This value does not meet the requirement on the seismic noise suppression yet. Figure 4.6 shows the CAS of the closed-loop seismic noise for the optimization that includes a tunable suspension. From this figure, we can seen that the requirement of the closed-loop RMS of the seismic noise is just met. The tuned suspension, combined with the optimal controller is able to improve the suppression of the seismic noise in terms of the RMS value by a factor of 5.

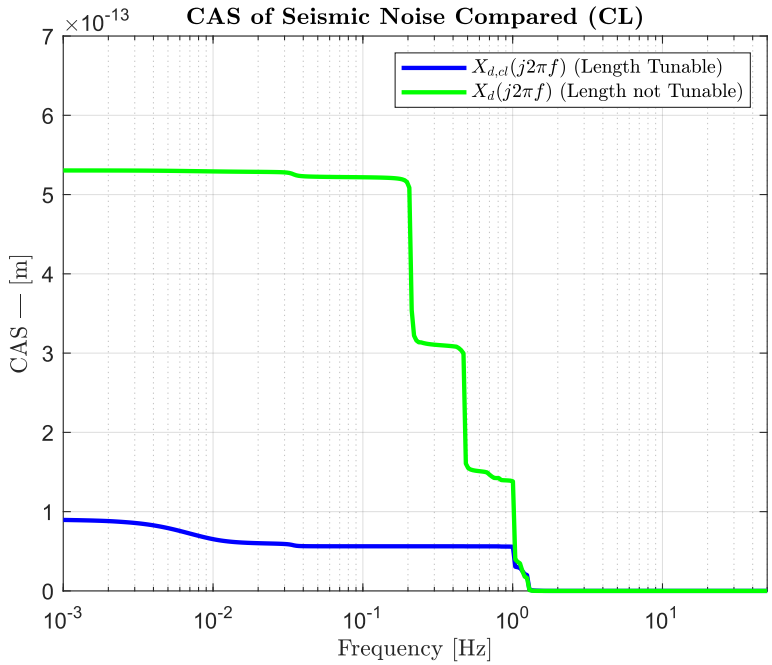

Figure 4.6: Closed-loop RMS of the seismic noise compared, tunable and non-tunable suspension

The singular value plot in Figure 4.7 shows the singular values for the optimization path $|W_{\mathrm{dac}}\hat{G}K_{\mathrm{a}}V_{\mathrm{u}}|_\infty$. From this figure, we can also see that the γ_{d} value is below one, over the entire frequency range.

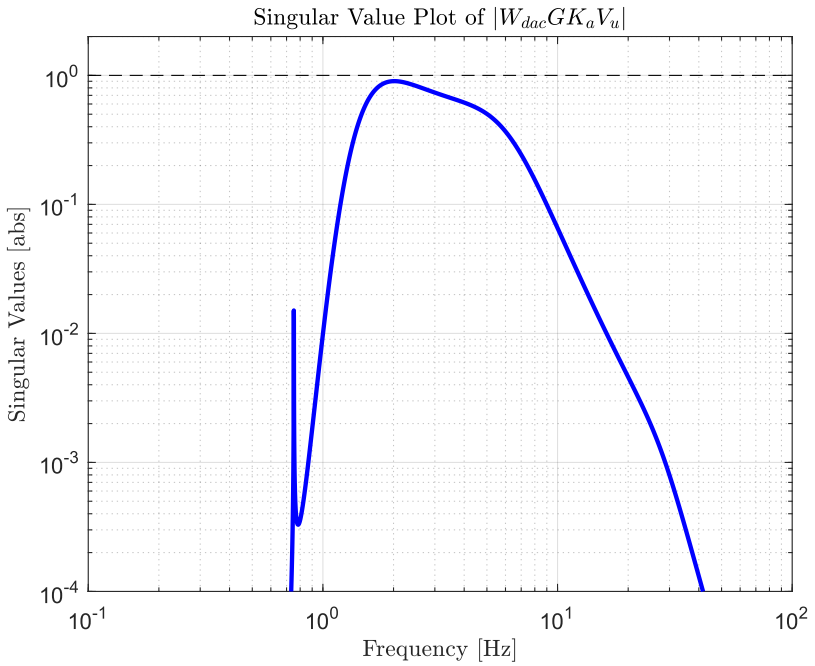

Figure 4.7: Singular values of the $|W_{\mathrm{dac}}\hat{G}K_{\mathrm{a}}V_{\mathrm{u}}|_\infty$ optimization path, confirming that $|GK_{\mathrm{a}}u_{\mathrm{d}}| < |W_{\mathrm{dac}}^{-1}|$

The open-loop DAC noise equivalence is shown in Figure 4.8. It can be seen that the optimizer tuned the system such that the DAC noise (almost) touches the inverse of the weighting filter, which is something that we expect from the optimizer.

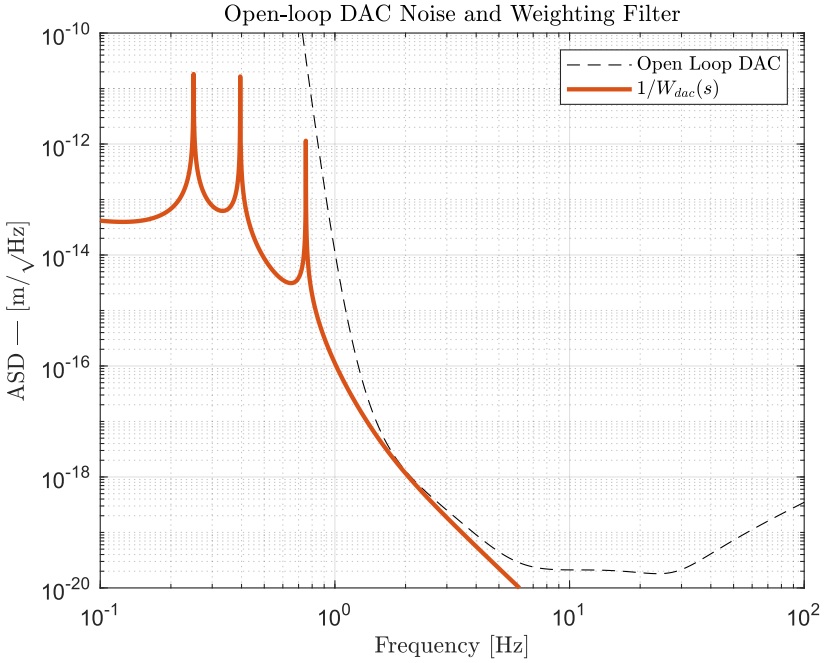

Figure 4.8: Open-loop DAC noise equivalence and inverse of the W_{dac} filter

The stability of the closed-loop system, with the synthesized controller and tuned suspension, is evaluated in the Nyquist plot in Figure 4.9. From this figure, we can see that the $\mathcal{H}_\infty$-constraint regarding the modulus margin of $\text{MM}_{\text{req}} = 0.1$ is indeed met, which corresponds with a value of $\gamma_{\text{r}} = 0.93$.

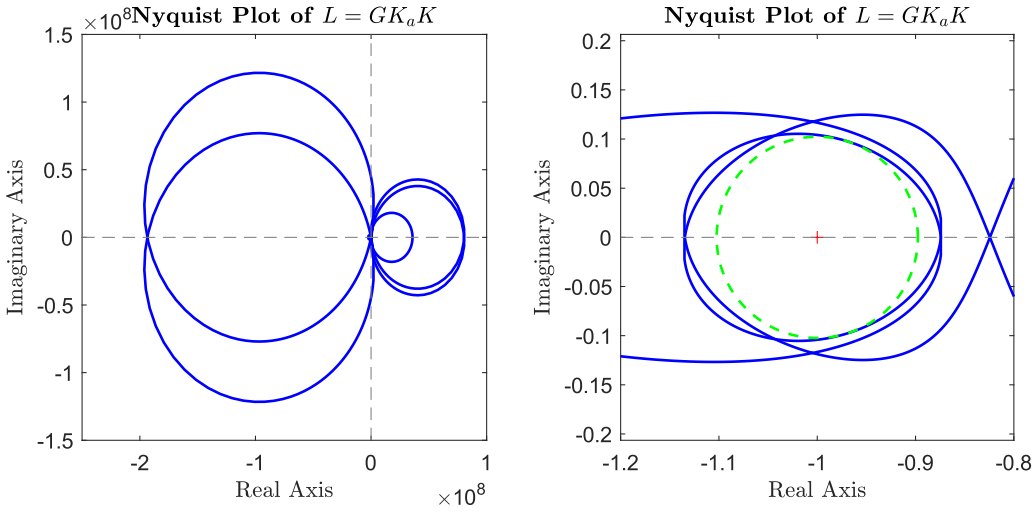

Figure 4.9: Nyquist plot for loop gain $G(s, \boldsymbol{\psi})K_aK(s)$

The optimal plant realization $G(s, \boldsymbol{\psi_{opt}})$ is shown in Figure 4.10. The overall low frequency gain is made a bit higher and the two higher frequency resonances are shifted to lower frequencies.

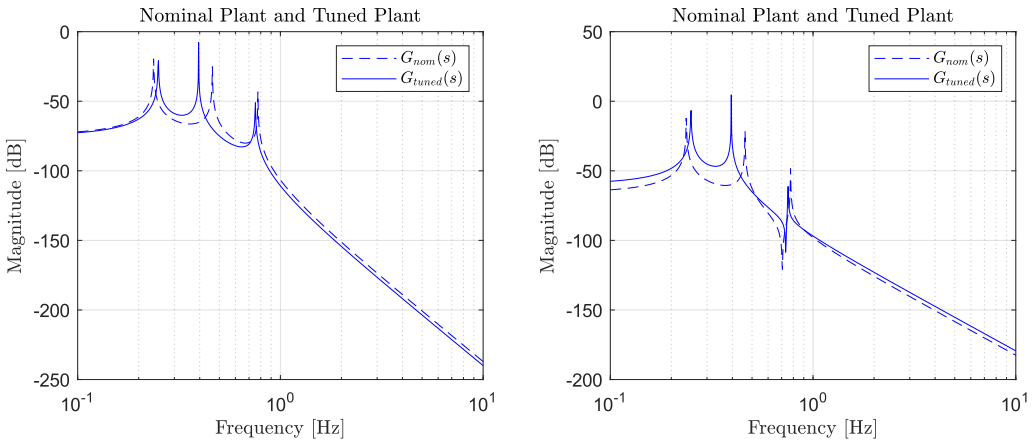

Figure 4.10: Optimal plant $G(s, \boldsymbol{\psi_{opt}})$, $G_1(s, \boldsymbol{\psi_{opt}})$ (left) and $G_2(s, \boldsymbol{\psi_{opt}})$ (right)

4.3.2 Optimization of Controller and Length Topology

The previous paragraph considers a full optimization of the plant. It is however arguable that there is a limited amount of space that can be allocated to the suspension. Therefore, a similar optimization was carried out, where the length of the pendulum can be optimized, with the additional constraint that the total length of the pendulum is not allowed to change. The optimizer is thus free to place the stages of the suspension over the total available height of the payload suspension. The set of tunable parameters consists of the three lengths of the pendulums, such that $\psi_\mathrm{i} = l_\mathrm{i}, \quad i = 1, 2, ..., n_\mathrm{dof}$. The transfer function of the tunable suspension is then given by:

$$G(s, \boldsymbol{\psi}), \qquad \boldsymbol{\psi} = [l_1 \;\; l_2 \;\; l_3]^T \tag{4.7}$$

Since the total length of the suspension should remain constant, an additional constraint is introduced, which is taken into account by the optimizer:

$$\sum_{\mathrm{i}=1}^{3} l_\mathrm{i} = const. \tag{4.8}$$

The definition of the optimization problem is then given by:

$$\boldsymbol{\Theta} = \underset{\text{K stabilizing}}{\arg\min} \; \|W_\mathrm{p}(s) F_\mathrm{l}(s, \boldsymbol{\psi}) V(s)\|_2 \qquad s.t. \tag{4.9}$$

$$\|W_\mathrm{u}(s) F_\mathrm{l}(s, \boldsymbol{\psi}) V(s)\|_2 \; \leq \gamma_\mathrm{u} \qquad \|W_\mathrm{rob}(s) S(s, \boldsymbol{\psi}) I\|_\infty \leq \gamma_\mathrm{r} \qquad \|W_\mathrm{dac}(s) G(s, \boldsymbol{\psi}) K_\mathrm{a} V_\mathrm{u}(s)\|_\infty \leq \gamma_\mathrm{d}$$

$$\psi_{\mathrm{i,l}} \leq \psi_\mathrm{i} \leq \psi_{\mathrm{i,u}}, \quad \forall \, i$$

$$\sum_{\mathrm{i}=1}^{3} \psi_\mathrm{i} = const.$$

$$K_{a_{\mathrm{j,l}}} \leq K_\mathrm{a} \leq K_{a_{\mathrm{j,u}}}, \quad \forall \, j$$

4.3.3 Results from the Optimization

The performance of the tuned controller and suspension is expressed in the seismic disturbance attenuation in terms of the RMS of the residual seismic noise. Besides the open-loop equivalent DAC noise and the Nyquist diagram, it is now also interesting to see how the optimizer distributes the stages of the pendulum over the available space. Figure 4.11 shows the CAS of the residual attenuated seismic noise. Since only the top two stages are actuated, the benefit in terms of performance gain with the optimal topology is best compared to those results that are presented in Figure 4.1.

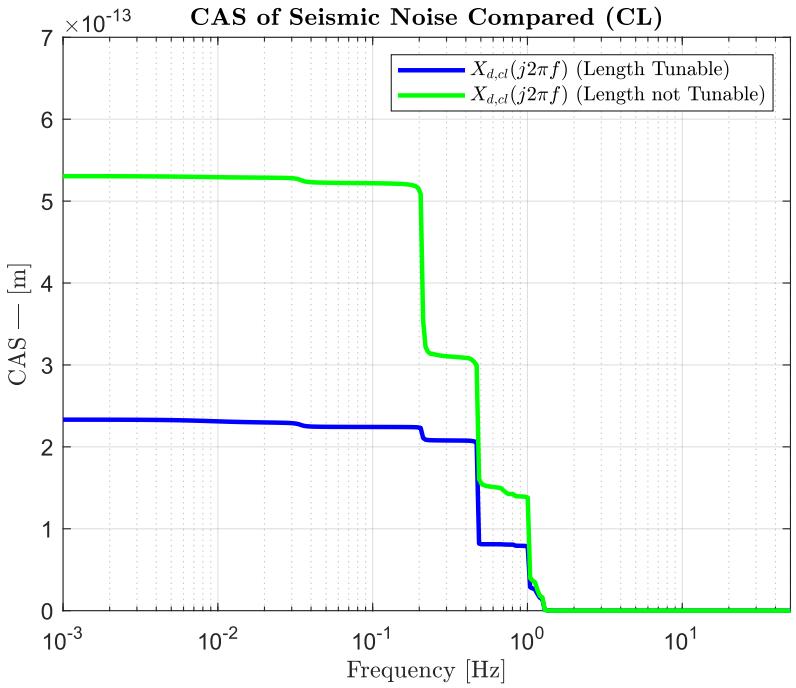

Figure 4.11: Closed-loop CAS of the seismic noise compared, tunable and non-tunable suspension

From the figure above, it can be concluded that the attenuation of the seismic noise is improved by a factor of 2. This is however not enough to comply with the requirement regarding the seismic disturbance rejection. Figure 4.12 shows the singular values of the weighted open-loop DAC, resulting from the optimization with tunable length topology. From this figure, we can see that the singular values of the open-loop DAC optimization channel again come very close to unity with $\gamma_{\mathrm{d}} = 0.9$ at about 2Hz, which is consistent with the previous results of the optimization studies.

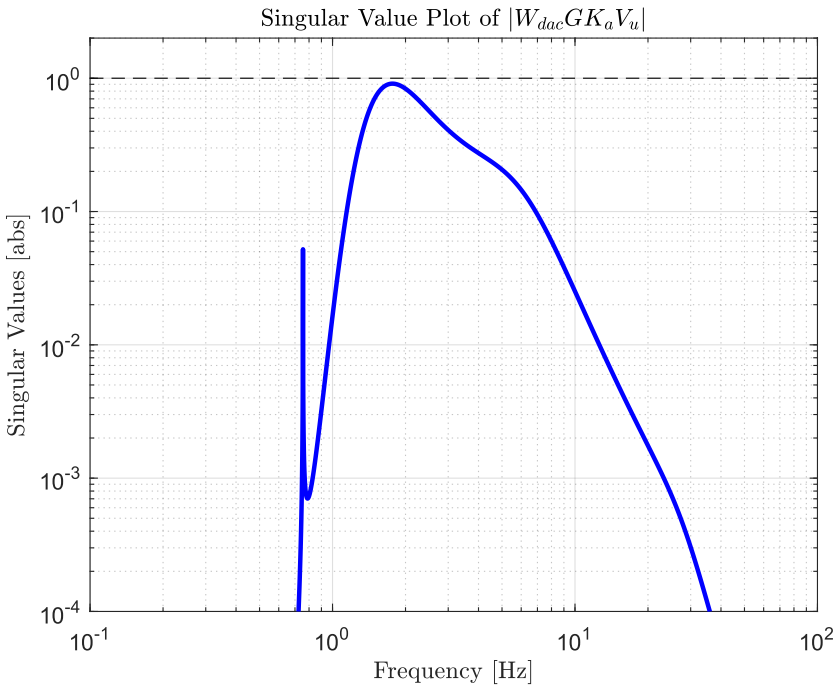

Figure 4.12: Singular values of the $|W_{dac}\hat{G}K_{\mathrm{a}}V_{\mathrm{u}}|_\infty$ optimization path, confirming that $|GK_{\mathrm{a}}u_{\mathrm{d}}| < |W_{\mathrm{dac}}^{-1}|$

Figure 4.13 shows the open-loop equivalence of the DAC noise, which touches the inverse of the weighting filter as expected.

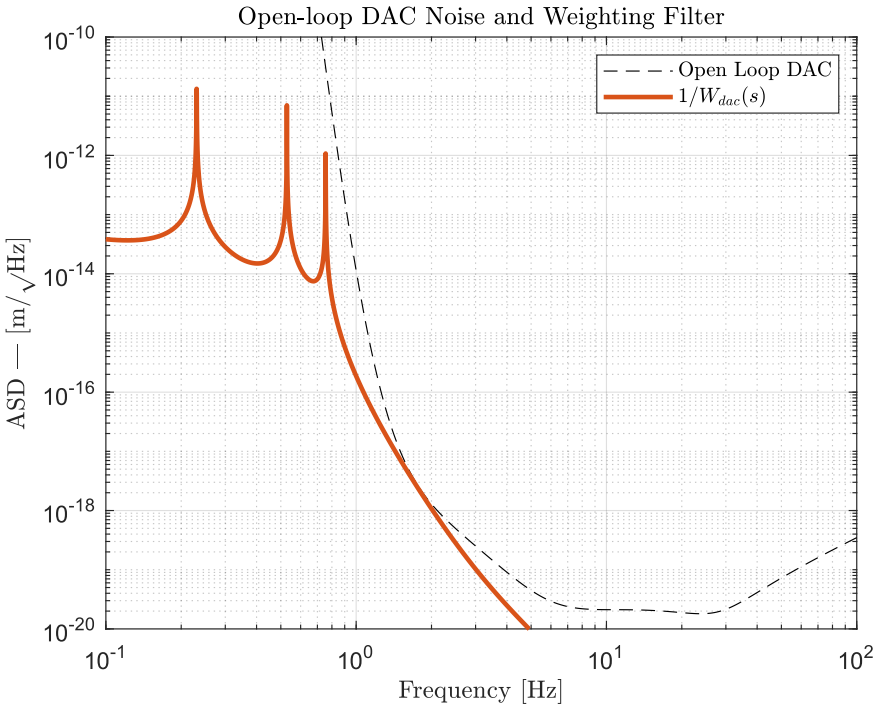

Figure 4.13: Open-loop DAC noise equivalence and inverse of the W_{dac} filter

Figure 4.14 shows the Nyquist plot for the loop gain $L(s) = G(s, \boldsymbol{\psi_{opt}})K_{\text{a}}K(s)$. The loop-gain again touches the requested modulus margin of MM = 0.10 at multiple instances, which is the result of the $\mathcal{H}_\infty$-bound concerning the robustness constraint.

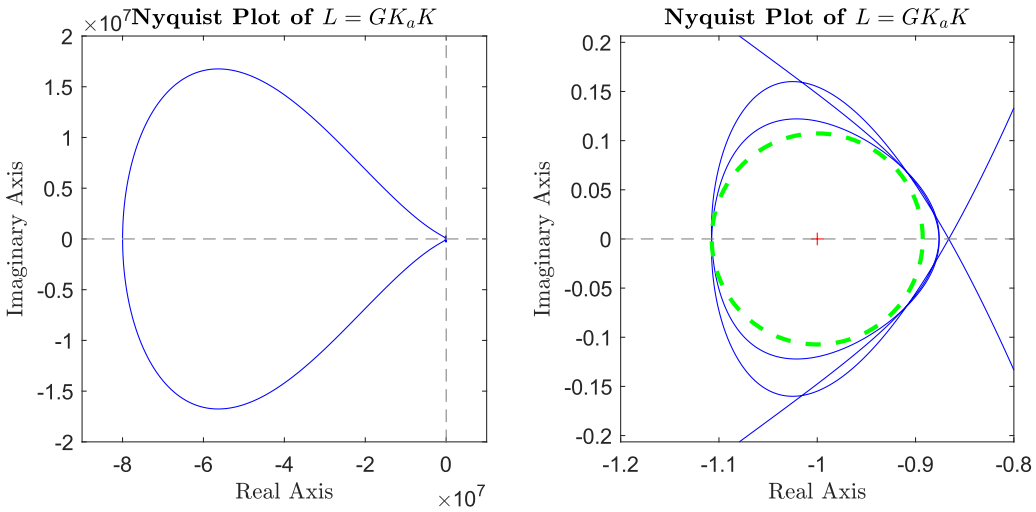

Figure 4.14: Nyquist plot for loop gain $G(s, \psi)K_aK(s)$

4.3.4 Optimal Topology of the Suspension

The main aim of this specific optimization is to investigate how the optimizer would place the masses of the suspension over the available space. Figure 4.15 shows the frequency response of the nominal, and optimal plant.

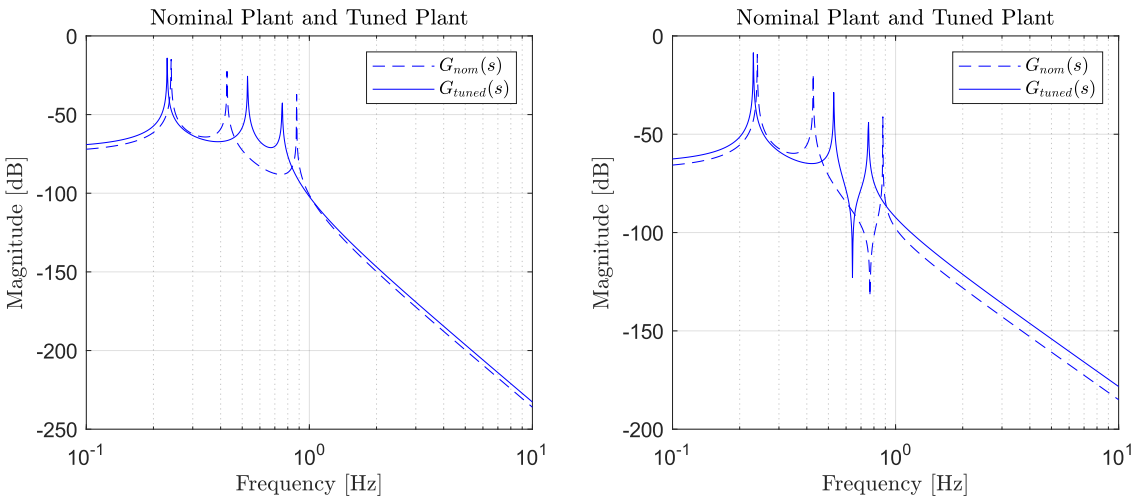

Figure 4.15: Optimal plant $G(s, \boldsymbol{\psi_{opt}})$

Table 4.2 shows how the optimizer has changed the lengths of the individual pendulums. Figure 4.16 shows a schematic comparison between the nominal and optimal configuration. The next chapter will elaborate on why this distribution of the masses may be favourable over the original configuration.

	$\boldsymbol{l_1}$	$\boldsymbol{l_2}$	$\boldsymbol{l_3}$
nominal	2	2	2
optimal	3.62	1.38	1.00

Table 4.2: Nominal and optimal lengths of the pendulums

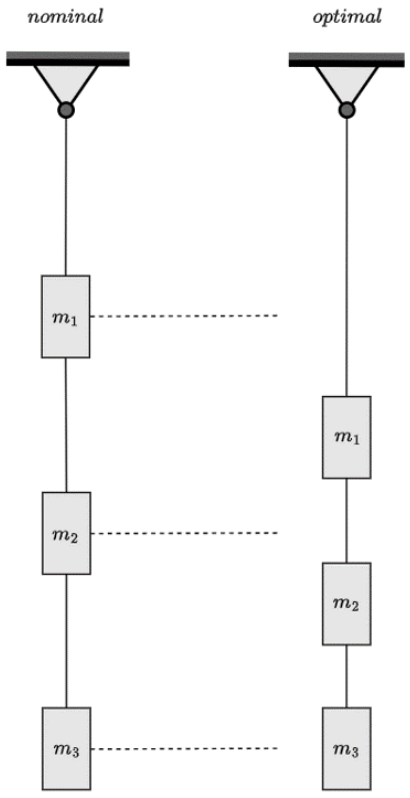

Figure 4.16: Nominal and optimal configuration of the masses of the suspension

Chapter 5

Discussion

In the previous chapters, the suitability of non-smooth mixed $\mathcal{H}_2/\mathcal{H}_\infty$ controller synthesis for a payload suspension was investigated. First, the description and the requirements for the control system were translated into a mathematically relevant control problem formulation. This required to define both $\mathcal{H}_2$-constraints for an energy based optimization, while also addressing hard limits over the entire frequency range for the open-loop equivalent DAC noise. Moreover, an extra $\mathcal{H}_\infty$-constraint was introduced to enforce robustness of the system against process variations.

In the previous chapter, several variations of the optimization problem at hand were investigated. First, the analysis of the base-line optimization that was shown in Chapter 4.1 and 4.2 is discussed. This is followed by analysing the extensions involving the complete suspension mechanics and length topology optimization shown in Chapter 4.3.1 and 4.3.2. Since the results for all optimizations in terms of the closed-loop RMS reduction, stability and open-loop equivalent DAC are quite similar, they are discussed only once. The discussion of the results generally holds for all the optimizations that are shown in the previous chapter.

5.1 Analysis of the Results

The necessity of utilizing the non-smooth mixed optimization was already argued in Section 2 and 3. It is the result of the presence of both $\mathcal{H}_2$- and $\mathcal{H}_\infty$-type of constraints that follow from the requirements for the control system for the payload suspension. From the results that are shown in Section 4, it can be generally inferred how the optimizer solves for a controller and actuator distribution that fulfills these requirements.

The main target for the control system is the attenuation of the effects of seismic disturbances to the longitudinal degree of freedom of the mirrors that make up the optical resonators in the observatories arms. Therefore this is defined as the minimization argument in the mathematical definitions of the optimization problem. From the results it can generally be observed that the RMS of the seismic noise is suppressed, as long as the constraints admit this. These constraints consist of a limit on the energy of the control signal, an $\mathcal{H}_\infty$-bound on the open-loop equivalence of the DAC noise and the sensitivity function to guarantee a desirable robustness margin. Some additional plots show how the optimizer deals with these constraints, which provides additional insight on what the controller tries to achieve.

Consider the sensitivity function $S(s)$ that maps the seismic disturbance to the mirror motion ($x_\mathrm{d} \to \hat{x}$). This transfer function simultaneously dictates the distance between the loop gain $L(s)$ and the critical point on the Nyquist plot. The robustness filter $W_\mathrm{rob}(s)$ is imposed to this sensitivity function, since the inverse of the nominal sensitivity peak $|S(s)|_\infty$ is exactly the modulus margin. It can be observed for each Nyquist plot that the loop gain touches a circle, of which the radius coincides with the requested modulus margin, multiple times. The cause of this can be traced back to the magnitude of the frequency response of the sensitivity function. Generally, the magnitude of the sensitivity function looks like shown in Figure 5.1, which results from the optimization study that was carried out as shown in Section 4.1.

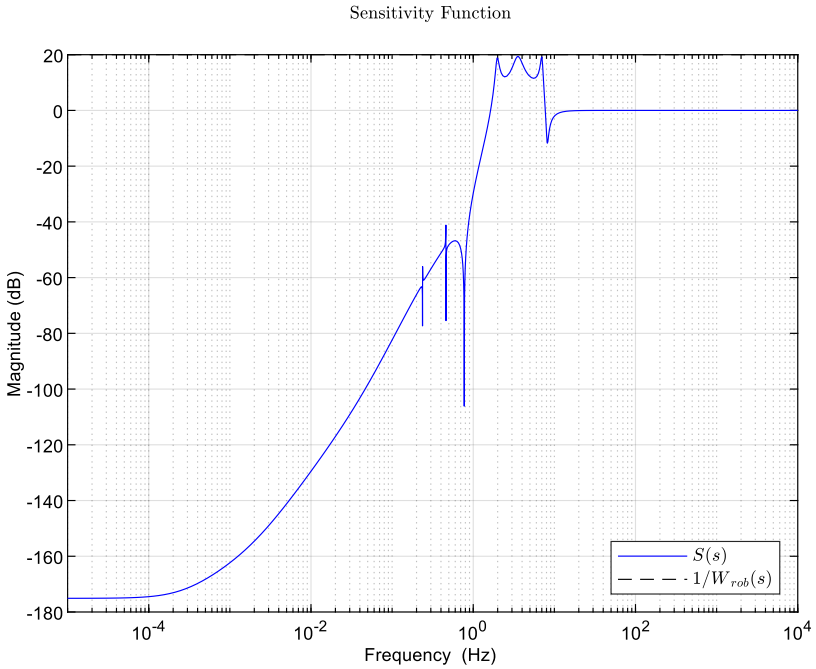

Figure 5.1: Sensitivity function $S(s)$ and the inverse robustness filter $W_\mathrm{rob}^{-1}(s)$

For lower frequency, the gain of the sensitivity function is noticeably small, since the attenuation of seismic noise mainly occurs in the low frequency region. In the region between $1-10$Hz, it is noticeable how the controller puts additional effort such that $S(s)$ coincides multiple times with the weighting filter. This is exactly the cause for the multiple coinciding points between $L(s)$ and the modulus margin. After all, it shows exactly why the robustness constraint was introduced in the first place; to limit high peaking of $S(s)$ towards high frequencies, such that the system is sufficiently far away from instability. Apparently the controller must put in some additional effort in this frequency range to push down the sensitivity

peak at multiple instances.

Generally, we wish to see something similar for the open-loop equivalence of the DAC noise. As long as the DAC noise does not exceed its acceptable limits, we want to increase the effort spent by the controller and actuators to compensate for the seismic vibrations. Consider the DAC noise related optimization statement $|W_{\text{dac}}(j\omega)G(j\omega)K_{\text{a}}V_{\text{u}}(j\omega)|_\infty < \gamma_{\text{d}}$. If the optimizer is able to find a suitable controller, the following should hold.

$$|W_{\text{dac}}(j\omega)G(j\omega)K_{\text{a}}V_{\text{u}}(j\omega)|_\infty < \gamma_{\text{d}} \quad \rightarrow \quad |G(j\omega)K_{\text{a}}V_{\text{u}}(j\omega)| < \gamma_{\text{d}} \cdot |W_{\text{dac}}^{-1}(j\omega)| \ \ \forall \ \ \omega \tag{5.1}$$

A value of $\gamma_{\text{d}} < 1$, indicating that Equation 5.1 can then be simplified to:

$$|G(j\omega)K_{\text{a}}V_{\text{u}}(j\omega)| < |W_{\text{dac}}^{-1}(j\omega)| \ \ \forall \ \ \omega \tag{5.2}$$

Indicating that, for a value of $\gamma_{\text{d}} < 1$, the optimizer is thus able to keep the open-loop equivalent DAC noise spectrum below the weighting filter for all frequencies. Figure 5.2 shows the open-loop equivalent DAC noise from section 4.1 and the individual contributions of each actuator.

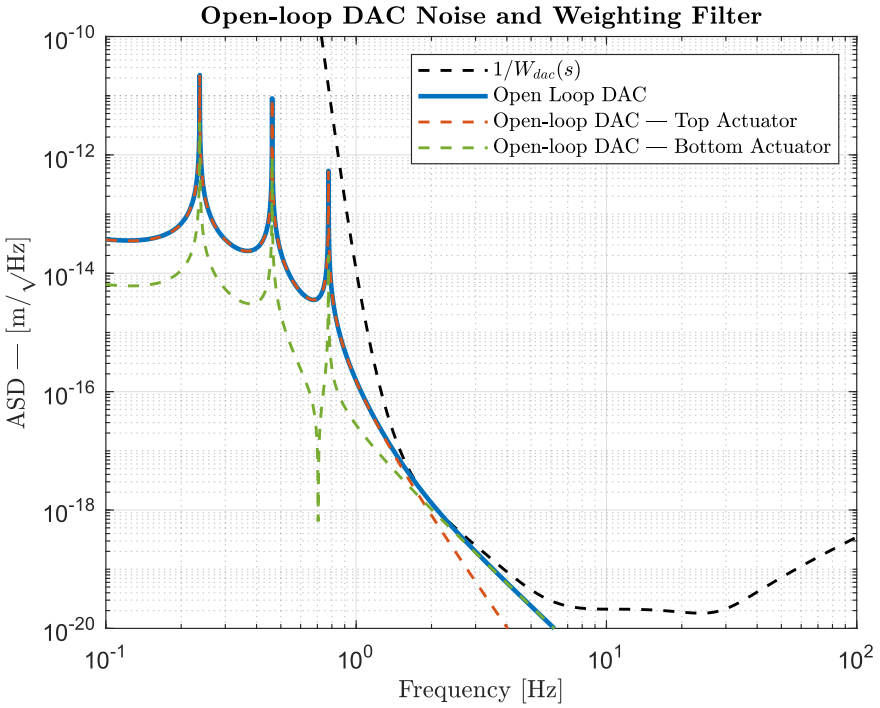

Figure 5.2: Open-loop DAC noise equivalence and individual actuator contributions

The open-loop DAC noise equivalence generally stays well below the $\mathcal{H}_\infty$ related weighting filter $W_{\text{dac}}(s)$ and touches the inverse of weighting filter often at a frequency around 2Hz. Therefore, the controller and actuators are generally chosen by the optimizer such that Equation 5.2 holds. Since the controller itself does not contribute the open-loop equivalent DAC noise, the sizing of the actuator is mainly attributed to how the open-loop DAC is placed against the inverse of the weighting filter. For all optimizations, the actuator gains do not run into the imposed bounds. Again, it can be observed that the seismic noise is attenuated as long as the limit on the open-loop DAC noise is not exceeded. Specifically in the case showed in the figure above, it may be noted how the optimizer wraps the sum of the two individual contributions around the inverse of the weighting filter around the 2Hz point. It was assumed that the 3Hz point would be the most challenging point to suppress the DAC noise initially, which is confirmed closely by the highest singular value repeatably occurring at around 2Hz for all optimizations. From the singular value plot that is shown for each optimization study, it can be concluded that the values for γ_{d} are very close to 1. This indicates that the optimizer is able to push the limits of the system to the hard limits that were imposed in the form of $\mathcal{H}_\infty$-bounds.

Sub-Optimal Solutions

Customarily, the effects of the fact that the cost function that is associated with all the optimizations is not convex is observed quite often during the optimizations. Since the cost function, for which the optimizer aims to find a suitable controller is non-convex, the optimal solution that the algorithm finds is often not a global optimum, but a local optimum. This might be fine, as the closed-loop system that results from the controller synthesis often still meets the requirements.

We can observe these effects mainly from the resulting γ_∞ values concerning the $\mathcal{H}_\infty$-constraints[1]. One would like to have the optimizer to return values for γ_∞ of exactly 1. This would indicate that the performance is pushed to its hard limits that were imposed regarding the open-loop DAC noise requirement and the additional robustness constraint. Often, it was observed that the values for γ_∞ would settle at values lower than one, indicating that there is room for improvement in terms of additional performance. Performance here is expressed as a reduction of the RMS of closed-loop seismic noise, which is the minimization argument of the optimization. This is typically attributed to the non-convexity of the optimization problem.

There is a workaround for the aforementioned phenomena. The optimizer allows to start the optimization at a user-specified amount of initialization points, where the optimizer starts to find a solution via gradient descent methods. By choosing a sufficiently large amount of initialization points, one could then somewhat assume that the solution that is found is close to a globally optimal solution.

5.1.1 Actuation at all Suspension Stages

The results that are shown in Chapter 4.1 show that the optimization results in a controller and actuator distribution that closely meets the $\mathcal{H}_\infty$-bounds. This indicates that there is not much room left for improving the performance, because the controller pushes the system already to its limits. However, the attenuation of the seismic disturbance is not within the specifications. For this reason, a similar study was carried out, that included an additional actuator at the mirror stage to increase the capability of the control system to suppress the seismic noise.

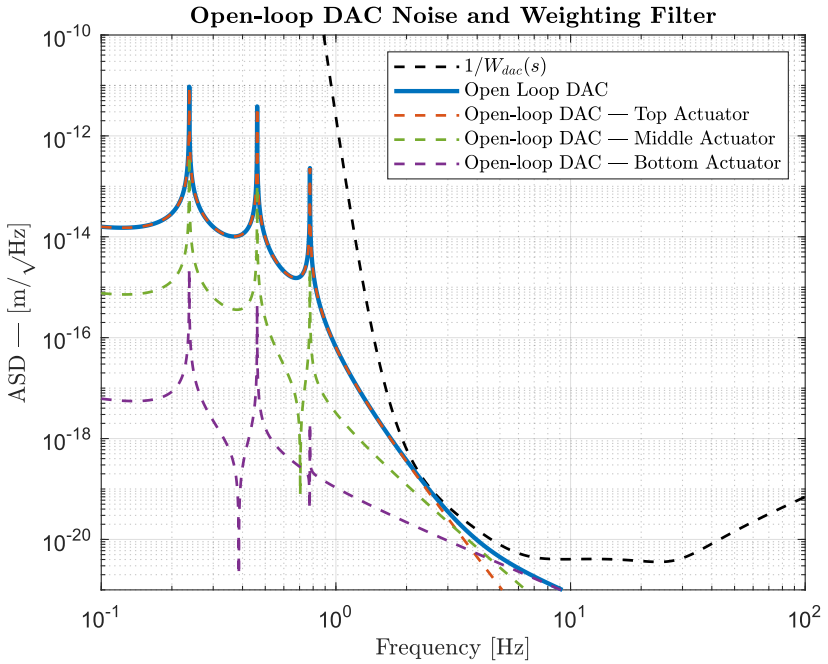

Figure 5.3: Open-loop DAC noise equivalence for the case with actuation at all three stages. The individual contributions are also shown

[1] The values γ_∞ correspond to the values of both γ_d and γ_r, hence $\gamma_\infty = [\gamma_\mathrm{d} \quad \gamma_\mathrm{r}]$

From the results that are shown in the paper, it can be concluded that the actuation at the mirror stage is necessary to meet all the requirements that are imposed on the control system. Since the mirror stage only provides a roll-off of -40dB/decade, it was initially expected that the actuation of the mirror must be very small to satisfy the open-loop DAC noise constraint. The corresponding open-loop DAC noise equivalence and the individual contributions of the actuators are shown in Figure 5.3.

From this plot, it can be seen how the additional actuator is sized such that the high-frequency asymptote of the open-loop equivalent DAC noise gets closer to the inverse of $W_{\mathrm{dac}}(s)$. This corresponds with the open-loop equivalence DAC noise from the actuation at the mirror stage. From this plot, it can be seen that the bottom actuator can be sized larger. There still is some headroom between the contribution of the bottom actuator and the inverse of the weighting filter. It is possible to manually increase the sizing of the actuators until the imposed limit, as long as it does not significantly affect the stability margins. Although the actuator is sized quite small, it significantly improves the systems seismic attenuating performance. Reasons for this could be introducing more actuation power and giving more flexibility in design for the optimizer due to an additional entry to the controller transfer matrix $K(s)$.

5.2 Analysis of the Suspension Optimization

Two case studies were investigated, where the optimization was extended with a parametric optimization of the suspension. From the length topology optimization that was shown in Chapter 4.3.2, it can be concluded that it is apparently optimal to increase the pendulum length, the more that you move up the chain. A possible reasoning for this is as follows; Increasing the length of the pendulum reduces the natural frequency of a pendulum, since $\omega_n = \sqrt{\frac{g}{l}}$. Reducing the eigenfrequency results in that the roll-off of the transfer function starts at a lower frequency, hence the transmissibility of the suspension is changed such that seismic noise is better suppressed towards high frequencies. Apparently, it is more favourable to do so at the top stage of the pendulum, such that the seismic disturbance is decoupled more at this stage. This is also supported by Figure 4.11, since the main performance gain occurs at lower frequencies, where the seismic disturbance is significantly reduced. The optimal pendulum lengths decrease further down the chain. This means that the dynamics become faster as you go down the suspension chain. This is actually in line with the expectation for the actuation. It was assumed initially that the top stage is likely to be assigned to compensate for the coarse, low frequency noise and the actuation at the mirror for the fine, high frequency part of the noise.

5.3 Validity of the Results

Even though the results show that the optimization algorithm is able to find a solution that meets all the requirements, there are still some important notes that should be considered. First of all, as mentioned before, the solution is likely not a global optimum of the optimization space, but it is close. This could mean that there exists a better solution. Now, for most applications this might be fine and most of this can be mitigated by starting the algorithm at a sufficient amount of starting points in the optimization space, as mentioned before. The controller may be improved by some additional manual tuning. However, in any case, the optimizer should fulfill its goal to improve controller design and significantly speed up the process to allow to quickly evaluate the performance for many suspension configurations.

Moreover, since the algorithm is initialized with an $\mathcal{H}_2$-optimal controller, the state space of the controller has the same number of states as the generalized plant for this problem, which has 28 states. Adding additional $\mathcal{H}_\infty$-constraints to the $\mathcal{H}_2$-optimization may result in synthesised controllers with a more complex structure. More complex controllers do however enable the use of simpler controllers. Such controllers may be achieved by taking a minimal realization or by manually adjusting the frequency response of the controller. It might be beneficial to check if the controller can be simplified, such that the number of states and consequently the computation time of the control action can be reduced. Of course, such adjustments are likely limited by the expense of performance degradation of the closed-loop system.

In order to get a sense of how close the solutions are to a global optimum, it can be of interest to compare the γ values of multiple optimizations that are initialized at 100 random starting points on the cost function. Generally, over multiple optimizations, the optimizer converged to values for γ_{d} close to one within

a range of about ±6% of the average value. Similarly, values for γ_r converged to value that were within ±5% of the average value. The limited spread of these values indicate that the optimizer converges to similar solutions over many optimizations. This could be an indication that the $\mathcal{H}_\infty$-constraints result in an optimum that is close to a global one. The optimal actuator gains are usually sized within the same order of magnitude, with a spread of about ±25%. This can be an indication that the chosen actuator distribution is fairly optimal, in combination with the synthesized controller. Moreover, the attenuation of the seismic noise in terms of the RMS of the effective seismic disturbance at the mirror stage stayed within ±7% of the average result over five optimizations. This could also indicate that the solution is somewhat close to the unconstrained $\mathcal{H}_2$-optimal solution.

An additional consideration is that the optimizer sometimes synthesises a controller that is unstable on itself, but stabilizes the loop. That is, some poles of the controllers are sometimes situated in the RHP. The controller makes up for this, by introducing an equal amount of CCW rotations of the critical point, such that an unstable controller can still be a stabilizing controller. Unstable controllers typically require anti-windup, to avoid excessive growth of the control signal. Whenever an unstable controller is not desirable, some additional constraints on the structure of the controller should be imposed to make sure that the controller is both stabilizing and stable on itself. This is possible to do with the proposed mixed synthesis algorithm.

Finally, the study that was shown in the previous chapters was based on a simplified model of the suspension that omits possible non-linearities and parasitic dynamics to name a few. For the optimization of both controller and the dynamics of the suspension, the optimizer is allowed to place the masses over the available space to improve the performance of the seismic attenuation capabilities of the payload suspension. However, increasing the length of the pendulum wires necessarily decreases the frequencies of parasitic modes, such as the violin modes of the wires, causing additional problems. This is not taken into account for the simplified model of the payload suspension, but will form a significant limit for the real system. Additional effort could be necessary to design a controller that is suitable for the actual dynamics, although the solution process that is proposed here should still remain the same. The next paragraph elaborates on some of the additional details that could be considered upon further research.

5.4 Recommendations for Future Research

The analysis in this research has considered a simplified model of the payload design without consideration of any parasitic dynamics that are inherent to the actual mirror suspension design. This section proposes some relevant extensions for future research, both on dynamical aspects and control related topics.

5.4.1 Dynamics

The dynamics of the payload are based on a simplified model of the actual system, which is a multi degree-of-freedom pendulum. Any parasitic dynamics that are inherently present in the real system are omitted in this study. Moreover, only a few stages of the multi-pendulum setup are considered and not the complete suspension.

Extension of the Dynamics

A logical step in the extension of this research would be to include the complete chain of cascading pendulums. First of all, the passive filtering is done by a set of cascading pendulums, that are above the actively controlled payload suspension. This passive suspension significantly changes the dynamics of the system. In this study they are lumped into the LTI model for the colouring of white noise to seismic noise. However, it could be interesting to consider the complete dynamics of the whole suspension chain to analyse the influence of the parameters of the passive suspension to the total performance that can be attributed to the suspension. Furthermore, the seismic disturbance filter should be parameterized in case of a mechanical optimization. After all, a change in the dynamics of the payload suspension would also reflect as a change in the filter V_x.

Considering Parasitic Dynamics

The intrinsic dynamics of the suspension can be represented quite accurately by a set of cascading pendulums. Nonetheless, the wires that suspend the stages of the pendulum are not infinitely stiff and have a

high quality factor. The $\mathcal{Q}$ factor of the suspension wires is high, since they are manufactured from fused silica wires that aim to minimize the influence of thermal noise on the mirrors. The suspension wires that connect the stages and test mass will introduce high frequency parasitic dynamics to the dynamics of the system which were not yet considered for the design in this research.

One important type of parasitic dynamics are the so called violin modes of the fused silica suspension wires. This type of parasitic dynamic follows from the resonating of the high $\mathcal{Q}$ wires that suspend the mirrors [22][29]. The high frequency vibration due to the violin modes will effectively also result in oscillation of the mirror, thus decreasing the sensitivity of the telescope. So far, this study has omitted the violin modes, but for a more thorough and accurate analysis and controller design, these modes are important to consider. They can have a significant effect on the operation of the telescope and the design of stabilizing controllers.

The mirrors also have a parasitic tilting degree of freedom, which was not yet considered during this study. Including additional couplings due to tilting of the mirror could be a logical topic for future research to assess their possible impact on the performance of the payload suspension.

5.4.2 Control

Besides an extension of the dynamics, there are also some logical steps in the extension for the controller design. The current analysis is done in the continuous domain. However, most of the times a control system is implemented on a computer and this requires a controller that can be described in the $\mathcal{Z}$-domain, which has some implications that are important to consider for the actual design. Furthermore, since the dynamics of the mirror suspension are not set in stone, it can be very interesting to perform optimizations that optimize for the controller and dynamics of the system simultaneously.

Discrete Controller Design Implications

Digital controller design provides great flexibility in new controller design implementation. There are however some considerations to take into account for the controller design. First of all, discrete controller implementation typically introduces one sample time of delay due to computation time for the control action. This delay may be reduced by immediately sending the control action. This however comes at the expense of more jitter of the digital control signal. An additional half of a sample time delay is introduced due to a zero-order-hold reconstruction. Delay reduces the phase margins of a system and if the phase margin is not sufficiently high to account for this, the discrete equivalent of the continuously designed controller could destabilize the system.

The delay is not expected to be the main concern for discrete controller implementation. The optimization algorithm computes a controller such that a closed-loop transfer function is shaped, by taking some frequency content from a desired operation range to other frequencies, where performance is less or not important. This follows from Bode's sensitivity integrals [40]. Delays do however worsen the achievable performance that can be achieved [31]. For continuous design, the controller can distribute the frequency content of closed-loop transfer functions up to infinite frequency. For discrete controller design, the controller can only distribute the frequency content up to the Nyquist frequency. This is a fundamental limit for discrete controller design. By designing a discrete controller from the beginning, one can take these implications into account from the start of the design process.

Simultaneous Optimization of Dynamics and Control

The design of the payload and the rest of the suspension is not yet fixed. There is still quite some freedom in the design of the suspension and thus its parameters. The non-smooth optimization approach that is used in this study allows for defining tunable parameters and transfer functions. This property of the optimizer was used to tune the size of the actuators in order to satisfy the requirement on the open-loop DAC noise. It is possible to define some dynamics or parameters of the pendulum, such as length of the pendulum or mass of the stages to name a few, that can be optimized simultaneous with the computation of the controller. This could potentially lead to a fully optimized suspension with an improved performance over the nominal dynamics. An implication of optimizing the suspension is that this also influences the spectrum of the residual seismic noise present at the mirror stage. The seismic noise model V_{x} should account for this by parameterizing this model accordingly. This research showed

how the optimizer is able to optimize the dynamics of the suspension for a simplified case study. However, implications on parasitic modes amongst other problems were not yet considered for these case studies and hence would be a logical addition for further research.

Feedforward Control

Feedforward control has been widely applied in vibration isolation control strategies, to directly compensate for a measured disturbance. A great benefit is that disturbance feedforward control does not suffer from delays that a feedback control scheme inevitably encounters. A computation of a feedforward control action could be based on immediate measurements of the seismic disturbance at the beginning of the suspension chain [39]. Furthermore, a feedforward controller can in general improve a system's performance significantly, without destabilizing the loop. The feedforward controller can be taken into account in the optimization problem, such that both feedback, feedforward controllers and possibly mechanical parameters can be optimized in one go.

Also, the implementation of a feedforward controller can give more flexibility in the overall controller design. The controller design can now be distributed over two controllers. This alleviates the design of the feedback controller concerning the stability constraint, since the control action is now distributed over two controller transfer functions. The DAC noise constraint is however still relevant for the feedforward controller. The non-smooth optimization approach allows for easy integration of the optimization of an additional feedforward controller alongside the feedback controller.

A drawback of the implementation of a feedforward controller would be that additional measurements of floor vibrations at the base of the suspension are required to directly act on the seismic motion. This could possibly introduce noise to the system and this leads to an important consideration of the additional benefit of the implementation of a feedforward controller. The noise cancelling control action from the feedforward controller is also filtered by the suspension when moving the sensors for measuring these disturbances further up the chain. Moreover, this can be taken into account by the controller, even by fusing inputs of multiple sensors. Possible benefits of feedforward control should in the end be found out rather quickly utilizing optimal control based design. After all, the optimizer should allow to quickly assess the performance of the system with additional measures such a a feedforward controller.

Chapter 6

Conclusion

Summarizing, this research has investigated how the requirements of a control system for the global control system of the test-mass suspensions can be condensed in a mathematically relevant optimization problem. From the requirements it is clear that the problem statement can be captured by both $\mathcal{H}_2$- and $\mathcal{H}_\infty$-constraints. For this reason,the suitability of a mixed non-smooth synthesis method to solve for a controller and actuator distribution was investigated.

The attenuation of the seismic disturbance was found to be a typical energy based minimization, for which the $\mathcal{H}_2$-control paradigm is arguably the most suitable method of choice. The same holds for restricting the energy of the control actions within the capabilities of the DAC. The strict limit over the entire frequency range that should be imposed on the open-loop equivalent DAC noise was best captured by an $\mathcal{H}_\infty$-constraint. Additionally, an $\mathcal{H}_\infty$-constraint on the sensitivity function allows to guarantee a desirable stability margin to account for possible process variations.

A mixed non-smooth optimization algorithm was proposed, to solve the non-smooth cost function that is associated with the optimization problem for the suspension. The nonsmooth optimizer is generally able to find a suitable controller and actuator distribution, that attenuates the seismic disturbance well enough, such that the optical resonators can be locked and the telescope is able to stay within its small linear operating range. Actuation at the mirror and the two stages above appeared to be necessary to lock the FP cavities according to the specifications. Generally, the optimizer chooses the controller and actuation such that the $\mathcal{H}_\infty$-weighting filters maintain an acceptable open-loop DAC noise and robustness margin. Moreover, the associated open-loop and closed-loop transfer function for the DAC noise and sensitivity function respectively touch the inverse of the weighting filter, indicating that the optimizer does exactly what we expect it to do after all: minimize the effects of the seismic activity of the earths surface, as long as the hard limits allow this. Since the γ values for the $\mathcal{H}_\infty$-channels are very close to one, this is exactly what the optimizer is able to achieve.

All in all it can be said that the control problem can be captured well by a mixed $\mathcal{H}_2/\mathcal{H}_\infty$ optimization definition. The optimizer is generally able to deal with the associated non-smooth cost function. Even though the solution is not necessarily a globally optimal one, the controller and actuator distribution are able to fulfill all the requirements for the control system, given that the suspension is actuated at all three stages. The research is based on a simplified model of the suspension and is thus not directly applicable to any real system yet. However, the results for the simplified case study showcase that the optimization method itself lends itself very well for the control challenge at hand and could be very suitable for aiding controller design and agile performance assessment for these type of gravitational wave related applications. Since the optimizer also allows to tune dynamic systems, this work could be extended in a completely integrated controller and mechatronics for a fully optimized design. Some examples of a simplified suspension optimization were shown to improve the performance of the suspension.

This study considered a simplified model of the suspension. Moreover, the simultaneous optimization of the suspension did not take any consequences regarding parasitic modes into account. Future research regarding this topic could include inherently present parasitic dynamics. Examples of such parasitic modes are the violin modes of the suspension wires and tilt couplings of the mirror. The use of more accurate models of the suspension that include these parasitic dynamics would be in place. An additional

feedforward controller that compensates directly for the measured seismic disturbances may improve the performance of the payload suspension. Including feedforward control would therefore be an interesting addition to the control system design for a payload suspension.

Bibliography

[1] J Aasi et al. "Advanced Ligo". In: *Class. and Quantum Grav.* 32 (2015).

[2] B P Abbot et al. "Multi-messenger Observations of a Binary Neutron Star Merger". In: *The Astrophysical Journal Letters* 848 (2017).

[3] B P Abbot et al. "Observation of Gravitational Waves from a Binary Black Hole Merger". In: *Phys. Rev. Lett.* 116 (2016).

[4] B P Abbot et al. "Observation of Gravitational Waves from a Binary Neutron Star Inspiral". In: *Phys. Rev. Lett.* 119 (2017).

[5] R Abbot et al. "Compact Binary Coalescences Observed by LIGO and Virgo during the First Half of the Third Observing Run". In: *Phys. Rev. X.* 11 (2021).

[6] R Abbot et al. "Compact Binary Coalescences Observed by LIGO and Virgo during the First Half of the Third Observing Run". In: *Phys. Rev. X.* 11 (2021).

[7] R Abbot et al. "Compact Binary Coalescences Observed by LIGO and Virgo during the Second Part of the Third Observing Run". In: *Phys. Rev. X.* 13 (2023).

[8] F Acernese et al. "Advanced Virgo: a second-generation interferometric gravitational wave detector". In: *Class. and Quantum Grav.* 32 (2015).

[9] A Alloca et al. "Interferometer Sensing and Control for the Advanced Virgo Experiment in the O3 Scientific Run". In: *Galaxies* (2020).

[10] F Amann et al. "Site Selection Criteria for the Einstein Telescope". In: *Review of Scientific Instruments* 91 (Aug. 2020). DOI: 10.1063/5.0018414.

[11] P Apkarian, D Noll, and P Pellanda. "Nonsmooth H_∞ Synthesis". In: *IEEE Transactions on Automatic Control* (2006), 71–86 vol.51.

[12] P Apkarian, D Noll, and A Rondepierre. "Mixed H_2/H_∞ Control Via Nonsmooth Optimization". In: (2009).

[13] G Bakshi. *3 Key Specifications When Using a DAC as a Programmable Voltage Reference*. 2021.

[14] S Braccini et al. "Measurements of the seismic attenuation performance of the VIRGO Superattenuator". In: *Astroparticle Physics* 23 (2005).

[15] Moore C, Cole R, and Berry. "Gravitational-wave sensitivity curves". In: *Classical and Quantum Gravity* (2015).

[16] *LIGO Livingston*. https://www.ligo.caltech.edu/system/avm_image_sqls/binaries/30/medium/ligo-livingston-aerial-02.jpg?1447107179.

[17] J Casanueva. "Control of the Gravitational Wave Interferometric Detector Advanced Virgo". PhD thesis. University Paris-Sud, 2017.

[18] K Chamberlain and N Junes. "Theoretical physics implications of gravitational wave observation with future detectors". In: *Phys. Rev. D.* 96 (2017).

[19] M van Dael et al. "Control of the laser frequency in the Virgo interferometer: Dynamic noise budgeting for controller optimization". In: *Astroparticle Physics* 164 (2025).

[20] J Doyle. "Guaranteed margins for LQG Regulators". In: *IEEE Transactions on Automatic Control* (1978), pp. 756–757.

[21] J Doyle and K Zhou. *Essentials of Robust Control*. Pearson, 1997.

[22] S Großler et al. "Damping and tuning of the fibre violin modes in monolithic silica suspensions". In: *Classical and Quantum Gravity* (2004).

[23] J Heefner. *Digital Controls, ADC and DAC Research and Development for LIGO II*. https://dcc.ligo.org/public/0033/G010012/000/G010012-00.pdf.

[24] H Hindi, B Hassibi, and S Boyd. "Multiobjective H2/Hinfinity-optimal control via finite dimensional Q-parametrization and linear matrix inequalities". In: vol. 5. July 1998, 3244–3249 vol.5. DOI: 10.1109/ACC.1998.688463.

[25] N Holland. *A Systems Approach to Evaluating the Status of ET-LF Seismic Attenuation Proposals*. https://agenda.infn.it/event/32907/contributions/200472/. 2023.

[26] L Jabben. "Mechatronic Design of a Magnetically Suspended Rotating Platform". PhD thesis. TU Delft, 2007.

[27] A Keemink. *University of Twente: Control System Design for Robotics, Course Materials*. 2023.

[28] X Koroveshi et al. "Cryogenic payloads for the Einstein Telescope: Baseline design with heat extraction, suspension thermal noise modeling, and sensitivity analyses". In: *Physical Review D* 108.12 (Dec. 2023). ISSN: 2470-0029. DOI: 10.1103/physrevd.108.123009. URL: http://dx.doi.org/10.1103/PhysRevD.108.123009.

[29] N A Lockerbie et al. "First results from the 'Violin-Mode' tests on an advanced LIGO suspension at MIT". In: *Classical and Quantum Gravity* (2011).

[30] F Matichard et al. "Seismic isolation of Advanced LIGO: Review of strategy, instrumentation and performance". In: *Class. Quant. Grav.* 32 (2015).

[31] C Mohtadi. "Bode's integral theorem for discrete-time systems". In: *IEE Proceedings* 137 (1990).

[32] C Mow-Lowry and D Martynov. "A 6D interferometric inertial isolation system". In: *Class. Quantum Grav.* 36 (2019).

[33] RH Munnig Schmidt, G Schitter, and J van Eijk. *The design of high performance mechatronics. High-tech functionality by multidisciplinary system integration*. English. Netherlands: IOS Press, 2011. ISBN: 978-1-60750-825-0.

[34] A Oppenheim and R Schafer. *Discrete-Time Signal Processing*. Pearson, 2014.

[35] K Riles. "Gravitational waves: Sources, detectors and searches". In: *Progress in Particle and Nuclear Physics* 68 (2013), pp. 1–54. ISSN: 0146-6410. DOI: https://doi.org/10.1016/j.ppnp.2012.08.001. URL: https://www.sciencedirect.com/science/article/pii/S0146641012001093.

[36] N Robertson. "Laser interferometric gravitational wave detectors". In: *Class. Quantum Grav.* 17 (2000).

[37] B F Schutz. "Gravitational wave astronomy". In: *Classical and Quantum Gravity* 16.12A (1999), A131. DOI: 10.1088/0264-9381/16/12A/307.

[38] S Skogestad and I Postlethwaite. *Multivariable Feedback Control*. John Wiley & Sons, Ltd, 2006.

[39] S.T. Spanjer, H Köroğlu, and W.B.J. Hakvoort. "The Potential of Active Vibration Isolation Systems". In: (2023).

[40] G Stein. "Respect the Unstable". In: *IEEE Control Systems Magazine* (2003).

[41] ET Steering Comittee Editorial Team. *Design Report Update 2020 for the Einstein Telescope*. Tech. rep. ET Editorial Team, 2020.

[42] T Tsang et al. "Optimal sensor fusion method for active vibration isolation systems in ground-based gravitational-wave detectors". In: *Class. Quantum Grav.* 39 (2022).

[43] M Valentini. "The longitudinal control for the Advanced Virgo Plus gravitational wave detector". PhD thesis. Università di Trento, 2023.

Appendix A

Derivation of the Equations of Motion

The Equations of Motion (EoM) of the payload suspension are derived from those of a triple pendulum that is actuated at all stages. The EoM's are derived via Lagrangian mechanics. Consider an ideal physical model of a triple pendulum as shown in Figure A.1.

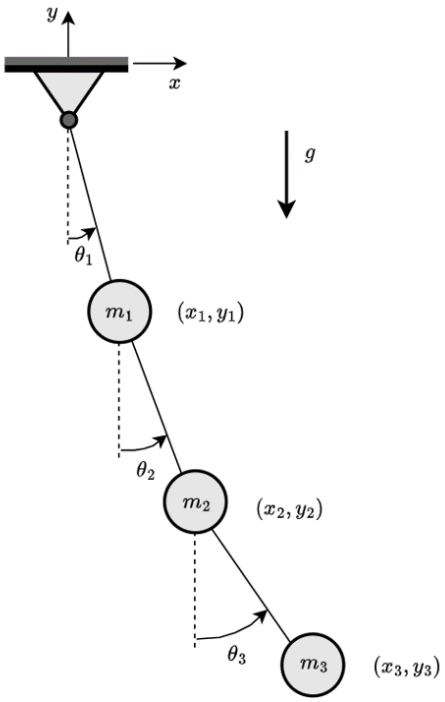

Figure A.1: Ideal physical model of a triple pendulum

This is a 3 DoF system, with the absolute pendulum angles as generalized coordinates, such that $\boldsymbol{q} = [\theta_1, \theta_2, \theta_3]^T$. The mass of each stage is denoted as m_i and the pendulum length by l_i. The values for these parameters are motivated by [28]. The wires that connect the pendulum stages are assumed to be massless. The pendulum stages are modelled as point masses. For notational simplicity, the cosine and sine terms are abbreviated to $s_i = sin(\theta_i)$ and $c_i = cos(\theta_i)$. The kinematic relationships between the Cartesian coordinates of the masses and the generalized coordinates are given by:

$$\begin{aligned} x_1 &= l_1 s_1 \\ y_1 &= -l_2 c_1 \\ x_2 &= l_1 s_1 + l_2 s_2 \\ y_2 &= -l_2 c_1 - l_2 c_2 \\ x_3 &= l_1 s_1 + l_2 s_2 + l_3 s_3 \\ y_3 &= -l_2 c_1 - l_2 c_2 - l_3 c_3 \end{aligned} \quad \xrightarrow[\frac{d}{dt}]{} \quad \begin{aligned} \dot{x}_1 &= \dot{\theta}_1 l_1 c_1 \\ \dot{y}_1 &= \dot{\theta}_1 l_2 s_1 \\ \dot{x}_2 &= \dot{\theta}_1 l_1 c_1 + \dot{\theta}_2 l_2 c_2 \\ \dot{y}_2 &= \dot{\theta}_1 l_2 s_1 + \dot{\theta}_2 l_2 s_2 \\ \dot{x}_3 &= \dot{\theta}_1 l_1 c_1 + \dot{\theta}_2 l_2 c_2 + \dot{\theta}_3 l_3 c_3 \\ \dot{y}_3 &= \dot{\theta}_1 l_2 s_1 + \dot{\theta}_2 l_2 s_2 + \dot{\theta}_3 l_3 s_3 \end{aligned} \tag{A.1}$$

The Lagrangian for the system is defined as the difference between kinetic energy $T(\boldsymbol{q}, \dot{\boldsymbol{q}})$ and potential energy $V(\boldsymbol{q})$.

$$\mathcal{L}(\boldsymbol{q}, \dot{\boldsymbol{q}}) = T(\boldsymbol{q}, \dot{\boldsymbol{q}}) - V(\boldsymbol{q}) \tag{A.2}$$

The Euler-Lagrange equations are then found as follows.

$$\frac{d}{dt}\frac{\partial \mathcal{L}(\boldsymbol{q}, \dot{\boldsymbol{q}})}{\partial \dot{\boldsymbol{q}}} - \frac{\partial \mathcal{L}(\boldsymbol{q}, \dot{\boldsymbol{q}})}{\partial \boldsymbol{q}} = 0 \tag{A.3}$$

The potential energy term and kinematic energy term for the 3 DoF pendulum are then derived using the kinematic relationships of Equation A.1 as follows.

$$V(\boldsymbol{q}) = m_1 g y_1 + m_2 g y_2 + m_3 g y_3 = -(m_1 + m_2 + m_3) g l_1 c_1 - (m_2 + m_3) g l_2 c_2 - m_3 g l_3 c_3 \tag{A.4}$$

$$T(\boldsymbol{q}, \dot{\boldsymbol{q}}) = \frac{1}{2} m_1 v_1^2 + \frac{1}{2} m_2 v_2^2 + \frac{1}{2} m_3 v_3^2 = \frac{1}{2} m_1 (\dot{x}_1 + \dot{y}_1)^2 + \frac{1}{2} m_2 (\dot{x}_2 + \dot{y}_2)^2 + \frac{1}{2} m_3 (\dot{x}_3 + \dot{y}_3)^2 \tag{A.5}$$

These terms are used to compute the EoM's of the pendulum via a piece of `Matlab` code that automatically produces the Lagrangian EoM's for a given T and V [27]. The EoM's resulting from this code are given by the set of equations below, with $s_{ij} = sin(\theta_i - \theta_j)$ and $c_{ij} = cos(\theta_i - \theta_j)$.

$$\begin{aligned} (m_1 + m_2 + m_3) l_1^2 \ddot{\theta}_1 + (m_2 + m_3) l_1 l_2 c_{12} \ddot{\theta}_2 + m_3 l_1 l_3 c_{13} \ddot{\theta}_3 + \dot{\theta}_2^2 m_2 l_1 l_2 s_{12} + \\ \dot{\theta}_2^2 m_3 l_1 l_2 s_{12} + \dot{\theta}_3^2 m_3 l_1 l_3 s_{13} + (m_1 + m_2 + m_3) g l_1 s_1 = 0 \\ (m_2 + m_3) l_1 l_2 \ddot{\theta}_1 + (m_2 + m_3) l_2^2 c_{12} \ddot{\theta}_2 + m_3 l_2 l_3 c_{23} \ddot{\theta}_3 + \dot{\theta}_1^2 m_2 l_1 l_2 s_{12} + \\ \dot{\theta}_1^2 m_3 l_1 l_2 s_{12} + \dot{\theta}_3^2 m_3 l_2 l_3 s_{23} + (m_2 + m_3) g l_2 s_2 = 0 \\ m_3 l_1 l_3 c_{13} \ddot{\theta}_1 + m_3 l_1 l_3 c_{23} \ddot{\theta}_2 + m_3 l_3^2 \ddot{\theta}_3 + \dot{\theta}_1^2 m_3 l_1 l_3 s_{13} + \\ \dot{\theta}_2^2 m_3 l_2 l_3 s_{23} + m_3 g l_3 s_3 = 0 \end{aligned} \tag{A.6}$$

Generalized Forces

The payload suspension is actuated by three actuators, one at each stage of the pendulum. At each stage, only a horizontal force, in the x-direction, can be applied. The equations of motion can be rewritten the standard form:

$$M(\boldsymbol{q})\ddot{\boldsymbol{q}} + C(\boldsymbol{q}, \dot{\boldsymbol{q}}) + g(\boldsymbol{q}) = \boldsymbol{\xi} \tag{A.7}$$

Where $\boldsymbol{\xi}$ is a vector of generalized forces. This vector is found by mapping the linear forces F to generalized forces $\boldsymbol{\xi}$ at some point r by means of the analytic Jacobian ${}^r J_q$ as follows.

$$\boldsymbol{\xi} = \left(\frac{\partial r}{\partial q}\right)^T = ({}^r J_q)^T \vec{F} \tag{A.8}$$

Consider the first stage of the pendulum, that is actuated by a horizontal force at point $\boldsymbol{r}_1 = [x_1, y_1]^T$

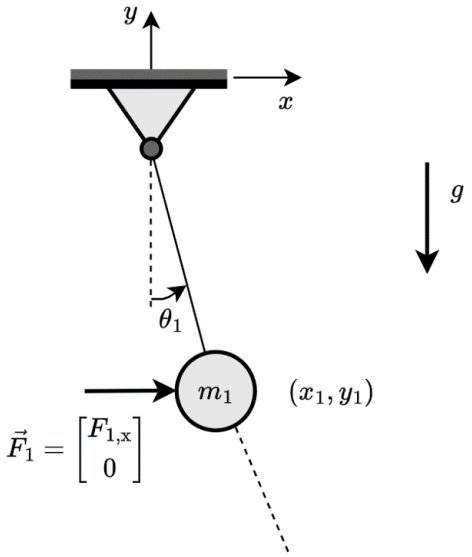

Figure A.2: A horizontal force is applied to the first stage of the pendulum at point $\boldsymbol{r}_1 = [x_1, y_1]^T$

The point $\boldsymbol{r}_1$ is described with the generalized coordinates as shown in Equation A.9, as well as the analytical Jacobian.

$$\boldsymbol{r}_1 = \begin{bmatrix} l_1 s_1 \\ -l_1 c_1 \end{bmatrix} \qquad \rightarrow \qquad {}^{r_1}J_q = \begin{bmatrix} l_1 c_1 & 0 & 0 \\ l_1 s_1 & 0 & 0 \end{bmatrix} \tag{A.9}$$

The generalized force is then found by mapping the linear forces as follows

$$\xi_1 = ({}^{r_1}J_q)^T \vec{F}_1 = \begin{bmatrix} l_1 c_1 & l_1 s_1 \\ 0 & 0 \\ 0 & 0 \end{bmatrix} \cdot \begin{bmatrix} F_{1,x} \\ 0 \end{bmatrix} = \begin{bmatrix} l_1 c_1 F_{1,x} \\ 0 \\ 0 \end{bmatrix} \tag{A.10}$$

Linearizing this equation around the operating point $\theta_i = 0 \rightarrow cos(\theta_i) \approx 1$ finally yields the linearized generalized force.

$$\xi_1 = \begin{bmatrix} l_1 F_{1,x} \\ 0 \end{bmatrix} \tag{A.11}$$

Similar derivations for the forces applied at the other two stages results in the total generalized force vector as such.

$$\boldsymbol{\xi} = \xi_1 + \xi_2 + \xi_3 = ({}^{r_1}J_q)^T \vec{F}_1 + ({}^{r_2}J_q)^T \vec{F}_2 + ({}^{r_3}J_q)^T \vec{F}_3 = \begin{bmatrix} l_1 F_{1,x} + l_2 F_{2,x} + l_3 F_{3,x} \\ l_2 F_{2,x} + l_3 F_{3,x} \\ l_3 F_{3,x} \end{bmatrix} \tag{A.12}$$

For the case where the suspension is not actuated at the mirror, $\xi_3 = 0$. Linearizing the equations of motion around the operating point $\theta_i = 0$ and rewriting them to the standard form of Equation A.7 yields the complete linearized equations of motion.

$$\underbrace{\begin{bmatrix} (m_1+m_2+m_3)l_1^2 & (m_2+m_3)l_1 l_2 & m_3 l_1 l_3 \\ (m_2+m_2)l_1 l_2 & (m_2+m_3)l_2^2 & m_3 l_2 l_3 \\ m_3 l_1 l_3 & m_3 l_2 l_3 & m_3 l_3^2 \end{bmatrix}}_{M(\boldsymbol{q})} \begin{bmatrix} \ddot{\theta}_1 \\ \ddot{\theta}_2 \\ \ddot{\theta}_3 \end{bmatrix} + \underbrace{\begin{bmatrix} (m_1+m_2+m_3)gl_1 & 0 & 0 \\ 0 & (m_2+m_3)gl_2 & 0 \\ 0 & 0 & m_3 g l_3 \end{bmatrix} \begin{bmatrix} \theta_1 \\ \theta_2 \\ \theta_3 \end{bmatrix}}_{g(\boldsymbol{q})} = \boldsymbol{\xi} \tag{A.13}$$

Notice that the Coriolis matrix $C(\boldsymbol{q}, \dot{\boldsymbol{q}})$ disappears due to the linearization, since $\dot{\theta}_i \dot{\theta}_j \approx 0$.

Appendix B

Non-convex Cost Functions for Non-smooth Optimization Strategies

Throughout this text, it is sometimes noted that the non-smooth cost function associated with the mixed $\mathcal{H}_2/\mathcal{H}_\infty$ optimization problem is not convex. Because of this non-convex nature of the cost function, the proposed non-smooth optimization method is employed. It might very well be that the solution that the optimization algorithm (`Matlab's systune()`) returns is not a globally optimal solution, but a sub-optimal one.

To illustrate this, consider the surface resembling a cost function for an arbitrary optimization problem. Now, for strictly convex problem, the cost function is bowl shaped. It only has one optimum to which the optimization algorithm converges. Local optima are not present in this case. The fictional cost function of Figure B.1 represents an optimization space that is not convex, instead, it has multiple local minima.

Let us denote the surface of a fictional cost function, as the function $f(x, y)$, with x, y a set of arbitrary parameters that are to be optimized. Roughly speaking, the non-smooth optimization algorithm finds an optimal solution by computing the gradient at some point in the optimization space and uses this to find the direction of steepest descent as:

$$\vec{\nabla} f(x, y) = \frac{\partial f}{\partial x}\boldsymbol{i} + \frac{\partial f}{\partial y}\boldsymbol{j} \tag{B.1}$$

The optimizer thus converges at points where the gradient is zero; a local optimum is located. From the figure, we can see if we pick two arbitrary points (1) and (2) on the surface $f(x, y)$, it might lead to two the localization of two different local minima that correspond to two different (sub)-optimal solutions. This is of course not necessarily the case for any two arbitrary points, but it is still something likely that can happen.

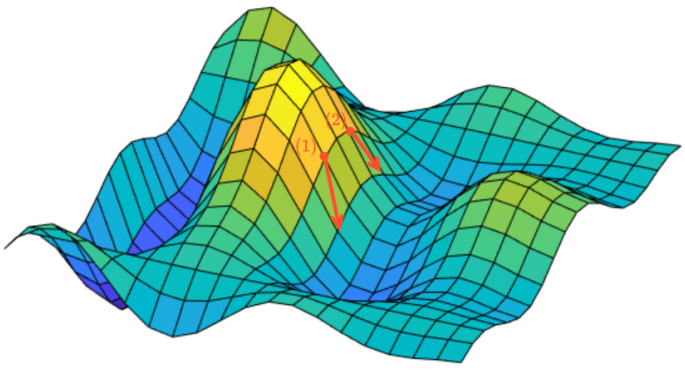

Figure B.1: Surface plot of an arbitrary cost function, including two starting points for the non-smooth optimization

Typically, it is very hard to visualize a cost function for a multi-objective optimization with many optimization parameters. This example however showcases the possibility that the found locally optimal solution is not necessarily a global one. This phenomenon is what we can attribute to the fact that the γ values for the $\mathcal{H}_\infty$ channels are not exactly 1, but close. One way to mitigate this problem, is to start the optimization at many points in the optimization space. This way, we can be somewhat sure that the optimizer finds a globally optimal solution.

Appendix C

Estimation of the Actuator Gains

The optimizer is initialized with an initial estimation of the actuator distribution. The optimizer is allowed to change these values, however, since we want to bound the actuator sizes with reasonable values, we need to make an estimation of the actuator distribution. This was done by using the known disturbance spectrum and plant inversion. The disturbance spectrum of the seismic noise is known, as well as the model of the payload suspension. The inverse of the plant can be used to derive the required force spectrum for the spectrum of the seismic noise:

$$\vec{f}_{\mathrm{a}}(\omega) = [G(j\omega)]^{-1}\vec{x}_{\mathrm{d}} \tag{C.1}$$

However, the matrix $G(s)$ is non-square and hence its inverse does not exist. A better formulation that minimizes the RMS of the force vector uses the pseudo inverse of the system $G(j\omega)$ to obtain the vector $\vec{f}_a(\omega)$:

$$\vec{f}_{\mathrm{a}}(\omega) = [G(j\omega)]^{+}\vec{x}_{\mathrm{d}} \tag{C.2}$$

Where $[G(j\omega)]^{+}$ is the Moore-Penrose pseudo inverse of $G(j\omega)$:

$$[G(j\omega)]^{+} = ([G(j\omega)]^{*}[G(j\omega)])^{-1}[G(j\omega)]^{*} \tag{C.3}$$

The RMS of the spectrum of $\vec{f}_{\mathrm{a}}$ gives the average force required and can be used to estimate the actuator gains that map the control command to the required force. This is what the initial size, that is used to initialize the optimizer, of the actuators is based on. The actuator gains are tunable elements that are constrained within reasonable bounds. The upper and lower bound for each actuator is given by a fraction of the nominal actuator size. Throughout this research, these bounds are $[K_{\mathrm{a,l}}, K_{\mathrm{a,u}}] = [10^{-2}, 10^{2}]$.

Appendix D

$\mathcal{H}_2$-optimal Controller Synthesis

The non-smooth optimization algorithm is initialized with an $\mathcal{H}_2$ optimal controller. $\mathcal{H}_2$-optimal control was investigated before the proposed non-smooth mixed synthesis method. The $\mathcal{H}_2$-optimal control paradigm is able to find controllers that attenuate seismic motion well, however stability margins are generally very small and a requirement on the open-loop equivalent DAC noise spectrum cannot directly be taken into account, while using this method. The $\mathcal{H}_2$-optimal controller was found while fixing the actuator sizes with a reasonably accurate estimation, as shown in Appendix C. First, the control formulation will be rewritten with a generalized plant $P(s)$ that includes the actuator gains. Next, an H_2 optimal controller is synthesized for this generalized plant, that aims to minimize the closed-loop motion of the mirror, while keeping the influences of the actuator disturbance to a minimum. With the controller, we can make an estimate of the PSD of the mirror motion.

D.0.1 Including K_a in the generalized plant $P(s)$

For the design of a controller for a certain fixed set of actuator gains K_a, we need to define the generalized plant formulation for the block diagram in Figure D.1. Since K_a is not part of the optimization, this block is absorbed in the generalized plant $P(s)$. The generalized plant is then derived from the block diagram as follows:

$$w = \begin{bmatrix} w_1 \\ w_2 \end{bmatrix}, \quad z = \begin{bmatrix} z_1 \\ z_2 \end{bmatrix}, \rightarrow \begin{bmatrix} z_1 \\ z_2 \\ v \end{bmatrix} = P(s) \cdot \begin{bmatrix} w_1 \\ w_2 \\ u \end{bmatrix} \tag{D.1}$$

From the block diagram in Figure D.1, we can derive the following equations:

$$z_1 = W_\mathrm{p}(V_\mathrm{x} w_1 + GK_\mathrm{a}(V_\mathrm{u} w_2 + u)) \tag{D.2}$$

$$z_2 = W_\mathrm{u}(V_\mathrm{u} w_2 + u) \tag{D.3}$$

$$v = -V_\mathrm{x} w_1 + GK_\mathrm{a}(V_u w_2 + u) \tag{D.4}$$

And from these equations, the generalized plant, which includes the actuator gain matrix K_a:

$$P(s) = \begin{bmatrix} W_\mathrm{p}V_\mathrm{x} & W_\mathrm{p}GK_\mathrm{a}V_\mathrm{u} & W_\mathrm{p}GK_\mathrm{a} \\ 0 & W_\mathrm{u}V_\mathrm{u} & W_\mathrm{u} \\ -V_\mathrm{x} & -GK_\mathrm{a}V_\mathrm{u} & -GK_\mathrm{a} \end{bmatrix} \tag{D.5}$$

The seismic disturbance and DAC noise are mapped to the mirror motion with transfer functions $S(s)$ and $S_u(s)$ respectively, such that the PSD of the residual noise at the mirror stage is:

$$\boxed{S_{\mathrm{x}_2}(s) = |T(s)|^2 S_{\mathrm{x}_0}(s) + |S_\mathrm{u}(s)|^2 S_{\mathrm{u_d}}(s)} \tag{D.6}$$

The control problem is now formulated as:

> *Find a stabilizing controller $K(s)$, that minimizes the $\mathcal{H}_2$-norm of the closed loop transfer function (i.e. minimize $|F_\mathrm{l}(P, K)|_2$)*

Here, the linear fractional transformation is the closed loop transfer function that describes the mapping from $w \rightarrow z$ and minimizing the H_2-norm should result in a minimization of the effect of the mirror disturbance x_0 on the actual motion of the mirror, while keeping the effect of the actuator disturbance to a minimum.

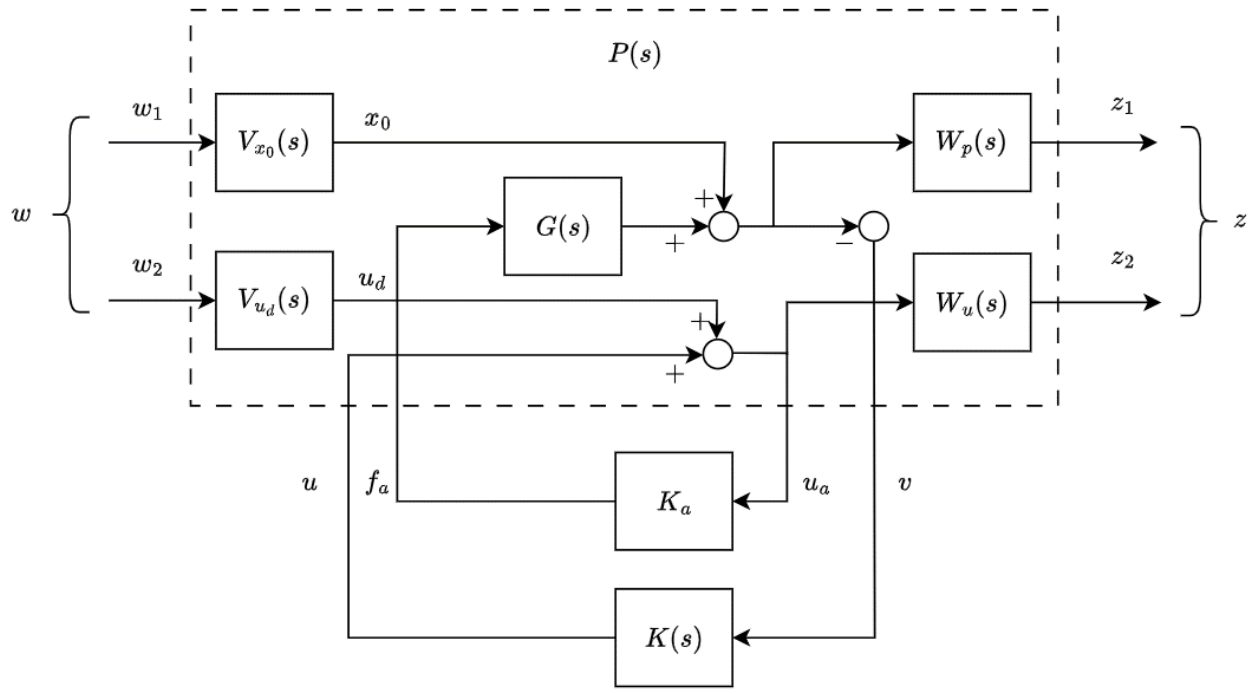

Figure D.1: Block-diagram that shows the generalized-plant

D.0.2 Weighting Filters

The freedom in the controller design lies at the definition of the weighting filters on the performance outputs, which are the mirror motion $\hat{x}(s)$ and the control output $u_a(s)$. Matlab's `h2syn()` function is used to synthesise an $\mathcal{H}_2$ optimal controller. The weighting filter for the controller output is taken as a gain:

$$W_{\mathrm{u}} = K_{\mathrm{u}} \tag{D.7}$$

The performance weighting filter on the motion of the mirror is also taken as a gain, since it is expected that the optimizer designs a controller such that it suppresses the seismic noise in the appropriate frequency regime.

D.0.3 Controller Synthesis

The generalized plant, together with the weighting filters and noise colouring filters are defined in Matlab, and an $\mathcal{H}_2$ optimal controller was synthesized. The performance of the controller is checked by comparing the open-loop response to the disturbances with the closed loop response to the disturbances.

With the found controller, we can compute the spectrum of the total noise contribution to the motion of the mirror via Equation D.6. The total noise contribution is compared with the noise budget of ET-LF. This figure also shows the open loop contribution of seismic motion to the mirror motion.

Scaling and Numerical Issues

The controller synthesis via the `h2syn()` function appears to have some numerical problems for the computation of a controller. It is expected that this is due to a large variation in gains and therefore, the plant and weighting filter are scaled, such that the gain of the weighting filter is more reasonable. The plant is scaled with a gain T_y, such that the output of system $G(s)$ is in nm instead of m, hence $T_y = 10^9$. The weighting filter, which is the approximate of the inverse of the ET-LF sensitivity curve, can therefore be scaled down by the same amount (10^9) to match the unit of the plant's output. This results in that the gain of the plant and performance weighting filter are much closer to each other and the noise shaping filter gains. The controller for the actual, unscaled plant is then computed by scaling

the controller with the same scaling T_y.

$$K(s) = T_{\mathrm{y}} \cdot K_{\mathrm{scaled}}(s) \tag{D.8}$$

In order to limit the number of states of the generalized plant $P(s)$, it is favourable to define the generalized plant with the `connect()` function. This omits building the generalized plant as a matrix from transfer functions, and significantly reduces the number of states in the state-space representation of the generalized plant. Moreover, the generalized plant can be rewritten as $P(s) = W(s)P'(s)V(s)$ as:

$$P(s) = W(s)P'(s)V(s) = \begin{bmatrix} W_{\mathrm{p}} & 0 & 0 & 0 \\ 0 & W_{\mathrm{u}} & 0 & 0 \\ 0 & 0 & W_{\mathrm{u}} & 0 \\ 0 & 0 & 0 & 1 \end{bmatrix} \cdot \begin{bmatrix} I_{1\times1} & GK_{\mathrm{a}1\times2} & GK_{\mathrm{a}1\times2} \\ 0_{2\times1} & I_{2\times2} & I_{2\times2} \\ -I_{1\times1} & GK_{\mathrm{a}1\times2} & GK_{\mathrm{a}1\times2} \end{bmatrix} \cdot \begin{bmatrix} V_{\mathrm{x}} & 0 & 0 & 0 & 0 \\ 0 & V_{\mathrm{u}} & 0 & 0 & 0 \\ 0 & 0 & V_{\mathrm{u}} & 0 & 0 \\ 0 & 0 & 0 & 1 & 0 \\ 0 & 0 & 0 & 0 & 1 \end{bmatrix} \tag{D.9}$$

This allows to use the `lft(P', K)` command to define the closed loop transfer functions, as the generalized plant without weighting filters and noise filters is defined.

D.0.4 Checking the Actuator Command Voltage

The required force that must be delivered by the actuators must be within the limits of the actuator. In order to do this, we can compare the spectrum of the control force with the actuator gains and check whether the actuators are actually capable to deliver the required force to reduce the influence of seismic motion. From the block diagram, we can write the actuator voltage signals as a sum of two closed loop transfer functions that relate the noise disturbances to the required actuator voltage. From the diagram, we can derive:

$$u_{\mathrm{a}} = ud + K(-x_0 - GK_{\mathrm{a}}u_{\mathrm{a}}) \tag{D.10}$$

$$(I + KGK_{\mathrm{a}})u_{\mathrm{a}} = u_{\mathrm{d}} - Kx_0 \tag{D.11}$$

$$u_{\mathrm{a}} = (I + KGK_{\mathrm{a}})^{-1}u_{\mathrm{d}} - (I + KGK_{\mathrm{a}})^{-1}Kx_0 \tag{D.12}$$

$$u_{\mathrm{a}} = S_{u_{\mathrm{a}}}u_{\mathrm{d}} + S_{u_{\mathrm{d}}}Kx_0 \tag{D.13}$$

The transfer function $S_{u_d}K$ can be rewritten to:

$$S_{u_{\mathrm{a}}}K = (I + KGK_{\mathrm{a}})^{-1}K = K(I + GK_{\mathrm{a}}K)^{-1} \tag{D.14}$$

D.0.5 Results of the Controller Synthesis

The controller, computed via H_2-synthesis, can be used to compute closed loop transfer functions, which can be used to compute the spectra of the noise contributions and the total closed loop noise contribution using Equation D.6.

It can be seen that the effect of the seismic activity is reduced significantly, while keeping the influence of the DAC noise below the ET-LF sensitivity curve, hence indicating an improved performance of the payload vibration isolating characteristics. The closed loop transfer functions that determine the noise propagation to the motion of the mirror are repeated below:

$$\hat{x}_2(s) = Sx_0(s) + GSu_{\mathrm{d}}(s) \tag{D.15}$$

$$S = (1 + GK_{\mathrm{a}}K)^{-1}, \qquad GS = GK_{\mathrm{a}}(1 + GK_{\mathrm{a}}K)^{-1} \tag{D.16}$$

The magnitude of the frequency response of these transfer functions is shown in Figure D.3. It can be seen that the magnitude of the sensitivity function is particularly low in the frequency region where the seismic disturbance is present, as this function describes the transfer from seismic vibrations to the motion of the mirror. The sensitivity to the DAC noise is low over the whole frequency range, with some peaking near the sensitivity range of the ET-LF noise budget. However, this peaking does not seem to

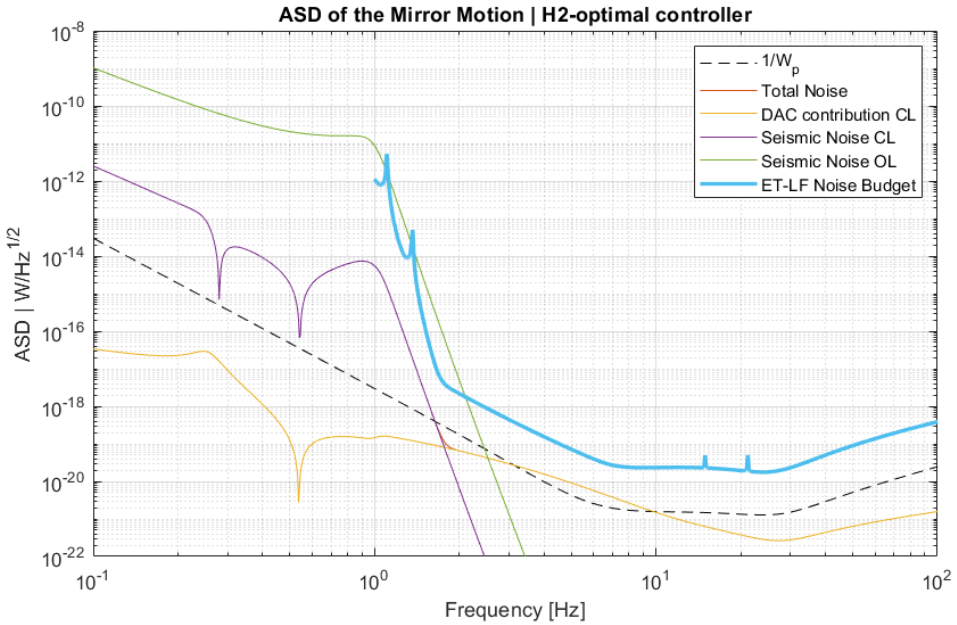

Figure D.2: ASD of the mirror motion and noise contributions

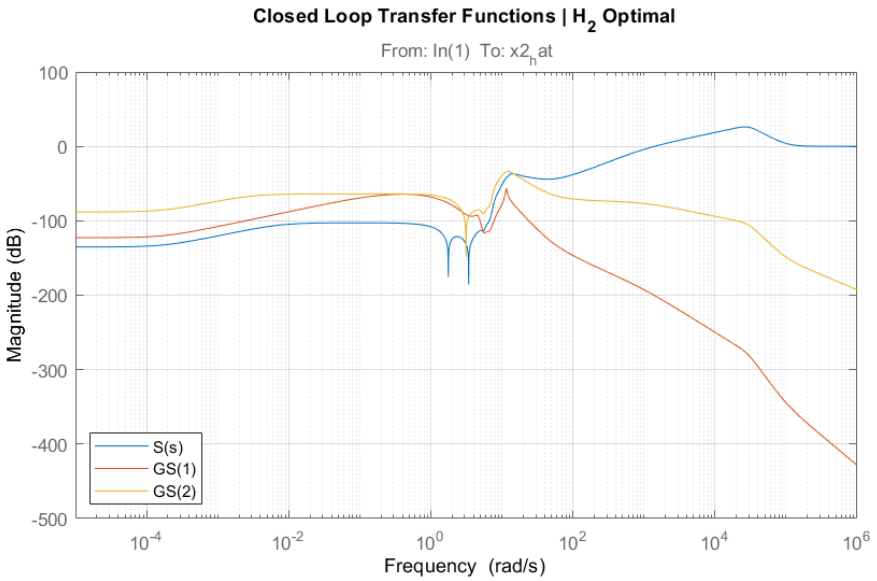

Figure D.3: Closed loop transfer functions S and GS

affect the closed loop contribution to the total mirror motion too much.

Although the seismic noise is suppressed quite well in the low frequency area, there is one requirement for the control system that was not taken into account. Chapter 2 posed why the so called open-loop equivalence of the DAC noise should not exceed the design sensitivity curve. This is typically reflected by an $\mathcal{H}_\infty$-optimization. Although the main objective for the control system is to attenuate seismic disturbances, the requirement on the open-loop equivalent DAC is as important. Such a requirement cannot be taken into account by the $\mathcal{H}_2$-optimizer. The last section of this chapter poses an alternative method that could provide a solution to this shortcoming of nominal $\mathcal{H}_2$-synthesis.

D.0.6 Stability

The algorithm that computes the H_2-optimal controller always is a stabilizing controller, however, no stability margins can be guaranteed. Therefore, the margins to instability are assessed to check whether the system is robust to changes in system gain and phase. The Modulus Margin is defined as the inverse of the H_∞-norm (Nominal Sensitivity Peak) of the sensitivity function:

$$MM = \frac{1}{M_\mathrm{s}}, \qquad M_\mathrm{s} = \sup_{0\leq\omega\leq\infty} |S(j\omega)| \tag{D.17}$$

Figure D.3 shows a magnitude plot of the sensitivity function. The loop gain for the control system is given by:

$$L = GK_\mathrm{a}K \tag{D.18}$$

And the sensitivity function is computed as:

$$S = (I + L)^{-1} \tag{D.19}$$

The magnitude of the frequency response is shown in Figure D.3 (blue line). The peak of the sensitivity has a value of approximately $M_s = 26.2dB = 20.4$. This corresponds to a modulus margin of $MM = 0.05$, which is rather low, as the rule of thumb states that a modulus margin of 0.5 is a nice value to meet. Now, it is assumed that the plant is known very well, and the operating conditions are also quite constant, hence the need for great stability margins is not as important, as the uncertainty in the system and process variations is not very large. Therefore, a modulus margin above at least 0.1 would be sufficient.

The Nyquist plot for the loop gain L is shown in Figure D.4, as well as a green circle, of which the radius corresponds to the modulus margin of the controlled payload. The controller introduces two RHP poles, and the Nyquist plot has two counter-clockwise encirclements of the critical point $s = -1 + 0j$, hence indicating a stable loop. However, a small variation in phase and gain can change the number of encirclements, which is reflected by the small modulus margin and hence the system is stable, but not very robust to process variations.

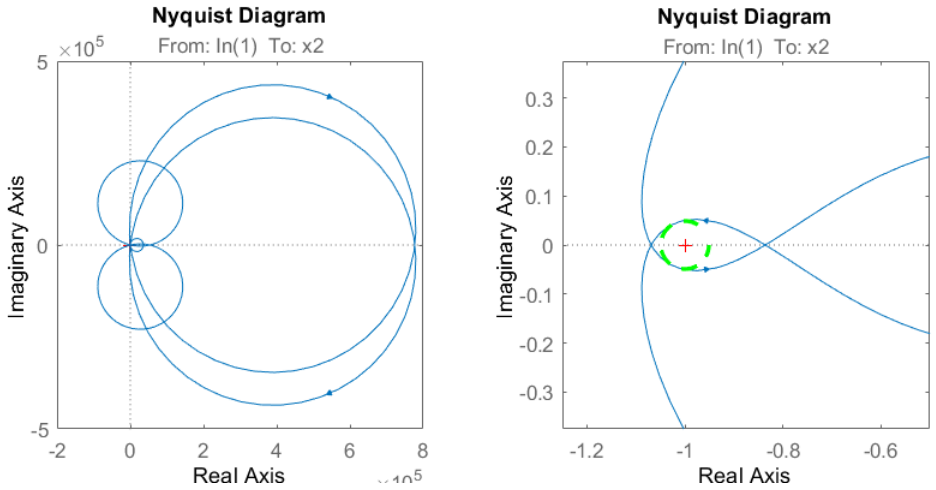

Figure D.4: Nyquist diagram of $L = GK_aK$

The H_2-optimal control algorithm does not include a way to reduce the S_∞ norm, whereas the H_∞-optimal solution implicitly does: if we would impose a weighting filter on the sensitivity function, the controller should aim to keep the sensitivity peak below this filter. If possible, the H_∞-optimal solution should return a controller that results in that the sensitivity function should be below the inverse of the weighting filter. In this case study, a gain could provide a limit to the nominal sensitivity peak. This gain would correspond to the maximum allowable nominal sensitivity peak M_s, which dictates the modulus margin. For a modulus margin of $MM = 0.2$, the sensitivity peak should be reduced to $M_s = 1/MM = 5$, which corresponds to a peak of $14dB$ at most.

D.0.7 $\mathcal{H}_2$-Optimal Control with Sensor Noise

The optimization algorithm `h2syn()` adds extra disturbance and measurement channels to make a solvable problem. This seems to have a great impact on the actual plant that is optimized by the command as the regularized plant that `Matlab` solves for, appears to be rather different to the generalized plant that is described in Equation D.22. Therefore, a similar H_2 optimization is discussed in this section, which includes sensor noise as an extra disturbance to the system. It is expected that this makes for a better solvable problem, and moreover, a more realistic plant, as sensor noise is always present to some extent in a real control system.

Reformulating the Block Diagram

The block diagram, that includes the sensor noise, is shown in Figure D.5. Note that the performance channel z_2 is now the control signal. Previously, the performance channel was defined on the actuator command signal u_a, however, this results in a direct feed-through term in the state-space representation of the generalized plant, which results in a problem that can in principle not be solved. The `h2syn()` command does return a controller however, but the controller is computed for a system for which this direct feed-through is ignored. Therefore, a more neat approach is to define the performance channel z_2 as the control command u directly, instead of the noise polluted signal u_a.

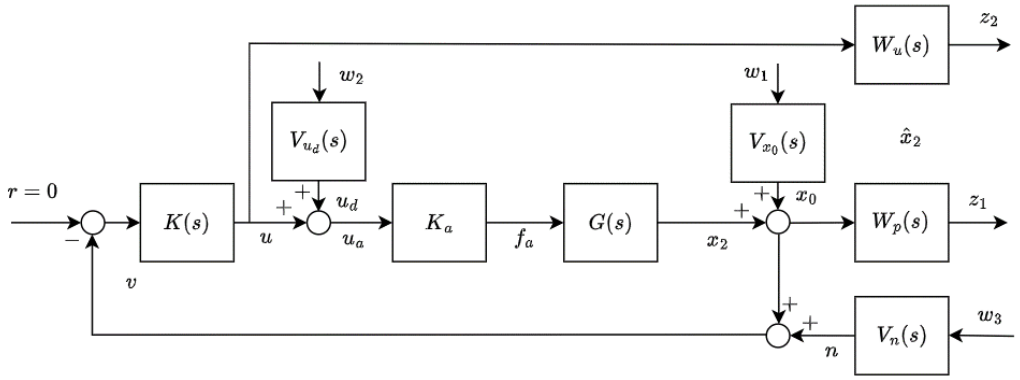

Figure D.5: Block diagram of the control system, including sensor noise

The generalized plant is now defined for the inputs $w = [x_0, u_{d_1}, u_{d_2}, n]$:

$$\begin{bmatrix} z_1 \\ z_2 \\ v \end{bmatrix} = P(s) \cdot \begin{bmatrix} w_1 \\ w_2 \\ w_3 \\ u \end{bmatrix} \tag{D.20}$$

$$P(s) = \begin{bmatrix} W_p V_x & W_p G K_a V_u & 0 & W_p G K_a \\ 0 & 0 & 0 & W_u \\ -V_x & -G K_a V_u & V_n & -G K_a \end{bmatrix} \tag{D.21}$$

Rewriting the generalized plant in the form $P(s) = W(s)P'(s)V(s)$ results in the following definition of the generalized plant, which allows to compute the closed loop transfer function matrix $T_{w\to z}(s)$ that maps $w \to z$ with `Matlab's lft(P', K)` command.

$$P(s) = W(s)P'(s)V(s) = \begin{bmatrix} W_p & 0 & 0 & 0 \\ 0 & W_u & 0 & 0 \\ 0 & 0 & W_u & 0 \\ 0 & 0 & 0 & 1 \end{bmatrix} \cdot \begin{bmatrix} I_{1\times1} & GK_{a1\times2} & 0_{1\times1} & GK_{a1\times2} \\ 0_{2\times1} & 0_{2\times2} & 0_{2\times1} & I_{2\times2} \\ -I_{1\times1} & GK_{a1\times2} & V_{n1\times1} & GK_{a1\times2} \end{bmatrix} \cdot \begin{bmatrix} V_x & 0 & 0 & 0 & 0 & 0 \\ 0 & V_u & 0 & 0 & 0 & 0 \\ 0 & 0 & V_u & 0 & 0 & 0 \\ 0 & 0 & 0 & V_n & 0 & 0 \\ 0 & 0 & 0 & 0 & 1 & 0 \\ 0 & 0 & 0 & 0 & 0 & 1 \end{bmatrix} \tag{D.22}$$

The total motion of the mirror now also depends on the sensor noise. From the block diagram, it can be seen that the total motion of the mirror due the disturbances is computed as:

$$\hat{x}_2 = (1 + GK_aK)^{-1}x_0 + (1 + GK_aK)^{-1}GK_au_d - (1 + GK_aK)^{-1}GK_aKn \tag{D.23}$$

$$\hat{x}_2 = Sx_0 + GSu_d - Tn \tag{D.24}$$

The actuator command signal is computed as:

$$u_a = (I + KGK_a)^{-1}Kx_0 + (I + KGK_a)^{-1}u_d + (I + KGK_a)^{-1}n \tag{D.25}$$

$$u_a = KSx_0 + S_uu_d + S_un \tag{D.26}$$

The closed loop transfer functions from Equation D.23 and D.25 define the spectra of the total mirror motion and actuator effort respectively.

D.0.8 Results

A controller was computed similar to the approach that was shown in the previous paragraph. The spectra of the total motion of the mirror due to the DAC noise, seismic motion and sensor noise under closed loop control is shown in Figure D.6. From the figure it can be seen that the seismic motion is suppressed in the low frequency region, while keeping the effects of the DAC noise and sensor noise below the ET-LF noise budget. It must be noted though, that the sensor noise model is taken as a rather small noise, to keep the total noise below the noise budget. The PSD of $\hat{x}_2$ is then computed as a function of the disturbance spectra as follows:

$$S_{\hat{x}_2}(j2\pi f) = |S(j2\pi f)|^2 S_{x_0}(j2\pi f) + |G(j2\pi f)S(j2\pi f)|^2 S_{u_d}(j2\pi f) + |T(j2\pi f)|^2 S_n(j2\pi f) \tag{D.27}$$

The ASD of the closed loop mirror motion is the square root of the PSD of $\hat{x}_2$ and the amplitude spectral density is shown below.

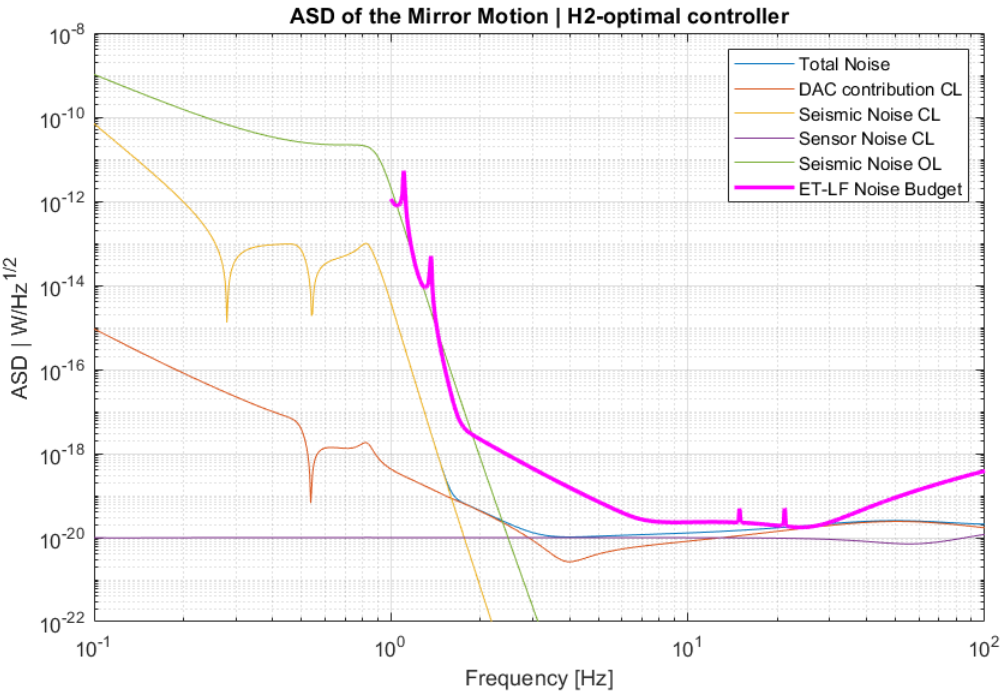

Figure D.6: Spectra of the total closed loop mirror motion and individual contributions

Figure D.7 shows the closed loop transfer functions S, GS and T, that define the spectrum of the mirror motion under closed-loop control. It can be seen that the synthesized controller results in a sensitivity function that suppresses the seismic noise and DAC noise in the ET-LF sensitivity bandwidth. The sensor noise, however is not suppressed very well in this region, as the transfer function $T = 1 - S$. This results in a trade-off between suppressing sensor noise and seismic noise.

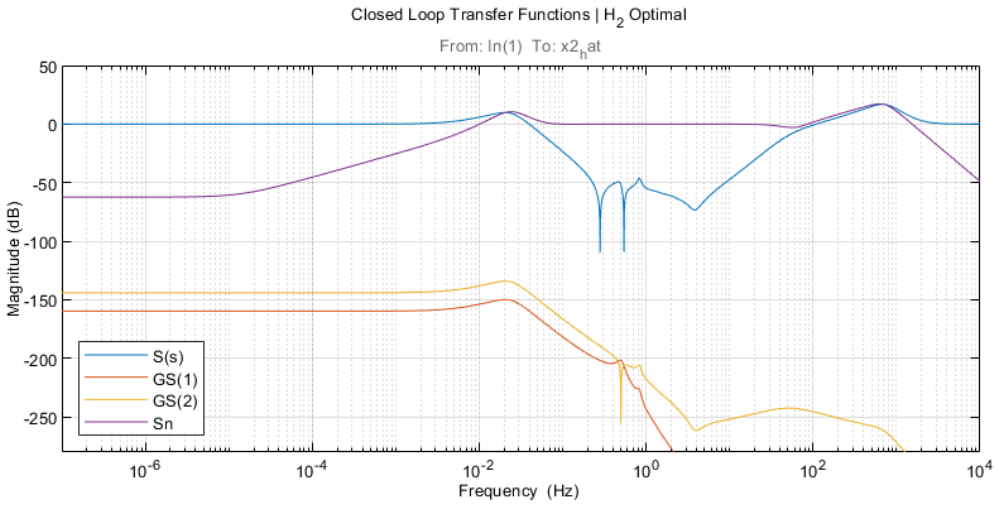

Figure D.7: Closed-loop transfer functions S, GS and T

Stability

The Nyquist plot of the open-loop gain L is shown in Figure D.8. The open-loop L has 6 poles in the RHP, which are the poles from the controller. The Nyquist plot encircles the critical point 6 times in the counter-clockwise direction, hence the closed-loop system is stable.

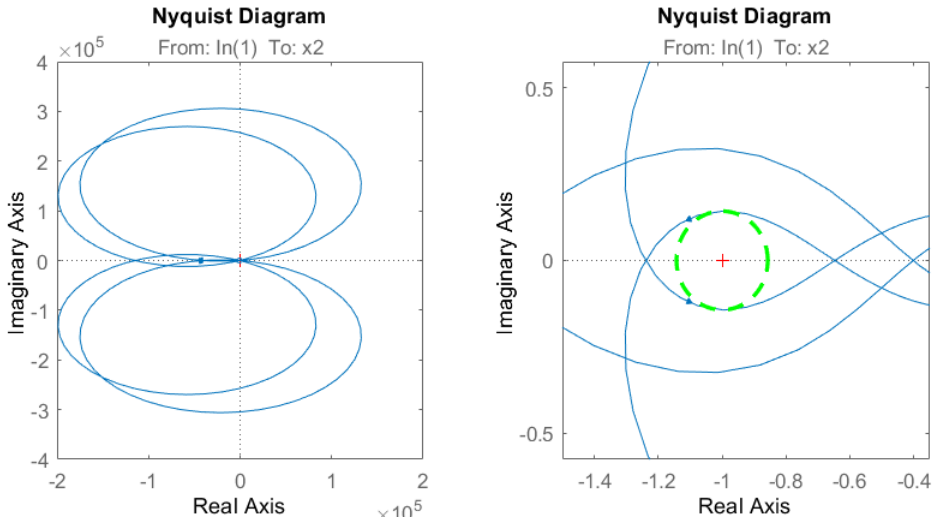

Figure D.8: Nyquist plot for the open-loop gain $L = GK_aK$, $MM = 0.14$

The modulus margin is computed as shown in Equation D.17, and a green circle with the radius of the modulus margin is shown in the right plot of this figure. The modulus margin for the system has a value of $MM = 0.14$, which is reasonable, but note that this margin is not specified, so a different weighting function could result in a system that is marginally stable.

D.0.9 Mixed $\mathcal{H}_2/\mathcal{H}_\infty$ Synthesis

Although the $\mathcal{H}_2$-optimal controller is a stabilizing controller, it can not be guaranteed that the controller resulting from the synthesis provides a closed loop control system that has nice stability margins. $\mathcal{H}_\infty$-optimal control does allow to compute a controller that guarantees, or is close to, some specified stability margin, by placing an $\mathcal{H}_\infty$ constraint on a closed loop transfer function. Previously, the sensitivity function $S = (1 + L)^{-1}$ function was used to compute the modulus margin for the system, which specifies how far the open-loop gain L is from the critical point $s = -1 + 0j$. Specifying a certain bound on the

sensitivity function by applying a $\mathcal{H}_\infty$ bound on the sensitivity function therefore allows to synthesize a controller that guarantees a certain stability bound, that is related to the S_∞ norm. Besides robustness, the open-loop equivalent DAC noise should also be bounded by an $\mathcal{H}_\infty$ constraint. Ultimately, the ET-LF design sensitivity forms a frequency dependent hard limit.

In order to fully capture the requirements for the payload suspension, both $\mathcal{H}_2$ and $\mathcal{H}_\infty$. This can be included in a mixed $\mathcal{H}_2/\mathcal{H}_\infty$ synthesis method. A general block scheme for this problem is shown in Figure D.9.

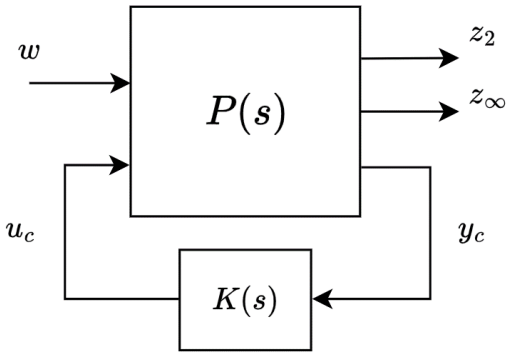

Figure D.9: General block scheme for a mixed $\mathcal{H}_2/\mathcal{H}_\infty$ control problem

Where the z_2 channel is used to ensure that the energy of these signals is kept to a minimum, and where the z_∞ channel imposes a constraint of the gain of the associated transfer function.

The addition of one or more $\mathcal{H}_\infty$-constraints to the $\mathcal{H}_2$-synthesis results in an optimization problem that is not convex anymore. Therefore, an alternative optimization method, proposed in [11], is used to compute the optimal controller for a problem that includes both $\mathcal{H}_2$ and $\mathcal{H}_\infty$ constraints. The $\mathcal{H}_2$-optimizer also showed some difficulties that were likely the cause of a numerically poor conditioned generalized plant. This may be attributed to the broad range of singular values for the different optimization paths for the control problem. Presumably, the aforementioned mixed synthesis approach is numerically better conditioned. It should suffer less from these problems that nominal $\mathcal{H}_2$-synthesis via LMI based solvers encounter.